The Rock Record of Mars: Structure, Sedimentology and Stratigraphy

Thesis by

Kevin W. Lewis

In Partial Fulfillment of the Requirements

for the Degree of

Doctor of Philosophy

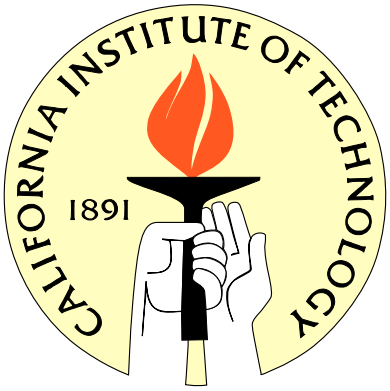

California Institute of Technology

Pasadena, California

2009

(Defended May 21, 2009)

Amerika, du hast es besser

als unser Kontinent, der alte,

hast keine verfallenen Schlösser

und keine Basalte.

Dich stört nicht im Innern

zu lebendiger Zeit

unnützes Erinnern

und vergeblicher Streit.

—Goethe

Acknowledgements

I have been unbelievably fortunate to arrive at Caltech in the midst of a renaissance in Mars exploration. During the course of my graduate career, five successful spacecraft joined the two already in orbit around Mars when I arrived, including four orbital and three landed missions. While two of these missions have since ended, five remain in operation at Mars. It has been a welcome challenge to stay afloat in the midst of the enormous volumes of data being returned every day from what could rightfully be called a fleet of Mars spacecraft.

This work was only made possible with the kindness, generosity, and intellectual guidance of a great number of people, without whom I would be lost. Ultimately, I am indebted to my parents, who taught by example a deep-seated love of learning. Most importantly, I seem to have inherited a mix of confidence and humor, along with a joy for creating things, whether it be a table, a t-shirt, or a thesis. I am forever grateful for the sacrifices they made to get me this ~~fat~~ far.

Intellectually, I recieved a great deal of direction from my undergraduate research advisors at Tufts University. Peggy Cebe was willing to take me into her lab as a freshman, and gave me a great deal of career advice. Sam Kounaves didn't realize I was only in the Chemistry department for a work-study job, and offered me my first chance to work on Mars research, opening the gateway to a new community.

Despite our seemingly divergent personalities, I couldn't ask for a better mentor than my research advisor, Oded Aharonson. He has been responsible more than anyone for my development into the role of a professional scientist. I am grateful for his efforts to foster a productive research environment, where any material or intellectual resource simply appeared nearly before I knew I had a need for it. Oded provided me with all the data I could want, and simply asked that I do good

science with it. He has instilled in me countless bits of wisdom, and ensured a sense of confidence in my own scientific ability. Our most serious disputes could usually be solved by Strunk and White, and I owe a debt of gratitude for Oded's unending attempts to spare me the embarrassment of poor use of the English language. I am truly glad to be able to count him as a friend.

Several other professors have had an outstanding influence over the course of this work. Andy Ingersoll, with whom I am glad I had the opportunity to work early in my time at Caltech, taught me the elegance of simplicity. John Grotzinger was an intellectual force, helping me to bridge the terrestrial and planetary communities, and spending countless hours with me in pursuit of scientific truth. Jean-Philippe Avouac was an invaluable resource when I got stuck at scientific and technical roadblocks. Additionally, I am indebted to the GPS staff, in particular Nora Oshima and Mike Black, for their unrelenting help with all sorts of technical challenges.

I must thank my scientific collaborators with whom this work was accomplished. Steve Squyres and Alfred McEwen have been incredibly generous, and welcomed me into the MER and HiRISE families. Indeed, it has been a pleasure and an honor to collaborate with the science and engineering teams of both missions. Anton Ivanov, Randy Kirk and Annie Howington-Kraus have been unsparing of their tools and knowledge regarding stereo processing. Alex Hayes and Terry Suer have frequently helped me with the day-to-day snags that come with doing research, and I can only hope that I have been able to help them in return.

My friends have been an inestimable source of support and relief. It has been a pleasure to share time and space with my officemates. In particular, I truly enjoyed the company of Colette Salyk, Xin Guo, Kaveh Pahlevan, and Kris Barkume over all these years, in and out of the office. A whole bunch of crazy people who make me smile are too numerous to mention, but have kept me firmly anchored on this planet despite my tendency to get lost in a sea of rocks and pixels.

Abstract

This work combines several studies related to the sedimentary rock record of Mars. Data from several spacecraft are employed to ascertain the formation mechanisms and timescales of stratified outcrops exposed at the surface, In particular, high-resolution topographic data from stereo images are utilized to obtain quantitative estimates of geologic structure and stratigraphy. The first investigation focuses on a well-preserved fluvial distributary network exposed in Eberswalde crater. Geologic structure and basin topography are used to assess modes of formation and place limits on the deposition timescale. Chapter 3 describes an enigmatic feature studied by the Spirit rover, an 80 m diameter, intricately cross-bedded plateau known as Home Plate. Via combined analysis of the stratigraphy, structure, and sedimentology, a pyroclastic origin is proposed for the origin of this enigmatic sedimentary deposit. Finally, chapter 4 focuses on the occurrence of several rhythmically bedded sedimentary deposits across the surface of Mars. The strong quasiperiodicity seen in the stratigraphy at these locations is likely evidence of allogenic control on deposition from external climate cyclicity. Two scales of periodicity are demonstrated for one section at Becquerel crater. We propose a link to orbital forcing via the obliquity cycle of Mars.

Contents

List of Figures

List of Tables

List of Acronyms

CRISM Compact Reconnaissance Imaging Spectrometer for Mars

DEM Digital Elevation Model

DTM Digital Terrain Model

HiRISE High Resolution Imaging Science Experiment

ISIS Integrated Software for Imagers and Spectrometers

OMEGA Observatoire pour la Minéralogie, l'Eau, les Glaces, et l'Activité

MARSIS Mars Advanced Radar for Subsurface and Ionosphere Sounding

MER Mars Exploration Rover

MGS Mars Global Surveyor

MI Microscopic Imager

MOC Mars Orbiter Camera

MOLA Mars Orbiter Laser Altimeter

MRO Mars Reconnaissance Orbiter

MSL Mars Science Laboratory

TES Thermal Emission Spectrometer

THEMIS THermal EMission Infrared Spectrometer

Chapter 1

Introduction

1.1 The Sedimentary Rock Record of Mars

Among the terrestrial and icy bodies in our Solar System, there exists a wide range in surface activity. While some have remained essentially static for billions of years, others show evidence for dynamic surface processes throughout their history. By their very nature, geologic processes tend to conceal or destroy evidence of preexisting conditions. The Earth's rapidly changing surface continually devours its own history, leaving only fragments behind. These pieces make up the terrestrial geologic record, from which we are able to reconstruct the planet's past. Among the other bodies in the Solar System, Mars is the only one known to have an extensive sedimentary rock record. These rocks document the actions of water, wind, and other processes that occurred on the Martian surface. The combination of a rich geologic history along with a diverse record of that activity has made Mars a natural target for scientific study.

The presence, and significance, of well-stratified geologic units on Mars were recognized first from Mariner 9 images of Ganges Chasma and elsewhere in the Valles Marineris region (*Sharp*, 1973). However, the arrival of the Mars Orbiter Camera (MOC) in 1997 opened the door to the study of Martian stratigraphy (*Malin and Edgett*, 2000). Years of mapping by MOC showed that although the sedimentary rocks of Mars are extensive, they have a highly heterogeneous spatial distribution across the planet's surface. As an illustration, Figure 1.1A) shows the locations of all MOC Narrow Angle images from aerobraking through the S10 mission phase (Sept. 1997–Sept. 2005), while

Figure 1.1B) shows only images of layered rocks, identified from image header keywords. While the full data set is fairly evenly distributed over the planet, images of layered terrains are highly non-uniform. Figure 1.2 shows the corresponding latitudinal percentage histograms for the two sets of images. In particular, the large majority of sedimentary deposits are located within $\sim 30^\circ$ of the equator, with the thickest sections concentrated between -10° and 10°. Isolated occurrences of stratified rocks, particularly Holden, Eberswalde, Terby, Galle, and Spallanzani craters, account for the peaks at -25° and -55°. Although sediments which may have been buried or completely eroded would not be included in the dataset, this distribution likely points to a strongly latitudinally dependent climate system throughout Martian history.

Sedimentary rocks on Mars can be broadly grouped into classes based on geologic context, mineralogy, and morphology. *Malin and Edgett* (2000) first delineated the sedimentary rocks of Mars into layered, massive, and thin mesa units based on morphology. Subsequent research, along with the arrival of new spacecraft instruments, allows for additional classifications based on mineralogy and morphology. Although these groupings are not mutually exclusive, and may not cover the full diversity of martian sedimentary rocks, they serve as a general framework for subsequent discussion. These broadly defined classes include fluvial deposits, pervasively weathered regions, sulfate-rich terrains, Arabia Terra intracrater mounds, midlatitude mounds, and pyroclastic deposits.

1.1.1 Fluvial Deposits

Terminal deposits have for been recognized for some time where fluvial valleys empty into topographic basins on Mars (*Cabrol and Grin*, 1999). Even with high-resolution images, it has been difficult to distinguish whether the sediment was transported in a subaqueous deltaic setting, or whether the deposits are simply eroded remnants of subaerial alluvial fans (*Irwin et al.*, 2005; *Moore and Howard*, 2005). A second important question is the timescale over which fluvial systems were active, a topic addressed in chapter 2 for the best-preserved example of a fluvial distributary system, in Eberswalde crater. Only a handful of these deposits have exposed strata, most notably those within Holden, Eberswalde, and Jezero craters (*Grant et al.*, 2008; *Malin and Edgett*, 2003;

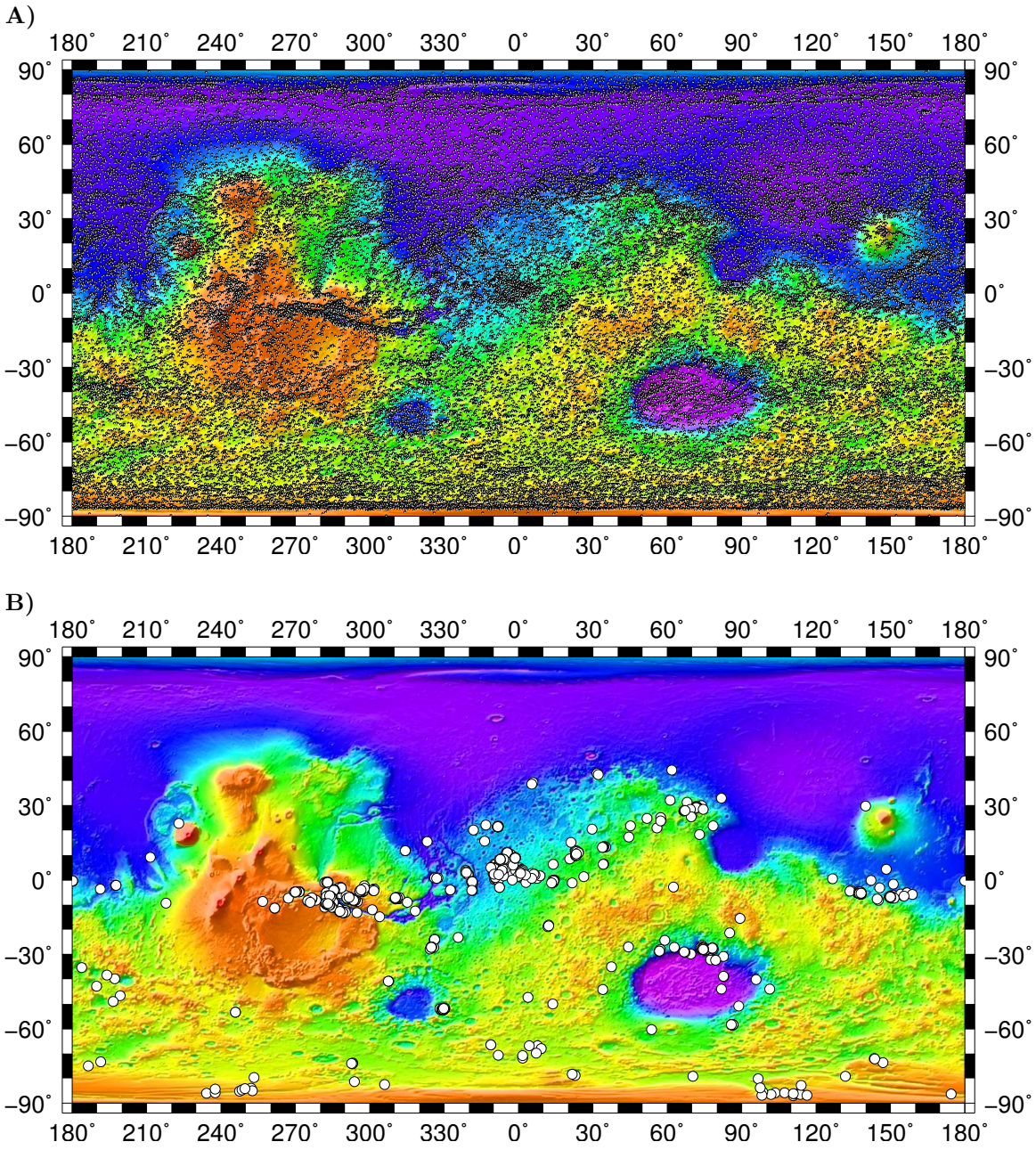

Figure 1.1: A) Map showing the location of all MOC-NA images from aerobraking through mission phase S10 (Sept. 1997–Sept. 2005) plotted over MOLA shaded topography. Although a few regions have somewhat higher image densities, coverage is roughly uniform across the planet. B) Map showing only MOC images of layered outcrops, identified by searching image header keywords. Points poleward of 70° are generally images of polar ice layers, rather than bedrock. In general, the distribution is highly heterogeneous. Concentrations of images are found within Valles Marineris, the Meridiani Planum/Arabia Terra region, north of the Hellas basin, and South of Elysium Mons. Isolated sedimentary rocks are also found within Gale, Holden, Eberswalde, Galle, and Spallanzani Craters.

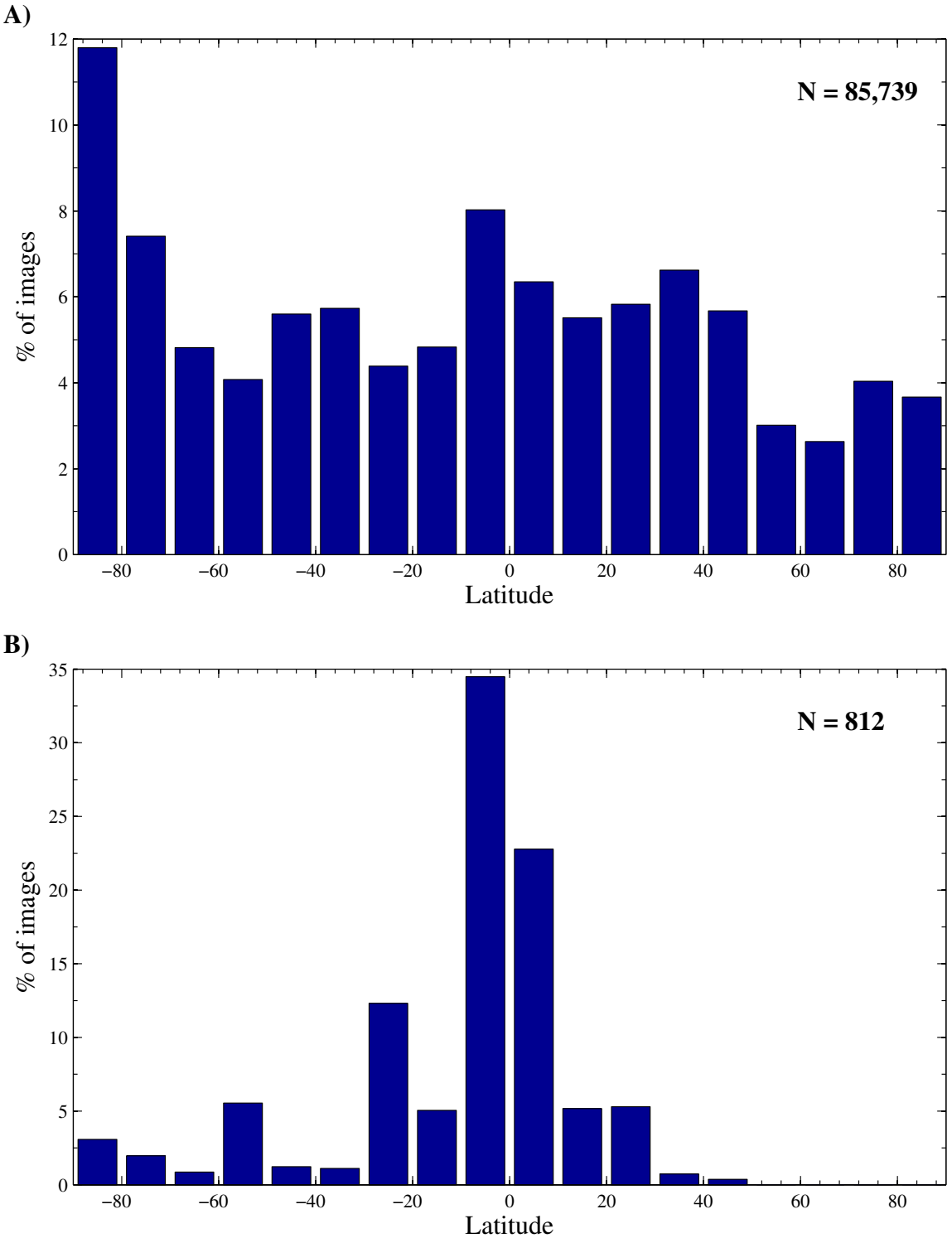

Figure 1.2: A) Latitudinal histogram of the data points shown in Figure 1.1A), showing a fairly uniform distribution. B) Latitudinal histogram of the data points shown in Figure 1.1B). Sedimentary rock outcrops are strongly concentrated within 10° of the equator, with isolated occurrences at higher latitudes. Images of the outcrops in Holden, Eberswalde, and Terby crater account for much of the peak at −25°, while those in Galle and Spallanzani crater are largely responsible for the peak at −55°. (Images at high southern latitudes are generally of the layered south polar ice cap, rather than rock outcrops.)

Fassett and Head, 2005). In other cases, terminal fluvial deposits are highly eroded or mantled, such that no internal stratigraphy is apparent. Recent observations by the Compact Reconnaissance Imaging Spectrometer for Mars (CRISM) of these three notable craters reveal the presence of phyllosilicate minerals (*Mustard et al.*, 2008a). Although these minerals are signs of aqueous alteration, it remains unclear whether they formed in place or were transported downstream from more widely altered Noachian crustal source regions. Owing both to their compelling morphology and mineralogy, Holden and Eberswalde craters remain two of the top candidate landing sites for the 2011 Mars Science Laboratory (MSL).

1.1.2 Pervasively Weathered Regions

Two regions of Mars appear to have an anomalously high concentration of secondary minerals, suggesting extensive alteration. The first unambiguous detections of phyllosilicates on Mars were achieved with the OMEGA instrument on Mars Express (*Bibring et al.*, 2005). A variety of smectite minerals were observed, most notably in extensive outcrops around Mawrth Vallis and Nili Fossae (*Poulet et al.*, 2005). More recently, CRISM has expanded the number of phyllosilicate detections on Mars to many smaller outcrops in the southern highlands, suggesting extensive alteration of the ancient crust (*Mustard et al.*, 2008a). In the Nili Fossae region, phyllosilicate formation appears to be largely a product of subsurface alteration, and is poorly correlated with fluvial features (*Mangold et al.*, 2007). Additionally, the detection of magnesium-bearing carbonate minerals has been proposed in a higher stratigraphic unit in the region, although the context is also unclear (*Ehlmann et al.*, 2008). At Mawrth Vallis, several phyllosilicates have been detected including kaolinite and smectite minerals, along with opaline silica deposits (*Bishop et al.*, 2008). Although the outcrops at Mawrth Vallis (one of the four candidate MSL landing sites) appear stratified in high-resolution images, their depositional context remains unclear. In particular, it is unclear whether the phyllosilicate bearing units, which seem to conform to underlying topography, are sedimentary or pedogenic (*Wray et al.*, 2008).

1.1.3 Sulfate-rich Terrains

Several large geologic formations on Mars have been shown to be rich in a variety of sulfate minerals, of varying hydration states. Chief among these is Meridiani Planum, the landing site of the Opportunity Mars Exploration Rover. Meridiani Planum was originally chosen due to the spectral signature of hematite observed by the Thermal Emission spectrometer (*Christensen et al.*, 2001). However, in addition to identifying hematite in the form of aqueously derived concretions, Opportunity detected the surrounding bedrock to be rich in sulfate minerals (*Squyres et al.*, 2004b). Several indicators, including large-scale cross-bedding, dissolution vugs, and the hematite concretions indicate that the Meridiani bedrock largely formed by aeolian transport and diagenetic alteration by groundwater, with limited occurrences of shallow subaqueous transport (*Grotzinger et al.*, 2005). Subsequently, the OMEGA spectrometer has detected sulfate minerals in other regions of Mars from orbit (*Gendrin et al.*, 2005). Initially, large sedimentary outcrops were confirmed in a broad region from Valles Marineris through Margaritifer Terra to Meridiani Planum. Within the Margaritifer Terra region, TES has since detected hematite with a similar spectral signature to that found at Meridiani, while OMEGA also confirmed this association within many of the sedimentary outcrops in Valles Marineris (*Glotch and Rogers*, 2007; *Bibring et al.*, 2007). This recurring pattern suggests a series of common formation and events that were widespread across this region of Mars. Correlative units may also exist in the lower part of the mound in Gale crater (*Milliken et al.*, 2009), one of the candidate landing sites for MSL.

1.1.4 Arabia Terra Intracrater Mounds

A third class of sedimentary rocks on Mars is not noted for its strong mineral signatures. Rather, deposits of stratified material of unknown mineralogical composition are found widely across Mars, particularly in Arabia Terra. Possibly related materials occur in Gale crater and in the extensive Medusa Fossae Formation in southern Elysium Planitia. Many of these light toned outcrops were first described in MOC data by *Malin and Edgett* (2000). Chapter 4 focuses on several of these mounds in western Arabia which are found to contain quasiperiodic bedding. *Fergason and Christensen*

(2008) described several mounds with similar characteristics in eastern Arabia Terra, finding thermal inertias consistent with weakly indurated material. *Ruff et al.* (2001) performed a detailed analysis of the "White Rock" feature in Pollack crater, finding a flat spectrum with no distinct mineral signatures. Both studies suggest that these characteristics are intrinsic to the material, and not a result of a dust mantle. Both studies, as well as the work presented in chapter 4, suggest aeolian dust accumulation as the preferred mode of deposition.

1.1.5 Midlatitude Mounds

A small number of locations in the southern midlatitudes have significant accumulations of stratified material, responsible for the peak at -55° in Figure 1.2. The two most prominent occurrences are found in Galle and Spallanzani craters. These deposits are relatively poorly studied via spectroscopy, partly due to colder temperatures at higher latitudes limiting thermal emission. A particularly interesting feature of the Galle crater mound is the presence of numerous angular unconformities at its base, suggesting many intervals of alternating erosion and deposition. The presence of angular unconformities likely rules out strongly gravity-controlled formation processes, such as lacustrine deposition.

1.1.6 Pyroclastic Deposits

Although perhaps not strictly sedimentary in origin, pyroclastic deposits are included here based on their ability to form intricately stratified deposits which can be difficult to distinguish from other sedimentary rocks. Extensive volcanism is known to have occurred on Mars, as evidenced by widespread volcanic flows and edifices. Explosive eruptions are expected to have occurred in Mars' history, and models have estimated how volcanic ash should fragment and be deposited on the surface (*Wilson and Head*, 2007). A few examples of pyroclastic deposits have been identified from orbit, although they are not conclusive (*Hynek and Phillips*, 2003; *Wilson and Head*, 2004). Several features have been linked to explosive volcanism at the Spirit rover landing site in Gusev crater. These include a deposit known as Home Plate, which is the focus of chapter 3. Although

an aeolian origin is the most common interpretation of the large-scale cross-bedding seen at the Opportunity landing site, a pyroclastic formation has also been proposed (*McCollom and Hynek*, 2005).

1.2 Data and Tools Used

The work presented in this thesis was only made possible by the arrival of several spacecraft at Mars, and several years of observation by their scientific instruments. Here, I briefly review those on which I have relied most heavily for the analyses that follow. In addition, I describe several of the software tools which I have used in deriving stereo topographic models of the Martian surface.

1.2.1 Mars Global Surveyor

Chapter 2 deals primarily with data from the Mars Global Surveyor (MGS), which was launched in 1996 after a 20 year hiatus in Mars exploration (*Albee et al.*, 2001). MGS (literally) reshaped our view of the planet with its powerful suite of analytic instruments. MGS operated in a near polar 87° sun-synchronous orbit. With its instrument deck initially nadir pointed, the spacecraft was reoriented in 2001 to a pitch of ∼16° to conserve fuel, providing easy opportunities for stereo imaging (*Ivanov*, 2003). After nearly a decade of observations, the spacecraft was finally lost in November 2006.

The Mars Orbiter Camera (MOC) was the first high-resolution imaging system to orbit Mars. MOC was a "pushbroom" line scanning camera, which built up images in the flight direction as the spacecraft moved over the surface. Although the instrument also contained two wide-angle context cameras, this work relies heavily on images from the MOC Narrow Angle (MOC-NA) camera. The camera itself consisted of a 3.5 m focal length telescope with a 2048 × 1-element CCD array, and acquired images in the 500–900 nm wavelength range. At full resolution, images were acquired at roughly 1.5 m/pixel, although 2 × 2 or 4 × 4 summing modes were frequently employed (*Malin et al.*, 1992). Image swaths are roughly 3 km wide on the surface. Although many stereo image pairs were acquired by MOC, the MGS spacecraft was not designed specifically for this capability.

As a result, vibrations on the spacecraft often induced high-frequency camera pointing errors, which need to be taken into account in derived topographic models.

A second instrument, the Mars Orbiter Laser Altimeter (MOLA) acquired the most accurate global topographic map of Mars to date. The instrument consisted of a 1064 nm laser altimeter operating at 10 Hz. Individual shot points have a vertical accuracy of 1 m and a footprint size of roughly 150 m. The full data set has a horizontal resolution of hundreds of meters to a few kilometers (*Smith et al.*, 2001). The MOLA data set represents the current "gold standard" for Martian surface topography, and is a critical starting point for many of the investigations presented in subsequent chapters.

1.2.2 Mars Exploration Rovers

The twin Mars Exploration Rovers (MER), which arrived at Mars in 2004, are essentially the first field geologists on Mars. Data from the Spirit rover makes up the basis for chapter 3. Long outliving their nominal 90 sol missions, Spirit and her twin Opportunity remain operational over five years later at Gusev crater and Meridiani Planum respectively. The science payloads of the rovers combine several remote sensing and *in situ* instruments that provide an integrated scientific view of the landing sites. Some of the chemical and mineralogical results are summarized here, although I focus on the imaging packages. Each of the rovers includes three cameras nominally dedicated to science, and six additional engineering cameras. All of the cameras on the spacecraft utilize the same 1024 $\times$ 2048 element frame-transfer CCDs (1024 $\times$ 1024 imaging area), and include onboard subframe and compression capabilities (*Squyres et al.*, 2003).

The Pancam instrument is the primary MER science imaging experiment, consisting of two stereo cameras located on the rover mast. The cameras are separated by a 30 cm baseline with a 1° toe-in angle, providing accurate range information out to 100 m or more. The combined cameras have 14 visible and near-infrared filters ranging from 400 nm to 1100 nm. Stereo imaging is available in both red (L2/R2 filters) and blue (L7/R1) wavelengths (*Squyres et al.*, 2003). While it is primarily a science instrument, Pancam often aids in rover navigation as well.

The Microscopic Imager (MI) is mounted on the rover arm for *in situ* analysis of rock and soil targets. The MI has a single bandpass visible filter with a range of 400–680 nm. The camera has a 3 cm field of view, providing an approximately 30 µm pixel scale. Typically, several images at a range of distances from the target are acquired, to achieve focus over a wide depth of field (*Squyres et al.*, 2003).

The engineering cameras on the MER spacecraft consist of front and rear hazard avoidance cameras (Hazcams) mounted beneath the rover deck, along with the mast-mounted navigation camera (Navcam). Each consists of a pair of stereo cameras, with a baseline separation of 10 and 20 cm for the Hazcams and Navcam, respectively (*Maki et al.*, 2003). Although these are nominally engineering cameras, they often acquire scientifically useful data.

1.2.3 Mars Reconnaissance Orbiter

Mars Reconnaissance Orbiter is the most recent orbiter to have arrived at Mars in 2006, and remains a powerful tool in orbit around Mars. Hosting several high data-rate instruments, it has already sent back Terabits of information, far surpassing all previous missions combined. A large fraction of these bits have been acquired by the High Resolution Imaging Science Experiment (HiRISE), the highest resolution camera ever flown to Mars. Also a pushbroom camera, HiRISE improves on MOC by nearly an order of magnitude in resolution, sampling the surface of the planet at 30 cm/pixel. The detector consists of 14 CCDs, with 10 red-filter detectors aligned linearly to create monochromatic images. Two each blue-green and near-infrared detectors provide color imaging over the center 20% of the swath. With 2048 $\times$ 128 element CCDs, the instrument utilizes Time-Delay Integration (TDI) to achieve high signal to noise at such small pixel scales. Red CCDs overlap slightly to create 20,000-pixel-wide swaths when fully assembled, covering roughly 6 km of the surface (*McEwen et al.*, 2007). Because MRO is a highly stable platform, camera pointing jitter is small, allowing highly precise derivation of topography from stereo image pairs. Further, by using the 24-pixel overlap between CCDs, it is now becoming possible to model and remove the effects of jitter from the images before deriving topography.

1.2.4 Software Tools

I have had the good fortune of access to several stereo correlators over the course of these studies. Below, I briefly summarize these software packages and their relevant features.

1.2.4.1 VICAR

Chapter 2 makes use of the VICAR software package, developed at the Jet Propulsion Laboratory (JPL) specifically for processing and analyzing spacecraft data. Specifically, I have relied on the tracker3 routine discussed by *Ivanov and Lorre* (2002). Tracker3 is a 2-D correlator based on Gruen least-squares minimization. Adjustable parameters include the correlation patch and window sizes, as well as several different search algorithms. *Ivanov* (2003) developed the essential software to transform tiepoints from image-space to geographic coordinates for MOC images, based on the SPICE telemetry data.

Chapter 3 relies on the stereo processing pipeline developed for the MER mission by the Multi-mission Image Processing Laboratory (MIPL) at JPL. This MIPL pipeline was also developed for the VICAR platform at JPL. Because of the fixed relative orientation of the stereo cameras on the rovers, images can be linearized in azimuth and elevation to allow fast 1-D correlation. For images acquired at different mast or rover positions, 2-D correlation is also available. The 2-D correlator employs several stages of image matching at progressively higher resolutions to increase computation speed (*Alexander et al.*, 2006).

1.2.4.2 Socet Set

Socet Set is a stereo-processing software package developed by BAE Systems, used here primarily for HiRISE data (discussed in chapter 4). *Kirk et al.* (2008) have developed pushbroom sensor models and methods for Socet Set which can handle both MOC and HiRISE data, and which we have implemented at Caltech. The software includes a sophisticated stereo correlation technique, which is capable of adaptively optimizing its algorithm to a variety of terrains. Data are tied to the MOLA data set using both gridded data and individual shots. Triangulation of MOLA-registered

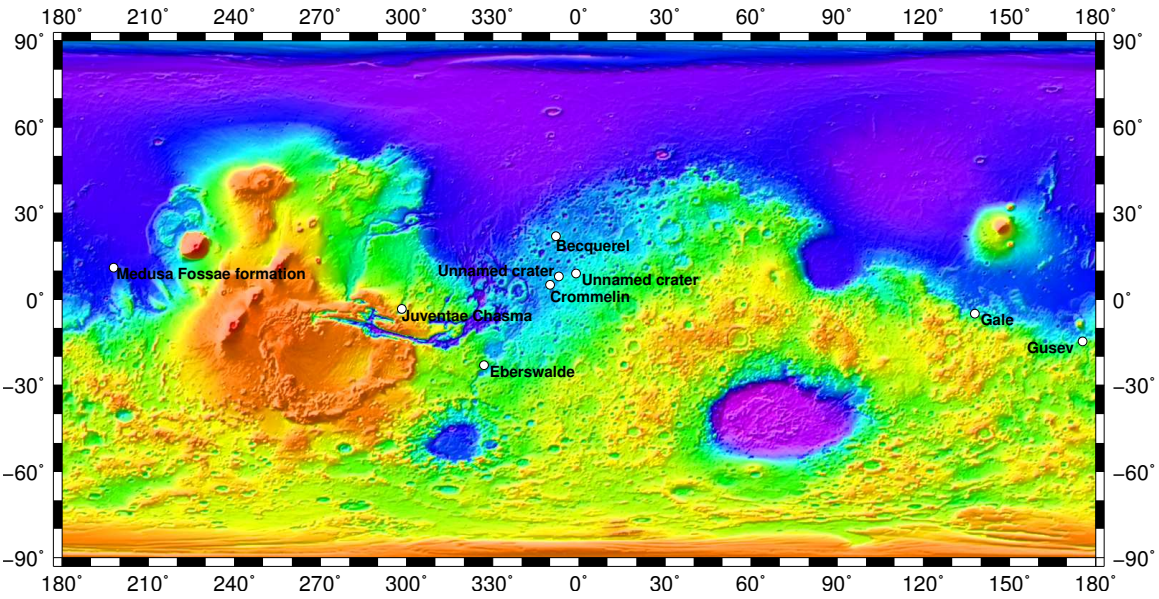

Figure 1.3: Map of important sites discussed in this thesis. Eberswalde crater is the focus of chapter 2, while the Spirit rover landing site in Gusev crater is discussed in chapter 3. All other labeled sites are presented in the context of rhythmic stratigraphy on Mars, the topic of chapter 4.

tiepoints allows the camera positions and pointing vectors to be refined, improving the final result. Multiple-pass correlations and efficient search methods allow 2 m topographic maps to be generated from gigapixel HiRISE images in a matter of hours (*Kirk et al.*, 2008).

1.3 Overview

The structure of the remaining chapters of this thesis is divided into three geologic investigations of martian sedimentary rock outcrops. All of the studies are united by the technique of using high resolution stereo topography to derive quantitative information about geologic formation and evolution. The locations of all of the sites which will be discussed are shown in Figure 1.3. Chapter 2 examines perhaps the best-preserved fluvial delta exposed on the surface of Mars within Eberswalde crater. MOC stereo topography is used to constrain the mode and timescale of formation of the deposit from the ∼80 m of exposed stratigraphy. Chapter 3 focuses on the enigmatic cross-stratified feature known as Home Plate encountered by the Spirit Mars Exploration Rover within Gusev crater. Data from several of Spirit's instruments are combined to quantify the geologic structure and sedimentology of Home Plate and nearby outcrops. Finally, chapter 4 presents the discovery

of several rhythmically bedded outcrops of sedimentary rock across Mars. Several occurrences are clustered in western Arabia Terra, including those in Becquerel and Crommelin crater, along with two unnamed craters. Additional identifications are presented within Gale crater and the Medusa Fossae formation in Elysium Planitia. Counterexamples of aperiodic stratigraphy are also discussed at Eberswalde crater and Juventae Chasma. HiRISE stereo topography is used to obtain stratigraphically corrected bed thickness measurements. Further, time-series analysis of corrected image brightness and topographic slope profiles is used to confirm periodicities within the stratigraphy.

Chapter 2

Stratigraphic Analysis of the Distributary Fan in Eberswalde Crater

Originally published in:
Lewis, K. W., and O. Aharonson (2006), Stratigraphic analysis of the distributary fan in Eberswalde crater using stereo imagery, *J. Geophys. Res.*, *111*(E06001), doi:10.1029/2005JE002558

Abstract

The eroded remains of a fluvial distributary network in Eberswalde crater are uniquely well preserved among similar structures on Mars. A quantitative analysis of the exposed stratigraphy has been performed to investigate the internal structure of the deposit. Using topographic information derived from stereo pairs of high-resolution Mars Orbiter Camera images, we have for the first time quantified the orientation of individual layers exposed along the distal end of the distributary network. In combination with topographic data from the Mars Orbiter Laser Altimeter, we have examined plausible scenarios for the formation of this structure. We find that the evidence is inconsistent with formation both as an alluvial fan and as a progradational delta. Instead, we find that an aggradational delta best fits the observed characteristics of the channel network and the Eberswalde basin as a whole. We conclude that the delta likely formed not in a stable long-lived lake, but over the course of a small number of shorter lacustrine episodes, which were not sustained at equilibrium conditions.

2.1 Introduction

The history of water on Mars remains a subject of vigorous debate. Evidence of hydrologic activity exists in diverse forms and on many scales around the planet (*Carr*, 1996). However, it remains unclear exactly how much water was present on the surface and for how long, and whether sources of water were recharged by precipitation (*Squyres and Kasting*, 1994; *Craddock and Howard*, 2002). Fan-shaped deposits at valley termini have been recognized as valuable pieces of evidence for answering these questions, and their implications at the global scale have been discussed by *Irwin et al.* (2005) and others. The distributary network shown in Figure 2.1a) is a unique sedimentary structure that provides new information regarding these questions. This fan-shaped deposit, fed by meandering channels, has been interpreted as strong evidence of persistent fluvial activity (*Malin and Edgett*, 2003; *Moore et al.*, 2003). The most prominent example of meandering is shown in Figure 2.1a), and several instances can be found along other channels in the image. The fan (located at 23.8° S, -33.6° E) is situated within Eberswalde crater (formerly known as Holden NE crater), a severely degraded, shallow basin which has been buried beneath ejecta from the Noachian-age Holden crater, immediately to the southwest (*Scott and Tanaka*, 1986). The distributary channels overlie this ejecta, and are estimated to be of Late Noachian age (*Moore et al.*, 2003). Previous estimates of formation timescales for this structure have ranged from as little as decades (*Jerolmack et al.*, 2004), to as long as several million years (*Bhattacharya et al.*, 2005).

We have previously described the extraction of topographic data from a Mars Orbiter Camera (MOC) Narrow Angle stereo pair at the edge of the fan (*Lewis and Aharonson*, 2004), via the method of *Ivanov and Lorre* (2002). These high-resolution images and topographic models from Mars Global Surveyor (*Albee et al.*, 2001) allow unprecedented studies of meter-scale features (*Malin and Edgett*, 2001). MOC images have been used elsewhere to acquire high-resolution topographic information (*Kirk et al.*, 2002). Here, analysis of the topographic data is presented, with a focus on the structure of the layers exposed at the distal end of the fan. The morphology of these layers records the depositional and erosional processes which formed the Eberswalde fan. There are dozens of layers exposed along the edge of the landform, and they occur in a wide range of outcrop

orientations and elevations. This presents a rare opportunity for studying the overall architecture of the deposit, which preserves both spatial and temporal variations in the depositional environment. Stereo-derived topographic data is used to achieve a quantitative assessment of the structure of these layered materials.

2.2 Geomorphic Observations

An important aspect in deciphering the geologic history of the Eberswalde fan lies in determining the severity of aeolian erosion to which the deposit has been subjected. *Jerolmack et al.* (2004) estimated that the original volume was five times greater than the currently preserved remains. This greater volume is required if the sediment was deposited in an alluvial fan which followed a smooth profile to the crater floor. This scenario also requires a 35 km erosional retreat of the distal end of the distributary system. *Jerolmack et al.* (2004) point to the scattered fluvial deposits around the floor of Eberswalde in support of a greater original extent of an alluvial fan, although they concede the evidence does not definitively discriminate between alluvial and deltaic scenarios. However, many of these channels have elevations and flow directions inconsistent with a direct relationship to the main distributary network. The alternative hypothesis is that the deposit represents the remains of a delta that built into a lake which partially filled Eberswalde crater at some point in its history. The deltaic scenario requires far less aeolian erosion, due to the fact that the subaqueous margin of a delta can be much steeper than the profile required here for a purely subaerial alluvial fan. In this case, the current scarp at the edge of the structure would be more representative of the origin distal limit of the fluvial channels, as opposed to a purely erosional feature.

While we find no solid evidence of a much more extensive alluvial fan, some observed features do suggest the modern scarp is close to the original distal limit of the deposit, favoring formation as a delta. In several places past the current margins of the distributary channels, other fluvial deposits are situated within the distance expected for a purely subaerial alluvial surface. In one instance, fluvial deposits to the northeast of the fan lie $\sim$1.5 km away ("A" in Figure 2.1a)). Using the MOC stereo topographic data described in detail below, it is clear that these channels originally flowed

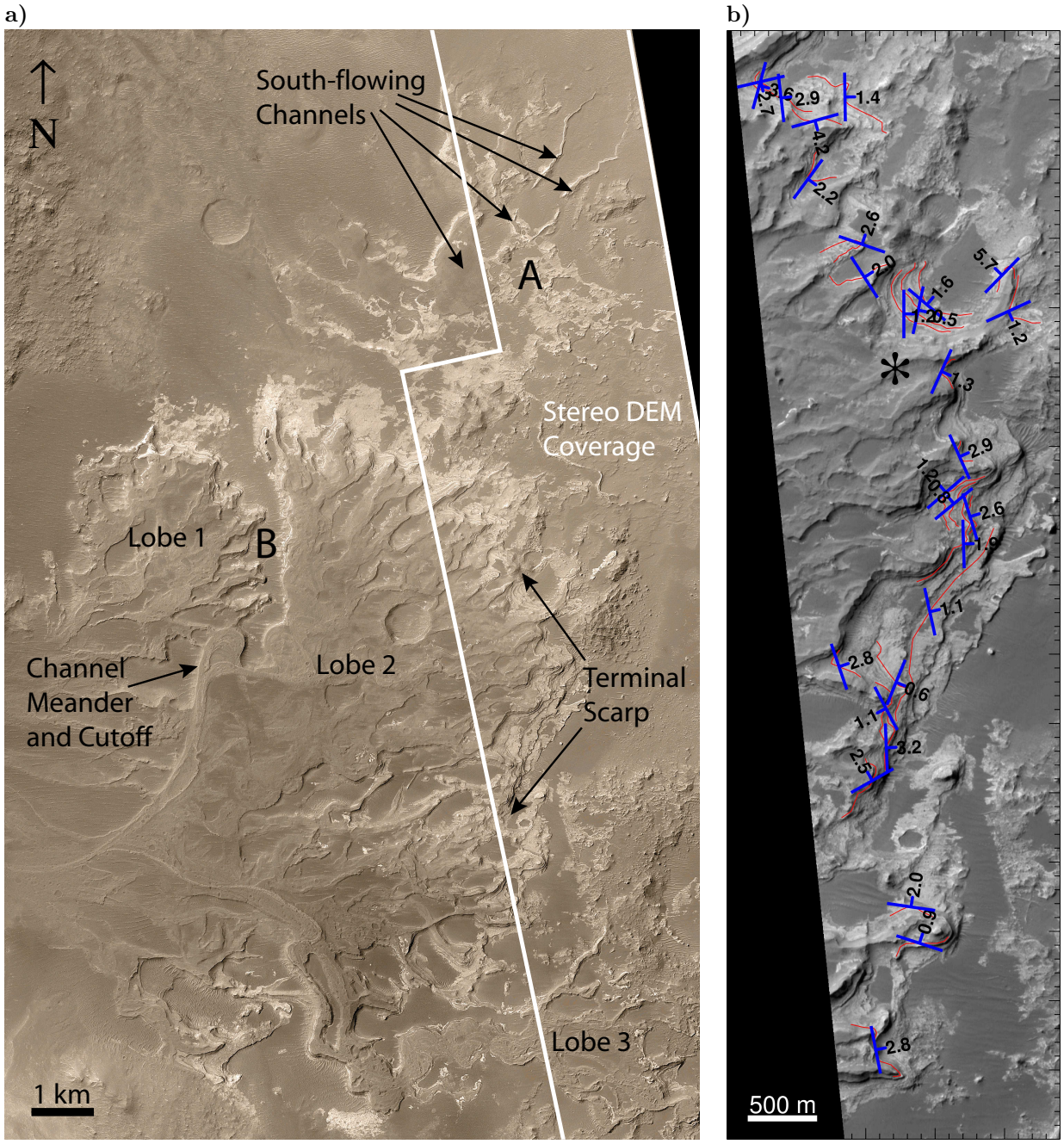

Figure 2.1: **a)** MOC Narrow Angle mosaic of the distributary network in Eberswalde crater. This landform is comprised of three main lobes, numbered here in inferred depositional sequence. Evidence of channel meanders and cutoffs can be seen in several places, suggesting sustained flow. Area "A" shows a group of south-flowing channels adjacent to the much larger distributary network. A gap between lobes 1 and 2 where the layered deposits are discontinuous is labeled "B". These two depositional forms provide evidence that the Eberswalde channel network was never significantly more extensive. Stereo coverage in this area is shown, covering the finely layered outcrops along the terminal scarp (Mosaic created by Malin Space Science Systems). **b)** Map of layer profiles used in this analysis. Red lines indicate the path of each profile, along a continuous layer outcrop. Blue symbols show the corresponding strike direction and values the dip magnitude. An area where a vertical sequence of layers have a consistent eastward dip, is denoted by "∗". Several other areas also exhibit consistent trends among adjacent layers. Four additional profiles, along outcrops farther to the south on lobe 3, are not shown on this plot. Minor tick marks denote 100 m intervals.

to the southwest, originating from a distinct source on the northern wall of the crater. There are several plausible depositional scenarios which may explain the relationships between the southwest-flowing channels and the larger, northeast-flowing distributary network. We assume that aeolian erosion is the final stage of the geologic sequence, postdating the Noachian fluvial activity, and likely continuing in the present era. Moreover, it is likely that all fluvial deposits were emplaced before significant erosion had occurred. However, the order of deposition of the large channel network and the smaller southwest-draining channels nearby is unclear. If these channels were deposited after, or concurrent with the larger distributary network, they place a firm constraint on its original extent. If the southwest-draining channels were instead deposited first, the constraint is more ambiguous. However, a differential erosional mechanism would need to be invoked whereby several tens of meters of sediment from the large distributary network was stripped away, yet these delicate channels (of order 10 m high and 30 m wide) beneath remained well preserved. Such differential resistance to erosion would require a significant difference in cohesiveness or grain size, for example, though there is no independent evidence for such a difference.

As a second key relationship, the two largest lobes of the fan are separated by only hundreds of meters in places ("B" in Figure 2.1a)). Thus, using the labels in Figure 2.1a), the potential extent of channels in lobe 1 is limited by later channels in lobe 2. The distance between the lobes, however, is too great for this truncation to have been caused by fluvial erosion of lobe 1 by lobe 2 channels. This example is particularly difficult to explain by simple headward retreat of an alluvial deposit, as erosion here would be near the center of the currently preserved structure. Instead, the current limit of the channels in lobe 1 is likely representative of their original termini.

The two examples described here outline a scenario of fairly limited aeolian erosion within Eberswalde. From these observations, we suggest that the 10–15° distal slope of the fan, as measured from stereo data, is not primarily an erosional feature, but is instead a remnant of the original depositional form. Modest post-fluvial erosional retreat of the scarp is possible, but is limited by this argument to be <1 km or so in lateral extent.

2.3 Stereo Topography

2.3.1 Methodology

For this study we have used high-resolution MOC narrow-angle images from the MGS spacecraft. These images have a maximum resolution of around 1.5 m/pixel and are typically 3 km wide. MOC has taken images of the Mars surface both in nadir and offnadir orientations. Where such coverage exists, high-resolution stereogrammetry is possible.

Stereo images are processed according to the technique developed by *Ivanov and Lorre* (2002) and *Ivanov* (2003). To begin, radiometric calibration of the images is performed using the Integrated Software for Imagers and Spectrometers (ISIS) software package. Calibrated images are then rectified using VICAR tools and the MGS telemetry data and then adjusted manually to bring them into a more precise alignment. When the stereo pair has been properly aligned, an automatic correlator is used to locate tiepoints between the two images. Tiepoints are typically collected in a 2-pixel grid, and hundreds of thousands are generally collected for a given pair of MOC images. VICAR routines are again used to extract elevation data from the tiepoints.

Once the elevation data has been collected, Digital Elevation Models are created by regridding, interpolating, and projecting the elevation data. The final DEMs are gridded at a resolution of 6 m/pixel in the horizontal direction. In the vertical direction, accuracy of the data is approximately 1–2 m. The DEMs in the Eberswalde region that have been used in this study include a component of the jitter reported by *Ivanov and Lorre* (2002) and *Kirk et al.* (2002). This was removed by separating the parallax between the images into its alongtrack and crosstrack components. The vibration onboard MGS is evidently limited to the alongtrack direction, so that any parallax in the crosstrack direction is free from jitter. Long wavelength tilts between the MOC stereo data and MOLA topographic measurements are less than 0.1°, and are difficult to constrain further due to the sparse distribution of MOLA points over the study area. As any discrepancies of this nature would be small compared to the topographic slopes being studied, the stereo DEM was not adjusted to conform to the MOLA dataset.

2.3.2 Observations

Two stereo pairs were used for our study, of images E14-01039/E23-00003 and E14-01039/E22-01159. The area for which stereo coverage is available is shown in Figure 2.1a). The DEMs produced in this area have good coverage over most of the original images. The automatic correlator fails to find matches in some particularly smooth or shadowed regions, but this is uncommon in areas with high-contrast features, including the layered outcrops.

The stereo-derived DEMs were used in conjunction with the original MOC images to extract elevation segments along the edges of exposed layers. Dozens of individual segments were selected manually, each ranging from a few hundred meters to over 1 km in length. Data was only taken where a layer outcrop was clearly continuous; no attempts were made to connect or extend layers where they become indistinct in the images. Efforts were made to choose layer exposures with some natural curvature in the horizontal direction, to provide more accurate constraints on the three dimensional geometry of the layer. Conversely, a linear segment provides no information in the direction perpendicular to the line. Otherwise, segments were taken from all areas within the DEM. For our analysis, we used 40 such segments along the margin of the layered deposits.

Since each segment extracted here is much smaller than the overall extent of the fan, it is assumed that the layers should be very close to planar on this scale. To evaluate this hypothesis, and to gain a quantitative measure of the attitude of the layers, a plane was fit to each profile using linear regression. From the derived coefficients, the dip direction and slope are computed, along with their corresponding error estimates based on confidence intervals. While a more mathematically precise error analysis can be derived than the one used here (R. Phillips, pers. comm., 2005), our method is sufficient for discriminating poor fits. Segments for which the corresponding dip azimuth had an error of more than 30°, or for which the slope had an error of more than 1° were eliminated from further analyses. Roughly 80% of our sample was within these limits, while the remaining 20% fell outside of at least one of the constraints. The wide error bounds for some profiles can be traced mostly to noise in the DEM, or to a lack of significant curvature in the segment, which produces a poorly constrained fit. However, the large majority of continuous layer outcrops in the fan are well

approximated by a plane. Those that are constrained by the fits according to the criteria above are shown in Figure 2.1b).

The layered nature of this formation permits analysis of both vertical and lateral trends in addition to measurements of the structure as a whole. The mean gradient of all of the measured layers which could be well fit is 2.1°. Figure 2.2 shows a histogram of the observed slopes. The dip angles measured are consistently shallow, and have a standard deviation of 1.1°. The average dip direction is roughly eastward, parallel to the channel direction in this part of the fan, though there is wide variation within the data set as indicated by the strike-dip marks in Figure 2.1b). One trend among the sampled layers is that in many cases the layers have a component of dip in the direction perpendicular to the surrounding channels, in addition to the expected down-channel slope. Several of the layers exhibit this trend over hundreds of meters. No signs of postdepositional deformation are obvious from MOC imagery, indicating the cross-channel slopes are original depositional attributes. The reason for these strike directions is unclear. However such an attribute is consistent with the complex architecture associated with deltaic deposition, where erosional surfaces, levees and overbank deposits all lead to nonparallel strata (*Reading*, 1996; *Prothero and Schwab*, 2004). A second important trend is lateral and vertical consistency of the measured dips. One notable occurrence of this trend is marked with "$*$" in Figure 2.1b). Several layers here exhibit comparable eastward dips, at different outcrops and at varying levels in the stratigraphic sequence. This may indicate long-standing flow patterns here and in other outcrops where this trend is found. Regions where strikes and dips are more widely scattered may record a more dynamic depositional history.

2.4 Basin Analysis

While stereo-derived topographic data is available over a restricted area, Mars Orbiter Laser Altimeter (MOLA) data provides a far more extensive, though coarser coverage of the entire basin into which the fluvial network once drained. Here, the 128 pixel per degree (ppd) MOLA gridded elevation data is utilized (*Smith et al.*, 2001). It has been hypothesized that the fluvial deposits in Eberswalde have undergone significant burial and exhumation, accounting for the relative lack of

cratering on presently exposed surfaces (*Malin and Edgett*, 2003; *Moore et al.*, 2003). While this scenario would complicate assessing the topography at the time of emplacement of the fluvial deposits, evidence for the exposure of the original depositional surface is present in the form of MOC images within the basin which reveal other fluvial channels in several places on the floor of the crater, as in R07-00821, R07-01352, E21-00076, and E23-00003. These deposits have been mapped based on available MOC imagery, and are shown in Figure 2.3. Consequently, it is likely that the present topography is similar to that at the time of fluvial activity over most of the basin. This argues against significant infilling as well as large degrees of aeolian erosion of the basin floor in the time since fluvial activity ended in Eberswalde. Furthermore, it is likely that the main delta and the channel deposits found elsewhere in the crater are genetically related. There is no evidence to indicate significant gaps in time between depositional episodes, such as intervening (and morphologically distinct) strata between fluvial deposits. When they occur in close proximity to each other, all channels and their associated deposits appear to share a common underlying surface. In addition, all fluvial deposits have been subject to roughly similar degrees of aeolian erosion and cratering, which argues for a similar age and geologic history. This assumption places an additional constraint on the size of any long-standing lake, as all channel deposits are expected to have formed subaerially. With the assumption that other fluvial deposits are genetically related to the main delta, and therefore show that the basin topography is similar to that at the time of deposition, lake volume estimates are derived from the MOLA 128 ppd DEM. The -1400 m contour is approximately the highest lake level which does not have higher elevation than clear fluvial deposits, and is also the level at which the uppermost channels of the main delta discharge. At this contour, the calculated basin volume is approximately 24 km^3. *Moore et al.* (2003) estimated the mean discharge of the distributary system, using observed channel width and meander wavelengths, as well as contributing basin size. Their estimated mean flow rate was 700 m^3/s. Using these estimates, the basin would fill to -1400 m within 1.2 years of sustained flow, and begin flooding the delta. This simple calculation ignores losses due to evaporation and infiltration of water into the subsurface, as the conditions at the time of formation have large uncertainties. Fill times for various higher contours within the basin are

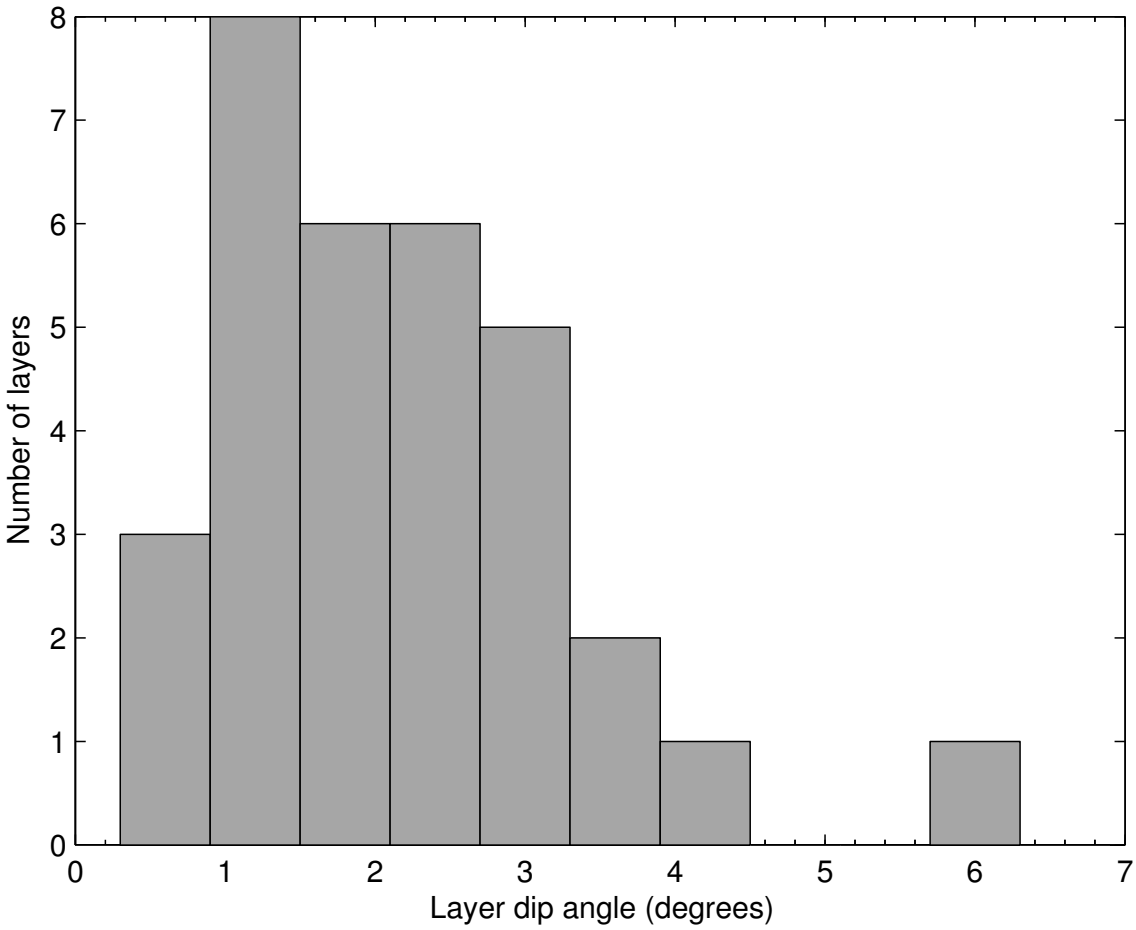

Figure 2.2: Histogram of observed slopes, as determined from the stereo DEM. The mean dip of these layers is 2.1°.

shown in Figure 2.3, but all are on a timescale of years. A delta would have to be rapidly aggrading in order to maintain equilibrium with a rising base-level, if such a flow rate was sustained for months to years. This depositional model is in contrast to one of a standard progradational delta, which occurs under static base-level conditions.

2.5 Implications for Formation

The distributary deposits in Eberswalde crater were formed either as an alluvial fan or as a delta. However, the alluvial fan hypothesis is found to be unsatisfactory. Strata in a simple alluvial fan should grade gently onto the underlying surface at the distal end, which would require that the

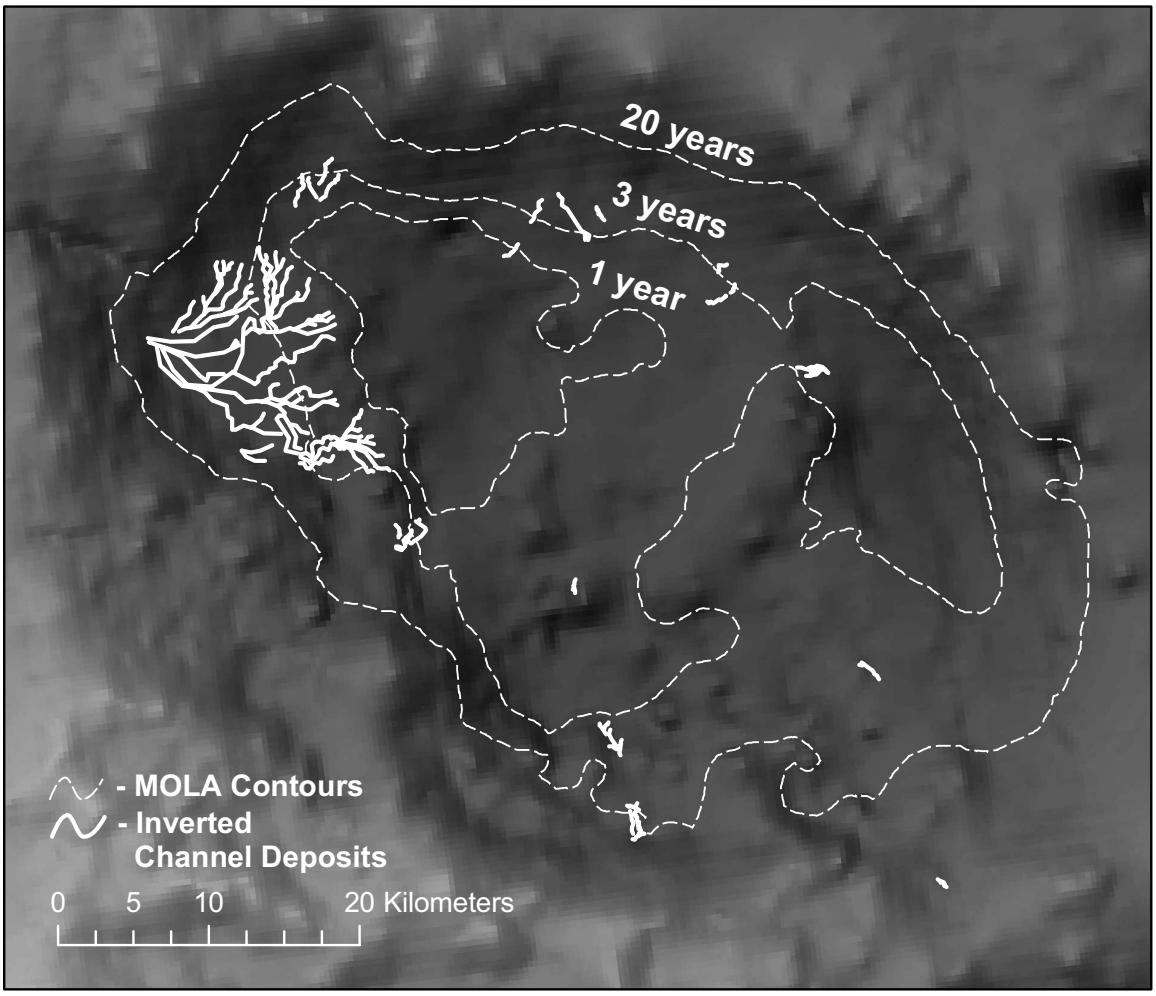

Figure 2.3: Estimated time to fill Eberswalde crater to various contours, based on MOLA 128 pixel per degree map. Inverted channel deposits are shown in white. The large channel network on the west side of the crater is the layered deposit discussed here. Note the other channel deposits found around the floor of Eberswalde, as highlighted in the figure. Contours denote fill times based on the 700 m^3/s estimate of flow rate into the crater by *Moore et al.* (2003). A theoretical paleolake at the 3-year level or higher covers many of these deposits, indicating the water level was below this contour at the time of deposition.

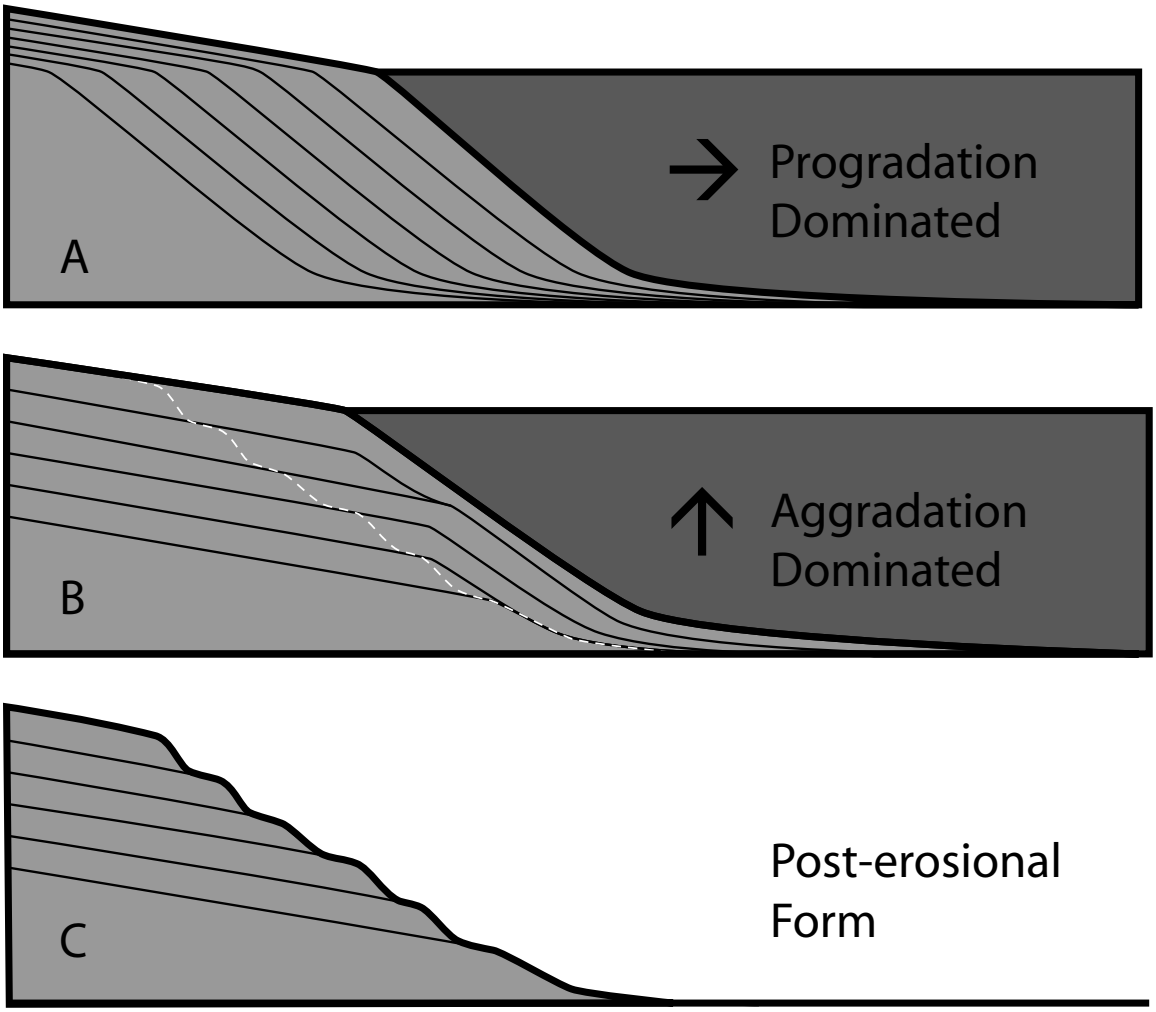

Figure 2.4: Schematic cross section of a progradational versus an aggradational delta. A) The bulk of a progradational delta will be made of steeply dipping foresets. This occurs under static base-level conditions, as coarser sediment is transported to the ends of distributaries and deposited on the delta slope. B) In an aggradational delta, the bulk of the sediment load will be deposited in shallower topset beds, as accommodation space increases due to a rising base-level. C) Hypothetical cross section of the eroded structure seen in Eberswalde crater, which may have been deposited as an aggrading delta.

deposit in Eberswalde was originally far more extensive at the time of deposition. With a roughly 100 m stack dipping at 2° or less, these deposits would have to have extended further by several kilometers. *Jerolmack et al.* (2004) estimate an original extent as large 35 km past the current terminus of the layers, with the assumption of an alluvial profile. Spatial relationships between the distributary network and nearby fluvial deposits, as well as between different sets of channels within the structure, argue against this depositional origin, as outlined above. It is noted that the term "fan delta" has been used to describe an alluvial fan which terminates at a body of water. However, much of the distinction lies in the nature of the feeder system, as opposed to the stratigraphy which is the focus of this work (*Postma*, 1990). Due to the presence of a standing body of water, the stratigraphy is more similar to deltas than purely subaerial alluvial fans (*Prior and Bornhold*, 1990; *Dabrio*, 1990). Therefore, fan deltas are considered to be within the broader category of deltas for the purposes of this analysis.

The primary difference between an alluvial fan and a delta is the presence of a prodelta lake in the latter case. A resulting morphologic distinction lies in the bedding orientations. In the case of a delta, the bedform is tripartite, including more steeply dipping foreset beds. These beds can exhibit a range of steepness, depending on the nature of the sediment and depositional environment (*Summerfield*, 1991). Foreset beds are often inclined at or near the angle of repose for coarse-grained Gilbert-style deltas, exhibiting a dip of up to 30° in some cases, but can be much lower in the case of very fine sediment, down to less than 1° (*Reading*, 1996). However, the presence of very shallow foreset beds would require a greater degree of erosion, and is not favored by the same argument as that for an alluvial fan. Foresets are formed as flow velocity declines rapidly upon entering a standing body of water and coarser sediment can no longer be moved or kept in suspension (*Nichols*, 1999). In a classic progradational delta, foreset beds make up the bulk of the volume of the delta, as shown in Figure 2.4a) (*Prothero and Schwab*, 2004). In the case of the Eberswalde formation, these steeply dipping layers would be exposed at the distal end, even after a modest amount of erosion has occurred on the delta front. However, the slopes of the beds measured here are uniformly shallow. These layers cannot simply be low-angle foreset beds, as this scenario is again vulnerable to the

same evidence against formation as an alluvial fan. Therefore, the stratigraphic data argues for a different depositional origin.

One resolution to the dual problems of small basin size and observed bedding orientation is an aggradational delta. As there is no outlet from Eberswalde crater at the level of the channels, any steady flow at the rates estimated by *Moore et al.* (2003) should produce standing water in the basin. Due to the size of this basin, it would fill rapidly under these flow conditions. To accommodate this base-level change, much of the sediment supply would be deposited in the form of shallow topset beds. This process is expected when the vertical increase in the accommodation space of a delta, caused by rising water levels, is comparable to or greater than the sediment flux into the system. Aggradation-dominated deltaic growth has been described by *Milton and Bertram* (1995); *Muto and Steel* (1992), and investigated experimentally by *Muto* (2001). These studies highlight the fact that, in a system with a constant base-level rise and a constant sediment supply, a delta must eventually transition to an aggradation-dominated state, with deposition occurring mainly in topset beds. Figure 2.4 illustrates the two endmembers discussed here for deltaic growth. In the aggradational delta scenario, subsequent erosion at the distal end could strip away the thinner foreset layers, leaving a scarp of exposed topsets. If this is the case, there appears to have been relatively little transgression or retreat accompanying the base-level rise. The complete stack of layers is exposed over a relatively short lateral distance, implying a fairly static shoreline. The aggradational model is buttressed by the fact that the most recent channels in this structure are also the highest topographically as measured from stereo data, and also noted by *Jerolmack et al.* (2004). Evidence of down-cutting, which would indicate a base-level drop, has not been identified. This implies that deposition occurred mostly during periods dominated by rising lake levels. Also, the lack of widespread down-cutting suggests a limited number of episodes for fluvial and lacustrine activity within this crater. As it is implausible that the entire deposit was emplaced on a timescale of months to years, as implied by the estimated basin filling time, this may be evidence for a much smaller mean flow rate over long timescales, and/or the importance of loss mechanisms from the system (mainly evaporation and infiltration) which are not included in our estimates. Alternatively,

evidence of down-cutting is simply not exposed at the surface presently, though it may exist in lower layers. In this case, erosion could have occurred alternately with aggradation over the course of several filling and drying cycles.

The small volume of Eberswalde crater relative to estimated flow rates provides a rough constraint on the formation timescale for this delta. *Malin and Edgett* (2003) estimated the current volume of the sediment within the delta to be approximately 6 km^3. We assume that the original volume of sediment at the time of deposition was similar to the currently preserved volume, as our model calls for limited scarp retreat. At a typical sediment/water volume ratio of 3%, as used by *Jerolmack et al.* (2004) for sandy sediment, this translates to a formative water volume of 200 km^3. As the basin below the -1400 m contour is only 24 km^3, this requires the basin to be filled more than 8 times in order to deliver the required volume of sediment. This requires at least 7 basin volumes of water to be lost in the process of forming the delta (the lake can be filled at the end of deposition, accounting for one basin volume), either through evaporation or infiltration. For a mean lake area of 240 km^2 and a loss rate L (m/yr) over that area, we can estimate the time required to remove this water from the basin at 700/L years. The value of L is unconstrained given the limited knowledge of the depositional environment. However, for typical terrestrial lacustrine loss rates of 1–10 m/yr (*Tyler et al.*, 1997; *Irwin et al.*, 2005), we estimate a minimum formation time of several hundred years. This increases the formation timescale slightly from the previous estimate of *Jerolmack et al.* (2004), who used a sediment transport model to estimate a minimum formation time for the delta of 50 years.

2.6 Summary

Stratigraphic studies of depositional structures on Mars is finally possible with high-resolution stereo topography. The geologic history of the Eberswalde fan is accessible through its unique form. Stereo-derived topographic data was used to examine the structure of individual layers within the outcrop at the distal end of the deposit. This analysis revealed that the exposed layers are not consistent with steep foreset beds found in terrestrial coarse-grained deltas. Volume calculations of the basin

within Eberswalde crater revealed that the basin should fill rapidly under estimated flow rates. There are inconsistencies associated with the standard formation scenarios of both alluvial fans and prograding deltas. A potential solution to the observed characteristics is proposed, in the form of a rapidly aggrading delta. The exposed layers were deposited as topset beds, as the base-level rose over a timescale of years. Modest erosional retreat of the delta front would have erased the volumetrically smaller foresets. This scenario implies the Eberswalde deposits formed not in a sustained long-lived lake, but more likely within a small number of shorter lacustrine episodes marked by a constantly rising base-level, which were never able to reach equilibrium conditions.

Acknowledgements

We thank John Grotzinger and Kerry Sieh for illuminating discussions, and Anton Ivanov for sharing software he developed. This work was supported by NASA's Mars Data Analysis Program grants # NAG5-13326 and NAG5-13232.

Chapter 3

Stratigraphy of the Inner Basin of the Columbia Hills from the Spirit Mars Exploration Rover

3.1 Home Plate

Originally published in:
Lewis, K. W., O. Aharonson, J. P. Grotzinger, S. W. Squyres, J. F. Bell III, L. S. Crumpler, and M. E. Schmidt (2008b), Structure and stratigraphy of Home Plate from the Spirit Mars Exploration Rover, *J. Geophys. Res.*, *113*, E12S36, doi:10.1029/2007JE003025

Abstract

Home Plate is a layered plateau observed by the Mars Exploration Rover Spirit in the Columbia Hills of Gusev Crater. The structure is roughly 80 meters in diameter, and the raised margin exposes a stratigraphic section roughly 1.5 meters in thickness. Previous work has proposed a pyroclastic surge, possibly followed by aeolian reworking of the ash, for the depositional origin for these beds. We have performed a quantitative analysis of the structure, stratigraphy and sedimentology at this location. Our results are consistent with an explosive volcaniclastic origin for the layered sediments. Analysis of bedding orientations over half of the circumference of Home Plate reveals a radially inward dipping structure, consistent with deposition in the volcanic vent, or topographic draping of a preexisting depression. Detailed observations of the sedimentology show that grain sorting varies significantly between outcrops on the east and west sides. Observations on the western side show a well-sorted population of sand-sized grains which comprise the bedrock, while the eastern

margin shows a wider range of grain sizes, including some coarse granules. These observations are consistent with primary deposition by a pyroclastic surge. However, aeolian reworking of the upper stratigraphic unit is not ruled out. Identification of explosive volcanic products on Mars may implicate magma interaction with subsurface hydrologic reservoirs in the past.

3.1.1 Introduction

The Mars Exploration Rover Spirit saw limited exposures of bedrock, and very few layered rocks for the first several hundred sols of its mission (*Squyres et al.*, 2004a). This underscored the significance of the first images at close range of a formation named Home Plate, which revealed extensive outcrops of clearly stratified bedrock. Home Plate (located at 14.64° S, 175.53° E) was first identified from Mars Orbiter Camera (MOC) images as a target of interest based on its light-toned appearance compared to the surrounding soil and rocks of the Columbia Hills, where Spirit has spent the latter part of her mission. From orbital images, Home Plate stands out as the largest expanse of lighter-toned material in the Inner Basin of the Columbia Hills. Among sites visited by Spirit, Home Plate is unique, although a few smaller bright features in the Columbia Hills seen from orbit may be analogous. From rover images, Home Plate is a subcircular plateau, up to a few meters high in places, composed of stratified sedimentary rocks (*Squyres et al.*, 2007). The sedimentary sequence here exhibits several units, each characterized by distinct morphologies. Several possible interpretations were consistent with initial observations, including fluvial, aeolian, and volcaniclastic deposits. Detailed observations were conducted to help address these competing possibilities, all of which can exhibit similar morphologies and can be difficult to distinguish even on Earth. Each possibility, however, would have distinct implications for the local geologic history. The origin of this enigmatic deposit is addressed here using quantitative structural and morphological techniques, providing complementary information to the chemical and mineralogical analysis suite of the MER Athena payload. Stereo images from both the engineering and science cameras are used to assess the internal structure of the bedding exposed at Home Plate in a quantitative manner. In combination with sedimentological and stratigraphic observations, these data constrain the potential hypotheses

regarding the origin of this unique landform, ultimately determined to be volcaniclastic in origin. Hydrovolcanic features and pyroclastic deposits have been identified elsewhere on Mars based on orbital data (*Hynek and Phillips*, 2003; *Wray et al.*, 2008; *Jaeger et al.*, 2007), and modeling has been carried out to understand the formation of such deposits (*Wilson and Mouginis-Mark*, 2003; *Wilson and Head*, 2004, 2007). Home Plate offers the first ground truth example for refining and testing these predictions *in situ*. While the origin of Home Plate has implications for the geologic history of this location, particularly regarding the role of localized, explosive volcanism within Gusev crater, the observations and tools presented here may also aid in the interpretation of similar deposits elsewhere on the planet. Specifically, a technique for robust plane fitting from rover stereo images is described here, and may be applicable to future remote geological investigations.

3.1.2 Regional Setting

Spirit landed on January 4th, 2004 in Gusev crater, a 150 km diameter impact crater in the southern highlands of Mars. This landing site was selected primarily because of its association with Ma'adim Vallis, the main trunk of a large valley network that breaches the southern rim of the crater. This association suggests the possibility of a standing body of water at some time in the Martian past (*Grin and Cabrol*, 1997). In addition to fluvial landforms, a notable feature of the regional geology is Apollinaris Patera, a large volcano 250 km to the north, indicating volcanism also had a significant presence in this region of Mars (*Robinson et al.*, 1993; *Martınez-Alonso et al.*, 2005). Indeed, upon Spirit's landing, the plains around the rover were found to be uniformly basaltic in composition (*McSween et al.*, 2004; *Arvidson et al.*, 2006; *Morris et al.*, 2006). After thoroughly characterizing the basaltic rocks of the Gusev plains, Spirit undertook a traverse to the Columbia Hills, in search of what appeared from orbit to be older geologic units and new lithologies. This small area of higher terrain is isolated among the otherwise flat topography of the plains. In orbital images, the basaltic plains clearly embay the older hills (*Crumpler et al.*, 2005). Although the process that uplifted or emplaced the hills remains unknown, they may be remnants of the intersection of multiple crater rims, or remnants of the Gusev crater central peak (*McCoy et al.*, 2008). Within

this new terrain, Spirit has found new classes of rocks, evidence of aqueous alteration, and the first sedimentary rocks of the mission (*Squyres et al.*, 2006).

After climbing Husband Hill, Spirit descended roughly 70 m into the Inner Basin of the Columbia Hills (Figure 3.1). In this area, Home Plate is one of the more prominent geologic structures, and appears to contain the largest expanses of bedrock. Several topographic ridges surround Home Plate, and may be genetically related. These include Mitcheltree Ridge to the east, and Low Ridge to the south. These ridges contain smaller outcrops of layered rock, and are capped by large, and often vesicular basaltic rocks. The stratigraphic relationship of these ridges to Home Plate remains unclear.

3.1.3 Home Plate Observational Campaign

Due to the approaching winter and declining power levels, Spirit conducted an initial survey of Home Plate over the course of roughly 26 sols. Spirit first approached Home Plate on sol 748, at the northwest corner of the structure, after descending from Husband Hill. The outcrop at this location is the thickest and most diverse stratigraphic section observed at Home Plate to date. At this location, Spirit analyzed the target Barnhill on the outcrop, and also a float rock, Posey. After this initial survey, Spirit drove to the top of Home Plate to gain a better vantage point for imaging the entire structure. In addition, Spirit carried out two analyses using its Instrument Deployment Device (IDD), on the targets Stars and Crawfords. Following the *in situ* campaign, Spirit undertook a clockwise traverse, imaging prominent outcrops between drives. This traverse continued through sol 774, when Spirit left Home Plate to find a favorable location for winter operations. Spirit's departure at the Eastern side of the structure completed a survey of roughly one-third of the circumference of Home Plate.

After a mobility hiatus during the Martian winter, Spirit returned to Home Plate, and conducted an extensive campaign along the southeastern margin of the structure. This included both close range remote sensing along the outcrop, as well as a set of nine *in situ* observations of the cross-bedded rocks on the eastern margin. Together, these two analysis campaigns cover roughly half of the Home

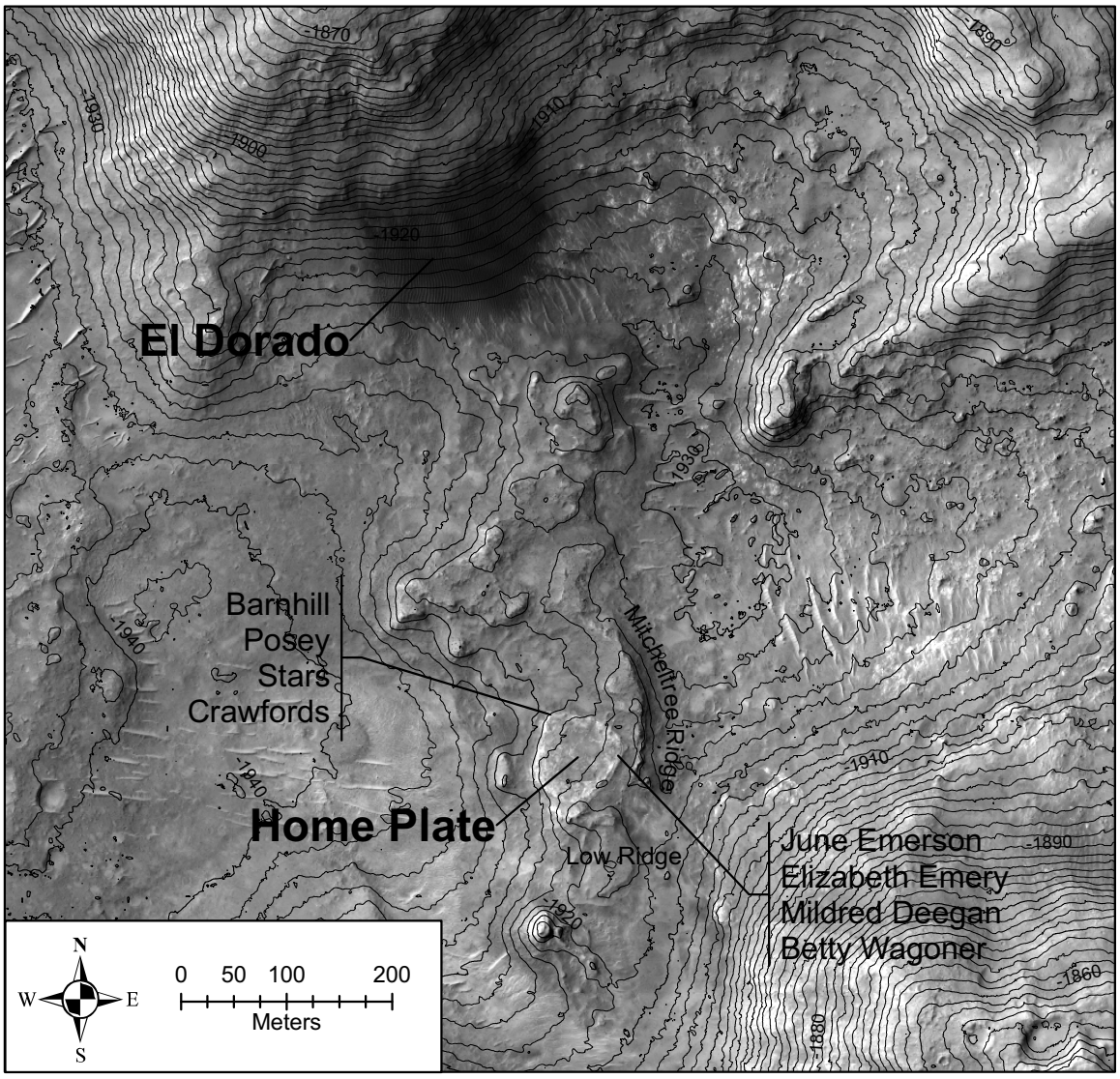

Figure 3.1: Map of the Inner Basin of the Columbia Hills, where Spirit has been conducting operations for the latter half of her mission. Home Plate stands out as a sub-circular light toned platform roughly 80 m in diameter. Topographic measurements indicate a dip of 3°–4°to the northwest for the surface of Home Plate. Several small ridges are situated immediately around Home Plate, including Mitcheltree Ridge to the east, and Low Ridge to the south. The dark feature near the top of the image is a modern aeolian dune field known as El Dorado. Contours at 2 m intervals are derived from stereogrammetry using HiRISE images PSP_001777_1650 and PSP_001513_1655. (Image credit: NASA/JPL/University of Arizona)

Plate margin, providing an extensive dataset for interpreting its origin and context within the Inner Basin.

3.1.4 Stratigraphy

Bedrock outcrops along the margin of Home Plate reveal a diverse stratigraphic sequence. Several distinct morphologies have been observed, which can be delineated into distinct geologic units. Chemically and mineralogically, these units are very similar, and comprise the Barnhill rock class. Further, all of the units at Home Plate have similar major element compositions to nearby vesicular basaltic rocks of the Irvine rock class (*Schmidt et al.*, 2008). The two basic units identified at Home Plate include a planar-bedded to massive lower unit, and a cross-bedded upper unit. An intermediate layer between these serves as a useful marker bed for correlating outcrops. No exposed contact has been observed at the base of this section, and the nature of the underlying material is unknown.

3.1.4.1 Lower Unit

The northwest margin of Home Plate contains the most complete section observed to date, including the best exposures of the lower stratigraphic unit. The lowest unit in the observed depositional sequence is characterized by thick beds which are planar and parallel over several meters (Figure 3.2, lower inset). In Microscopic Imager (MI) images of this unit, a knobby texture is apparent, though it is difficult to tell whether these are original clasts or diagenetic textures. In the only clear exposure of the lower unit on the northwest corner, the bedding has been eroded back into nearly planar outcrops. There is some variation in physical strength between beds, as some tend to form ledges, while others are recessed. This pattern indicates variable depositional conditions throughout the lower unit. While this characteristic does not discriminate unambiguously between depositional processes, it is consistent with a pyroclastic deposit, which can show rapid fluctuations in grain size, sorting, and induration between beds (*Crowe and Fisher*, 1973).

Within the lower unit, an apparent bomb sag has been identified from Pancam images (see lower inset in Figure 3.2) (*Squyres et al.*, 2007). On Earth, bomb sags are typically associated

with volcaniclastic deposits, where outsized clasts thrown out of an explosive vent are emplaced ballistically into an otherwise fine-grained ash deposit. The high-energy impact causes disruption and deformation of the underlying layers (*Fisher and Schmincke*, 1984). In this area, the strata of the lower unit appear to curve beneath a clast several centimeters wide, which is embedded within the outcrop. Topographic measurements were made to evaluate whether the apparent curvature in the bed associated with this clast is truly a topographic depression, as opposed to an effect of the outcrop and viewing geometries. Stereo data acquired at close range to the bomb sag indicate that the layer does deflect roughly 2 cm downward from an otherwise linear exposure in the vicinity of the bomb. This observation supports the case for a bomb sag in the lower unit of Home Plate, and an explosive origin for the clasts which comprise it.

At the top of the lower unit, a transition to a massive facies occurs, as shown in the stratigraphic section (Figure 3.2, middle inset). The change from planar-stratified to massive facies is gradual, with the prominent bedding at the bottom of the unit becoming less distinct, and eventually disappearing. It was not possible to extract any structural information from this part of the unit, although it appears to be conformable with the planar-bedded section beneath it. MI images of this massive section show a texture similar to the planar beds, with nodular textures, but no clearly identifiable grains. This part of the lower unit is roughly 10 cm thick, as shown in the stratigraphic column in Figure 3.2. As indicated in this figure, the lower unit has not been clearly identified on the eastern side of Home Plate. It is likely obscured by modern aeolian cover, but may simply not have been preserved (or ever deposited) in the section here. A correlation may exist with other rocks exposed on the east side between Home Plate and Mitcheltree Ridge, although poor exposures have prevented a conclusive determination.

3.1.4.2 Upper Unit

The upper unit of Home Plate accounts for the majority of the vertical section, roughly 90 cm out of 1.3 m on the northwestern corner. This unit is thin bedded, with characteristic low-angle cross-bedding occurring throughout the section and at least one location with high-angle cross-bedding

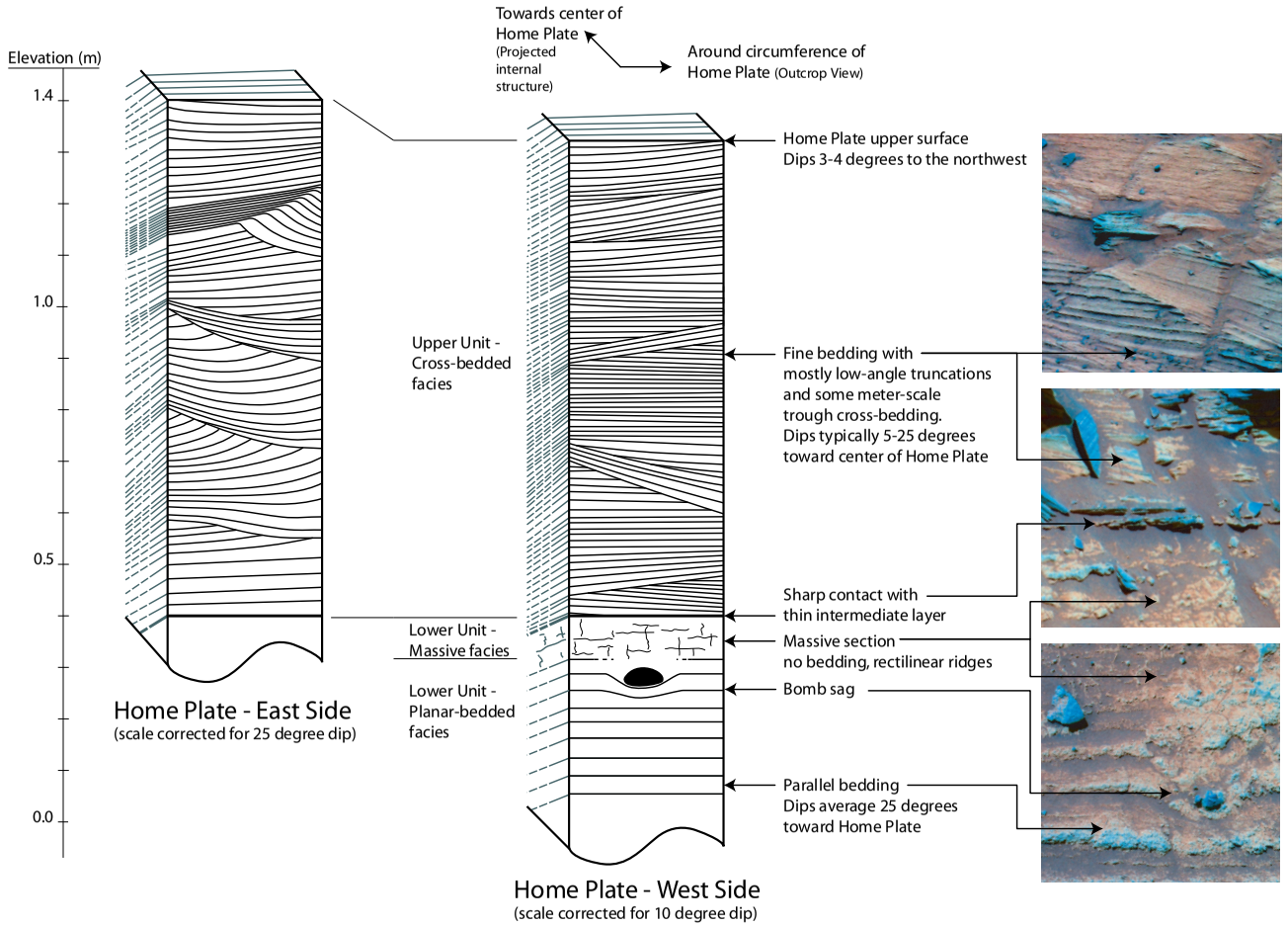

Figure 3.2: Stratigraphic column of Home Plate outcrops. The primary division is between the lower unit, where planar-bedded and massive facies are observed, and the upper unit, dominated by cross-stratification. The presence of a putative bomb sag in the lower unit points to an explosive volcanic origin of the Home Plate. On the east side of Home Plate, the lower unit has not been identified, although a correlation is indicated between a prominent layer seen at the base of the upper unit at both locations. After correcting for the structural dip on both the west and east sides of Home Plate, the stratigraphic thickness of the upper unit is calculated to be within 10 cm between outcrops. The side panel of each column indicates the projected internal structure, which dips toward the center of Home Plate at each location visited by Spirit. Examples of each unit are shown at right in a Pancam false color stretch using filters L2,5,7 (753, 535, and 432 nm respectively). Image numbers: 2P228456914EFFAS6MP2440L2M1 (top); 2P192944022EFFAO55P2275L2M1 (middle); 2P193032914EFFAO55P2276L2M1 (bottom).

on the eastern edge (Figure 3.2, upper inset). The upper unit exhibits fine stratification, with individual strata typically a few millimeters in thickness. Two competing hypotheses have been proposed for the upper unit of Home Plate (*Squyres et al.*, 2007). In the first interpretation, the upper unit is conformable with the lower unit, deposited in a later stage of the same pyroclastic surge. Cross-stratification, often referred to as a "sandwave" facies in the case of volcaniclastic deposits, is a common feature of terrestrial surge beds (*Wohletz*, 1998). Alternatively, the upper unit may represent material which has been reworked by aeolian processing from the same material which comprises the lower unit, being lithified at a later time. Thus, a central question for understanding the origin of Home Plate is discerning the depositional environment of the upper unit.

Two facies are prevalent within the upper unit of Home Plate. From the northwestern to the southern corners of Home Plate, images have been acquired of nearly the entire margin, and in some places repeatedly. Thus, the image datasets are highly representative of the actual outcrops at Home Plate. At most locations on the northern and southern perimeter, beds are planar or low-angle stratified. Truncation surfaces are typically inclined only a few degrees from bedding planes, and occur throughout the section. This bedding style is not uniquely diagnostic of a particular depositional mode, and is consistent with either surge deposition (*Fisher and Schmincke*, 1984) or an aeolian sand sheet facies similar to that described at Meridiani Planum by *Grotzinger et al.* (2005).

On the eastern margin of Home Plate, large-scale trough cross-bedding dominates the section (Figure 3.3). Concave upward erosion surfaces are common and extend over meter-scale wavelengths. Bed sets within this facies contain strata that parallel or asymptotically approach erosional lower surfaces. Exposed cross-bed sets are typically a few meters in horizontal extent, and tens of centimeters in thickness. It is well-established that trough cross-bedding is formed by migration of sinuous crested bedforms (*Rubin*, 1987). However, the link from stratigraphy to specific flow dynamics is less certain. The cross-bed sets on the eastern margin of Home Plate show a consistent orientation between bounding surfaces and internal stratification throughout the section, as shown in Figure 3.3. For a cross section nearly perpendicular to the flow direction, trough cross-bedding should show a

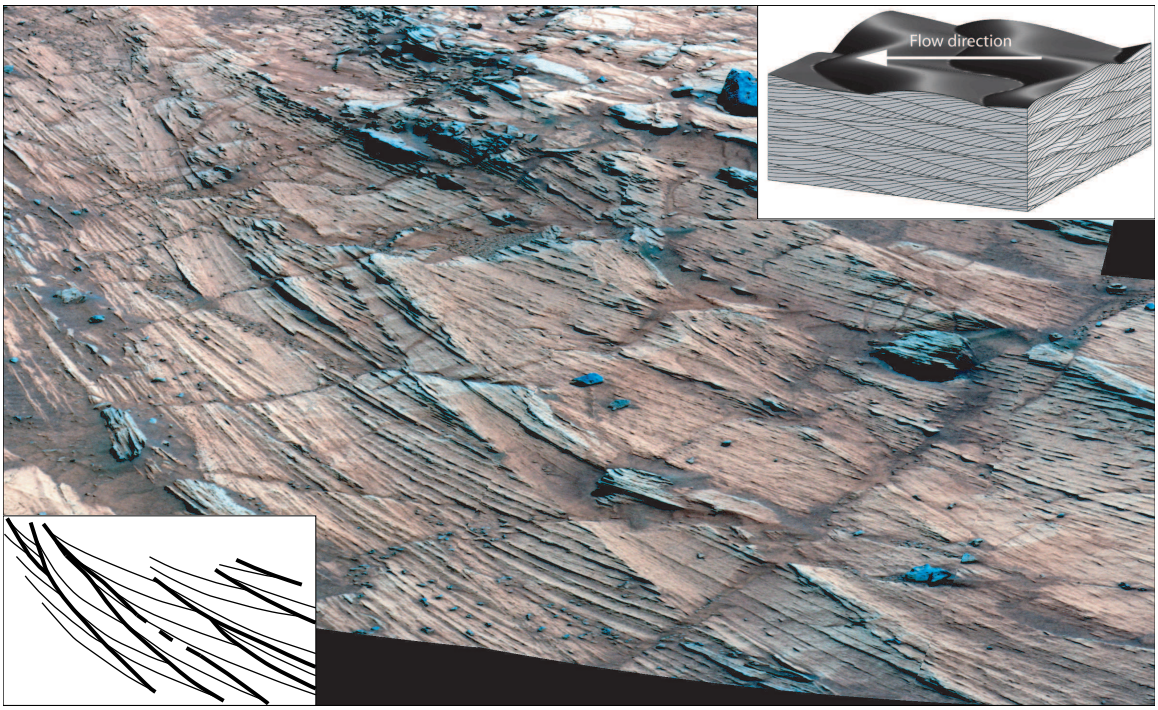

Figure 3.3: One example of high angle cross-bedding observed at Home Plate, from sol 1150. An interpreted sketch is shown the lower inset, with erosional boundaries between cross-bed sets marked as thick lines with representative cross-strata shown as thin lines. At this location, cross-strata show a consistent orientation with respect to bounding surfaces, and bounding surfaces occasionally intersect at low angles. This suggests a uniform migration direction, which was oblique to the outcrop. The upper inset shows one possible bedform reconstruction for this outcrop. The horizontal distance across the lower part of the image is approximately 2 meters. The mosaic is a false color stretch, as in Figure 3.2. (Mosaic credit: NASA/JPL/Cornell University)

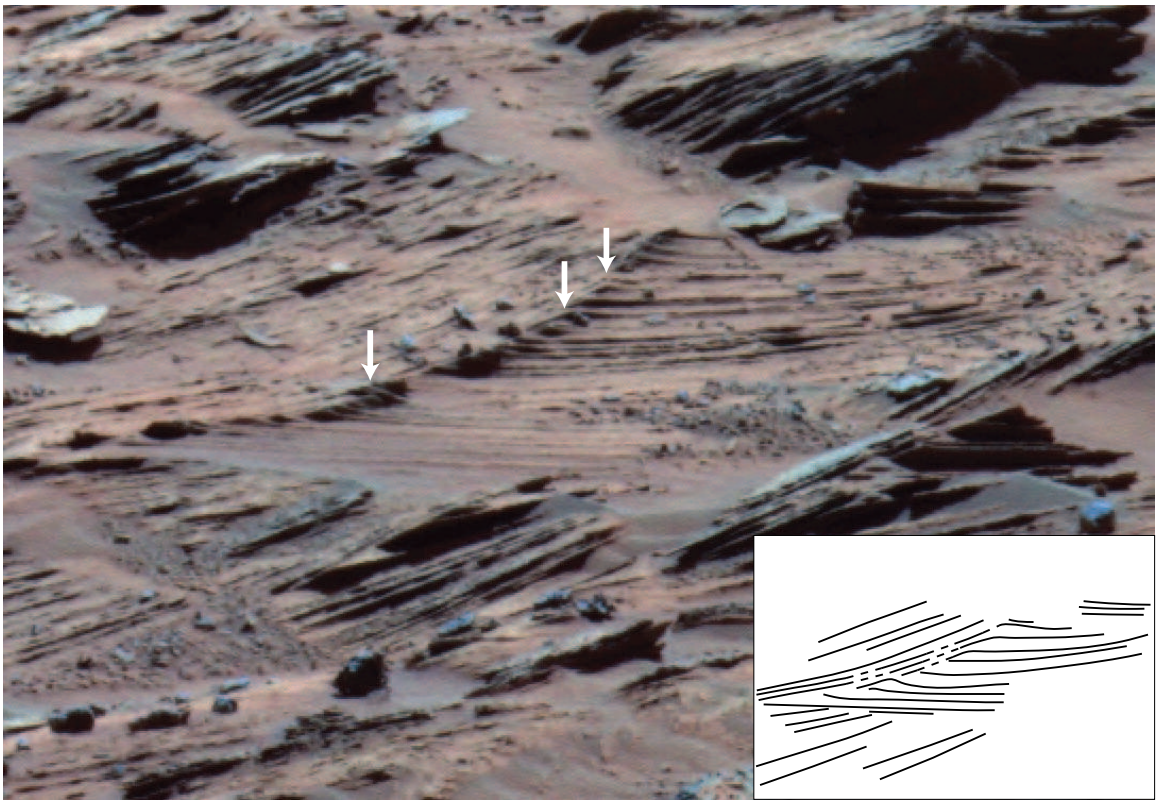

Figure 3.4: High angle cross-bedding exposed on the eastern side of Home Plate. This example shows evidence for the preservation of stoss-side laminae along with the crest of the bedform. Locations where preservation of the crest is apparent are shown with white arrows. The inset shows a sketch of the interpreted strata. Preservation of the crest of such a bedform implies rapid deposition relative to lateral migration. The outcrop here is north-south trending, on the eastern margin of Home Plate. The image is approximately 1 m across, and is a false color stretch as in Figure 3.2, of sol 774 image 2P195076279EFFAPDSP2381L7M1.

variety of orientations with respect to erosion surfaces. For this reason, the flow direction is interpreted to be oblique to the outcrop orientation at this location. Further, the consistent orientation of the cross-beds implies a uniform migration direction of the bedforms. This observation is consistent either with a pyroclastic surge, or aeolian dunes that generally migrated in one direction. One possible bedform reconstruction is shown in the upper inset of Figure 3.3, created using software developed by *Rubin and Carter* (2006). In this inset, a sinuous-crested bedform is shown migrating uniformly in a direction oblique to the exposed section. This is a simple formation hypothesis for the outcrops seen at Home Plate; more complex geometries, particularly ones involving multiple superimposed bedforms, may also be consistent with observed cross-bedding geometries.

In one location on the east side of Home Plate a unique high-angle bedform is preserved, as

shown in Figure 3.4. The outcrop here is interpreted to expose a cross section nearly parallel to the flow direction, which was likely left to right in this image. Interpreted lee side strata are inclined at a steep angle to the prevailing bedding orientation. In this example, the crest of the bedform and some of the windward side appears to have been preserved. Stoss preservation indicates that the bedform was climbing at a supercritical angle, or slightly steeper than the stoss side laminae. Climb angles near or above this critical angle occur when the deposition rate is high relative to the lateral migration of the bedform. For terrestrial aeolian deposits, evidence of supercritical climb is rare in the geologic record (*Kocurek*, 1991; *Rubin and Hunter*, 1982). Further, the continuity of the laminae between the stoss and lee sides of the bedform in Figure 3.4 is unusual for a simple aeolian bedform, which tend to be dominated by traction on the windward side and both fallout from suspension and avalanching on the lee side. In cases where aeolian dune crests are preserved, the processes would produce different stratification patterns and discontinuous laminations between the stoss and lee sides (*Ahlbrandt and Fryberger*, 1982). In contrast, stoss depositional forms are commonly documented in pyroclastic surge deposits (*Crowe and Fisher*, 1973; *Cole*, 1991). In this case, laminae are often continuous over the crest of the dune (e.g., Plate 3 of *Fisher and Waters*, 1970). Both the presence of cohesive sediment and rapid fallout from suspension over the whole bedform can allow preservation of the crest in a surge deposit (*Crowe and Fisher*, 1973). The observation of a supercritically climbing bedform favors the pyroclastic interpretation for the upper unit, although it is the only example seen thus far at Home Plate.

Ideally, details of the cross-bedding observed in the upper unit of Home Plate could provide clues as to the depositional process that formed it. Cross-bedded sediments are most commonly deposited by aeolian or fluvial processes on Earth. However, volcanic surge deposits can also show complex cross-stratification, and the discrimination between primary surge deposits and those reworked by aeolian processing is difficult even in terrestrial settings (*Smith and Katzman*, 1991). Very little chemical or morphological evidence has been found for fluvial action in the Columbia Hills (*Squyres et al.*, 2007). Further, as discussed in section 3.1.5, a large fraction of the sediment comprising the upper unit is unresolvable by the MI, implying grain sizes less than 100 µm. As shown in Figure

17 of *Grotzinger et al.* (2005), dunes are not predicted to form in subaqueous flows on Mars for grain sizes less than ∼200 µm. However, the aeolian and surge interpretations are both consistent with many of the observed characteristics. In particular, large-scale trough cross-bedding is well documented on Earth in both aeolian deposits (*Rubin*, 1987; *Ahlbrandt and Fryberger*, 1982) and volcaniclastic surges (*Wohletz*, 1998). The cross-bedding seen at Home Plate is typically at the decimeter to meter scale. In most cases, bedforms are truncated, indicating larger original heights. No bedforms have been observed at centimeter-scale wavelengths.

3.1.4.3 Intermediate Layer

At the northwestern corner of Home Plate, a thin, erosion-resistant bed was observed between the upper and lower units (Figure 3.2, center of middle inset). This bed typically appears as a doublet of two prominent strata, roughly 2 cm thick in total. The physical strength of this layer, in combination with its position between two morphologically distinct units, makes it a useful marker bed for correlating outcrops.

The intermediate layer cannot be traced continuously around Home Plate, disappearing particularly on the northeastern margin. However, a similar unit is observed on the southeastern edge of Home Plate. At several locations, an erosion-resistant "fin" appears close to the bottom of upper, cross-bedded unit. Further, the bed often appears as a doublet, of similar thickness to that observed on the other side of Home Plate. The location of this layer at the bottom of the exposed section is also consistent with the disappearance of the lower unit on the southeast margin. Thus, the combined similarity in thickness, stratigraphic position, and morphology suggest that these strata are correlative over 180° of the circumference of Home Plate. The observation of this intermediate layer on both the northwest and southeast sides of Home Plate also requires deposition by a process which was uniform over at least tens of meters.

3.1.4.4 Home Plate Upper Surface

Observations of the top of Home Plate, which Spirit drove onto at the northeastern and western margins, show a heavily fractured, dust-covered surface. Several subcircular dust-filled depressions are likely remnants of small impact craters, indicating an ancient surface. Where upper unit rocks are exposed, they have been rotated and displaced, making their stratigraphic interpretation difficult. While Spirit has not driven into the center of Home Plate, some exposures of bedrock are continuous and appear to be largely intact from rover and orbital images. This indicates that the modern surface is primarily a product of bedrock erosion, rather than infill by aeolian material. In addition, there appear to be localized areas where dark, vesicular basaltic rocks are scattered around the surface. The stratigraphic position of these rocks relative to the Home Plate sequence is unknown, although geochemical results indicate a genetic relationship (*Schmidt et al.*, 2008).

Aeolian erosion has left a smooth upper surface to the Home Plate structure, although a small raised rim exists in some locations, particularly on the southern margin. The topography of the upper surface of Home Plate can be quantified using orbital stereo images. We have used High Resolution Imaging Science Experiment (HiRISE) images (image numbers PSP_001777_1650 and PSP_001513_1655) to derive a digital elevation model (DEM) for the Columbia Hills via the method of *Kirk et al.* (2008). From this dataset, Home Plate can be adequately approximated by a plane, which dips 3°–4°to the northwest (Figure 3.1). While the upper surface of Home Plate has clearly undergone some degree of erosion, the magnitude and azimuth are similar to the surrounding gradient of the Inner Basin, as measured from the same dataset. This long wavelength tilt of the upper surface of Home Plate may reflect draping of the preexisting topographic slope.

3.1.5 Sedimentology

Spirit made observations of several targets at two locations around the perimeter of Home Plate with the Microscopic Imager. Three of these targets (Posey, Crawfords, and Stars) were rocks from the upper cross-bedded unit, on the western side. Stars and Crawfords were both on top of Home Plate, indicating an origin in the uppermost part of the section, although the rocks in this area appear to

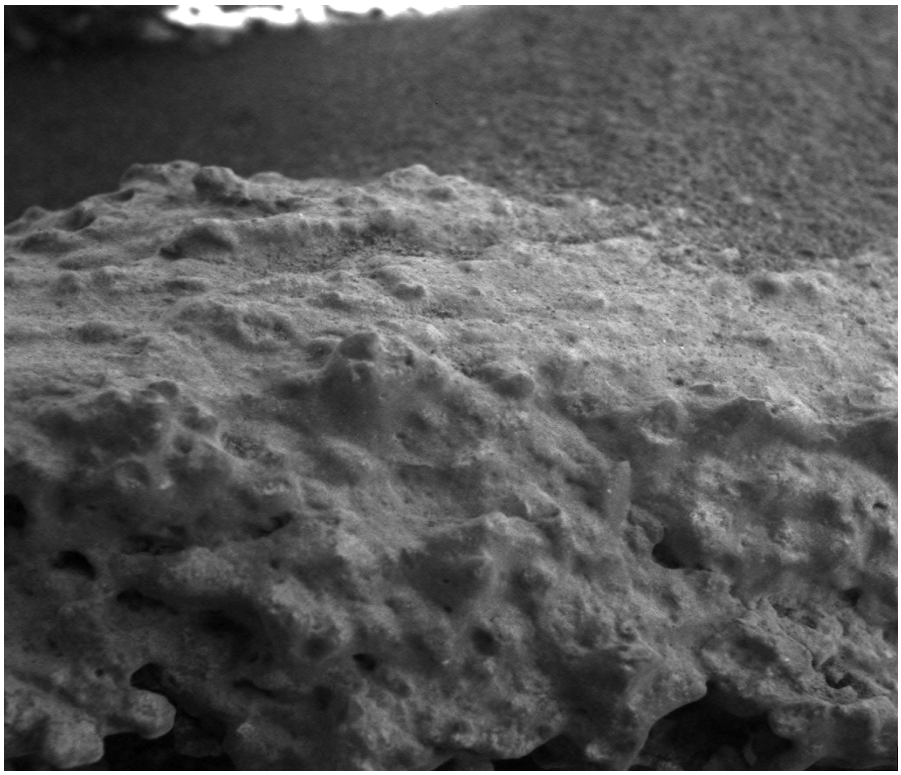

Figure 3.5: Unbrushed surface of Barnhill, a target within the lower unit of Home Plate, taken on sol 750. The view is 3 cm across. Image 2M192958525FFLAO55P2977M2M1.

have been rotated and shifted from their original positions. Posey, on the other hand, was clearly out of place, located to the side of Home Plate. Although its exact position in the stratigraphic column cannot be determined, its fine-scale stratification clearly correlates with the character of the upper unit of Home Plate. All of these images were taken roughly parallel to bedding planes. A fourth target on the west side, Barnhill, was imaged within the lower unit, on sols 747 and 750 (Figure 3.5). This target was of in-place bedrock at the northwest corner of Home Plate, so its stratigraphic position is well-established. Finally, a set of seven observations were made on the east side of Home Plate, with five in the upper unit, and two on the intermediate fin layer. All of the east side targets were in place in the outcrop, and most were perpendicular to bedding planes, exposing a sequence of strata.

Figure 3.5 shows an MI image of the lower unit target Barnhill. While the lower unit of Home Plate is stratified at centimeter scales, it is massive at smaller scales. Further, there is little evidence of individual clasts within this rock. The lack of a clastic texture suggests either that the sediment

size is largely below the resolution of the MI (less than 100 µm), or that diagenetic or weathering processes have obscured the original clastic texture. The latter interpretation is supported by the knobby texture seen in some lower unit rocks, as shown in Figure 3.5. When they can be measured, these roughly equant knobs are of a coarse to very-coarse sand size (roughly 1 mm in diameter, or between 1 and -1 on the ϕ scale).

In contrast to the lower unit, MI images of upper unit rocks show abundant dark clasts typically hundreds of µm in diameter, and up to nearly 3 mm for the largest example (Figure 3.6d). In some cases, the rocks appear to be clast supported, as in the case of Crawfords, on the northwestern side of Home Plate (Figure 3.6a). However, particularly on the eastern side of Home Plate, a significant volumetric fraction of the rocks appears to be composed of material finer than the resolution of the MI ($\sim$100 µm, (*Herkenhoff et al.*, 2004)), as seen in Figure 3.6c and 3.6d. In the case of a mature aeolian deposit, material below this threshold is often removed by suspension, leaving a well sorted framework of coarser particles which move by saltation. This attribute is observed for modern aeolian deposits imaged by Spirit, one example of which is shown in Figure 3.6b. This image was taken at the 170 m wide sand sheet known as El Dorado to the north of Home Plate (Figure 3.1). At this location, the apparent lack of finer-grained material was also indicated by a lack of sediment cohesion within a trench dug by the rover (*Sullivan et al.*, 2006). In contrast, the poorly sorted character of many surge deposits on Earth is consistent with a large fine-grained fraction (*Smith and Katzman*, 1991).

The upper unit exhibits several differences in sedimentology between the east and west side of Home Plate. On the west side, grains are highly rounded, appearing to be nearly spherical for the largest, best-resolved grains. In contrast, on the east side of Home Plate, grains are more angular, and occasionally elongated. Grain roundness is an important characteristic for distinguishing between depositional processes. Very round grains typically indicate extensive transport and abrasion prior to deposition. An excellent example is the El Dorado sand sheet, shown in Figure 3.6b. In contrast, juvenile pyroclasts are typically angular, experiencing only minor physical abrasion during transport (*Wohletz*, 1983). While the rock targets on the west side of Home Plate are strikingly

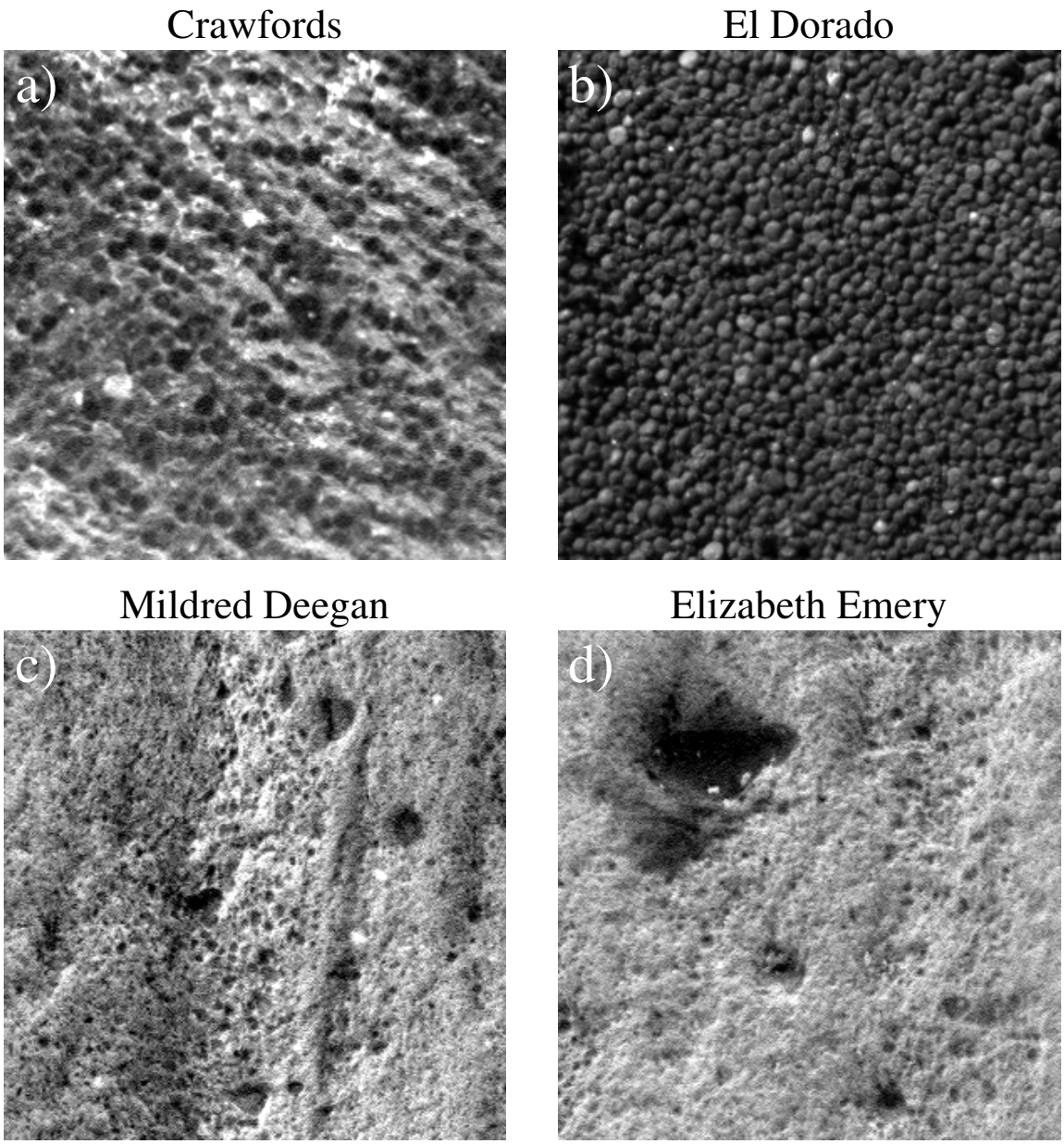

Figure 3.6: MI views of Home Plate upper unit rock targets (Crawfords, Mildred Deegan, and Elizabeth Emery), compared with the modern El Dorado dune field also observed by Spirit. In the rock Crawfords, a consistent population of well rounded and sorted clasts are observed. This population is nearly identical to that observed at El Dorado, both in terms of shape and sorting. However, on the east side of Home Plate, images of the lower two rock targets show a more poorly sorted texture, with several outsized clasts. The largest clast, from Elizabeth Emery, is nearly 3 mm in diameter. Aeolian activity can not transport grains of this size by saltation on Mars (although saltation-induced creep may be possible), giving weight to the primary pyroclastic surge interpretation for the upper unit. Each image is a subframe 1 cm across. Image numbers: 2M194100679EFFAODQP2936M2M1, 2M189317855EFFAL00P2956M2M1, 2M234495019EFFATF3P2936M2M1, 2M234405984EFFATF3P2936M2M1.

similar to modern aeolian deposits in terms of roundness, the east side targets are more consistent with a limited degree of transport and abrasion. Ultimately, these contrasting observations alternately provide support for either a pyroclastic or an aeolian depositional mechanism for the upper unit.

The second important characteristic of the upper unit clasts is their degree of sorting, which again varies between the two sides of Home Plate. To quantify the sorting characteristics, we have measured the diameters of several hundred grains in selected patches of the MI images for each of the upper unit targets. In addition, we performed the analysis on El Dorado, the modern aeolian deposit observed by Spirit earlier in the mission. This was done for comparison in recognition of the fact that aeolian deposits are typically among the most mature sediments found in terrestrial environments (*Prothero and Schwab*, 2004).

Figure 3.7 shows a plot of the sediment size distribution for each of the targets on the west side, along with El Dorado. All of the distributions fall within a very narrow size range from 100 to 500 µm. The mean grain diameters for the three Home Plate rocks range from 216 µm for Posey to 313 µm for Crawfords, while the aeolian El Dorado is intermediate at 288 µm. Further, the width of these distributions, which gives a measure of the sorting, is similar. Standard deviations range from 48 to 65 µm for Home Plate, while El Dorado falls within these bounds, at 56 µm. Based on grain size and sorting alone, the clast population found on the west side of Home Plate is indistinguishable from a modern, texturally mature sand sheet. However, pyroclastic deposits are also capable of transporting sand sized sediment, and physically sorting the sediment to varying degrees (*Wohletz*, 1983). From the observations of the west side alone, the aeolian reworked hypothesis is favored, but a primary volcaniclastic origin cannot be ruled out.

On the east side of Home Plate, very different sorting characteristics are seen. While the distributions from the west side have a fairly narrow peak around the mean diameter, the east side shows a significant tail of much coarser material, and a peak at somewhat finer grain sizes (Figure 3.8a). The mean grain diameters for these rocks are similar to the west side, while the standard deviations are uniformly higher (Figure 3.8b), consistent with the coarse tail of the distributions. The

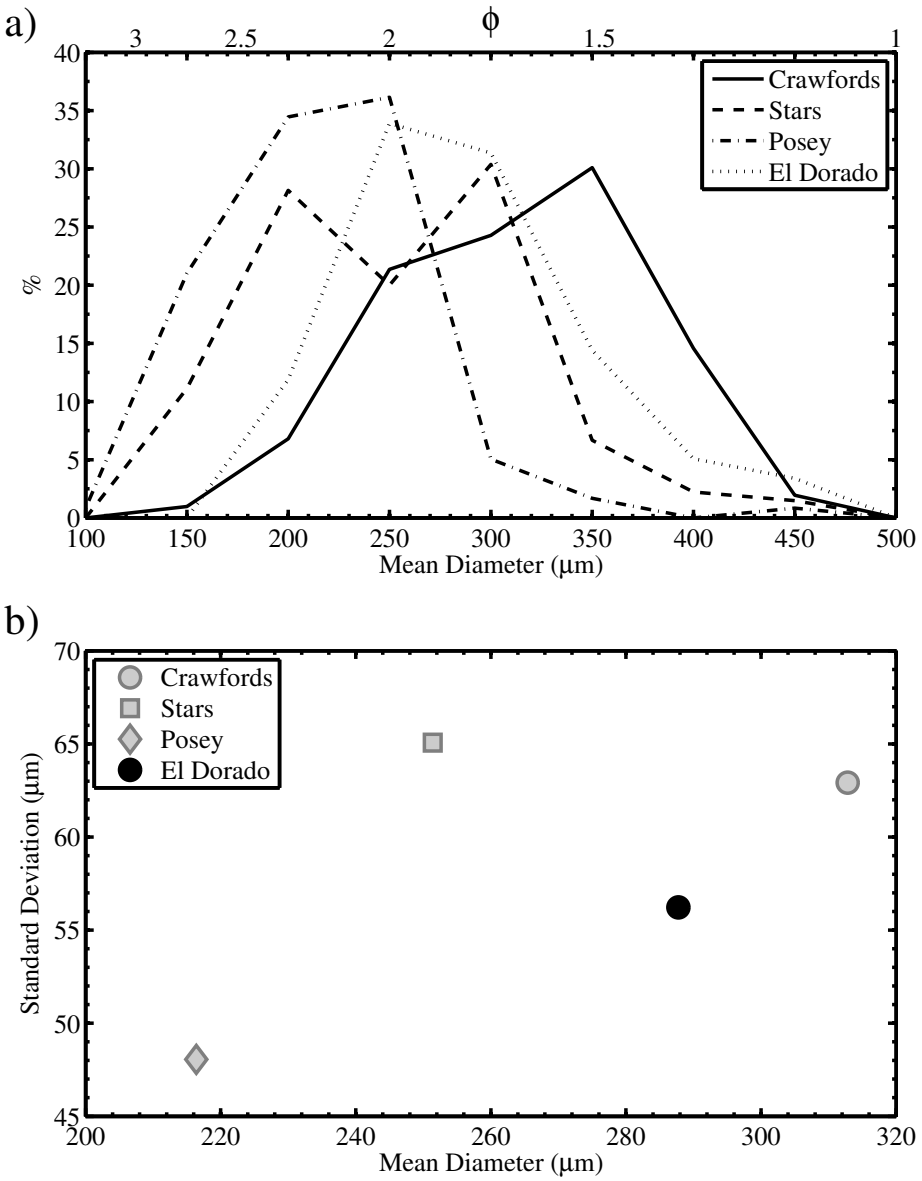

Figure 3.7: a) Grain size distribution for three upper unit rocks from the west side of Home Plate, compared to a modern sand sheet (El Dorado), also observed by Spirit. The four distributions are very similar, demonstrating the high degree of sorting of the sediment which comprises the upper unit. Bin size is 50 µm. b) Mean grain diameter plotted against the standard deviation of the grain size population. Again, Home Plate clasts exhibit textural maturity comparable to modern aeolian sediment.

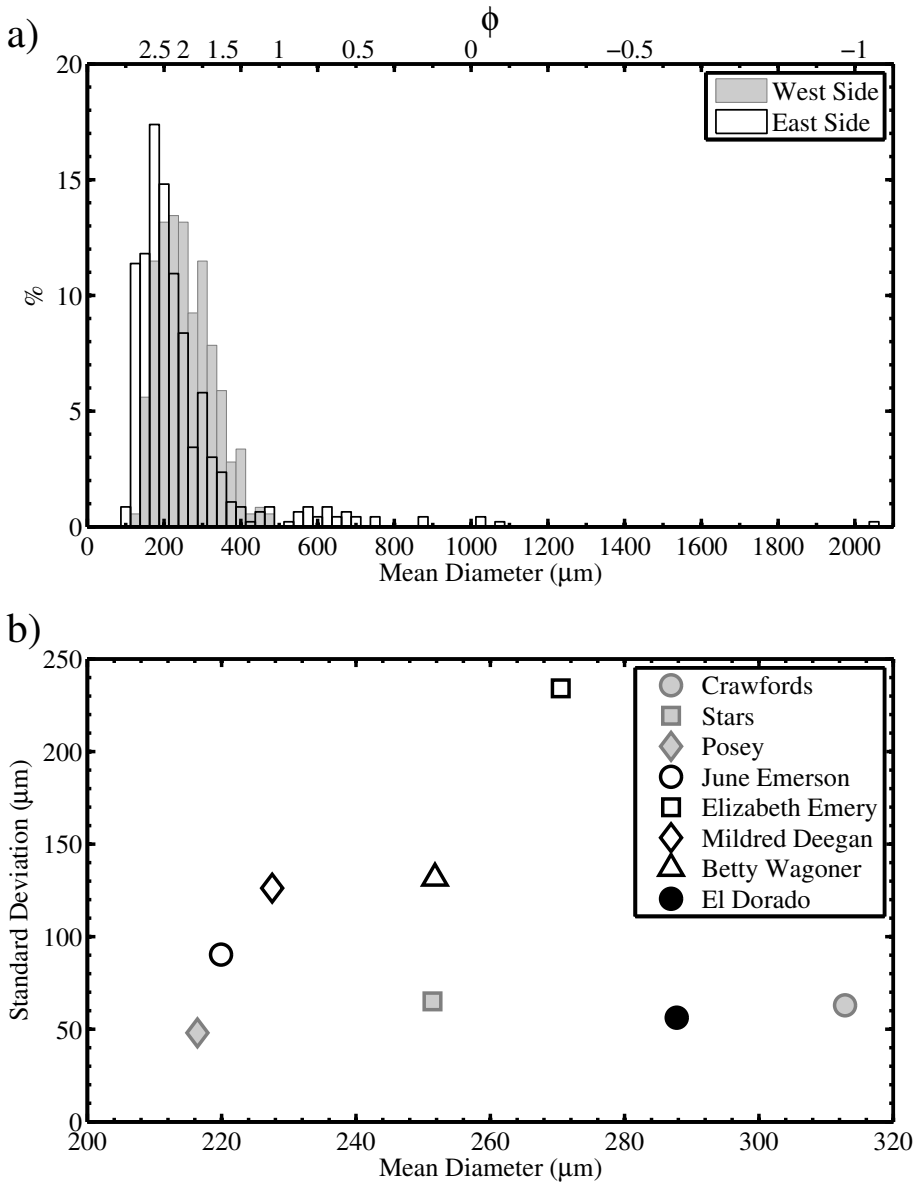

Figure 3.8: a) Grain size distribution for all measured upper unit rocks on the east and west sides of Home Plate. The east side rocks show a long tail of coarser grains out to over 2 mm, and a peak at smaller grain sizes. Bin size is 25 µm. b) Mean grain diameter plotted against the standard deviation of the grain size populations. This plot demonstrates the relatively poorer sorting of the east side rocks (unfilled markers) compared to the west side (gray markers). The modern aeolian deposit El Dorado is also included for comparison.

largest clast found within the cross-bedding on the east side was approximately 1.5 by 2.8 mm in size. This diameter is far larger than any observed at El Dorado, the largest of which are under 0.5 mm. It is, however, consistent with the size range of granules that have been transported by saltation-induced creep in modern eolian deposits on Mars (*Jerolmack et al.*, 2006). These granules can form small, low-relief bedforms known as granule ripples, and have been observed at both rover locations (*Greeley et al.*, 2004). Of course, large clasts are common in pyroclastic surge deposits, and can be emplaced as part of the surge cloud, or ballistically for the largest clasts.

Together, the textural evidence on the east side of Home Plate paints a picture that is the inverse of the situation on the west side: on the east side, a pyroclastic surge origin is favored, but aeolian reworking cannot be ruled out. While observations have illuminated a spatial heterogeneity to the upper unit of Home Plate, it is clear that the cross-bedded outcrops are all part of a single unit, which is expected to have formed via a single process. There is no compelling evidence to suggest multiple processes are required to produce different parts of the upper unit, or that only part of the section may have undergone aeolian reworking.

3.1.6 Structure

3.1.6.1 Method

We have used topographic data derived from stereo images to make precise structural measurements of the stratified materials at Home Plate. The Panoramic Camera (Pancam) is the primary science imaging tool onboard the MER rovers. This pair of cameras is capable of taking stereo images with a 30 cm baseline in both red and blue wavelengths (*Bell III et al.*, 2003). From Pancam image pairs, range and topographic data can be derived out to 100 m or more from the rover (*Squyres et al.*, 2003). To a lesser extent, we have also made use of stereo images from both the Navigation Camera (Navcam), and the Hazard Avoidance Cameras (Hazcams). Image pairs are taken specifically for stereogrammetry, and topographic data is derived via the automated software pipeline maintained by NASA's Multimission Image Processing Lab (MIPL) (*Maki et al.*, 2003; *Alexander et al.*, 2006).

Strata were first traced manually from the original images, and the corresponding topographic

data was subsequently extracted. Layers which could be followed over a significant fraction of the image (typically greater than 75 pixels), and which had a natural three-dimensional topography in the outcrop worked best for this analysis, so efforts were made to select layers which exhibited these qualities.

A best-fit plane is calculated for each layer using linear regression to minimize the residuals in the orthogonal direction. From the best-fit plane, the strike and dip are calculated, along with their corresponding errors. Spirit conducted an extensive though rapid imaging campaign as it circumnavigated the northern and eastern sides of Home Plate. The data used in this analysis are from site 124 position 55; site 125 positions 38, 100, and 218; and site 129 positions 25 and 262 (Figure 3.9). These sites were chosen based on their well-exposed outcrops of intact bedrock, and the suitability of the images for this analysis. Measurements were made for both the planar-bedded lower unit and the cross-bedded upper unit of Home Plate. However, measurements of the upper unit were only taken in areas of low-angle cross-bedding, in order to elicit larger-scale structural information, rather than bedform signatures. Retrieved bedding orientations mostly show dip angles higher than that exhibited by the cross-bedding, affirming that this was the case.

Mathematical criteria are used to select only those layers which provide a well-constrained planar fit. Principal component eigenvalues describe the variance in three orthogonal directions, both within the plane (first and second components), and out of the plane (third component). The first criterion limits the percentage of the variance in the first principal component to less than 99.5%. This prevents layers for which the topography is too linear to adequately constrain the second dimension from being included in further analyses. The second criterion requires the ratio of the variance described by the second principal component to that of the third to be greater than 15, ensuring that the signal which describes the planar fit is significantly larger than the out-of-plane error in the data. These empirical values were found to reliably exclude poorly constrained measurements. The range to the outcrop was less than 5 m at each of the imaging positions, and noise was typically under 1 cm in amplitude.

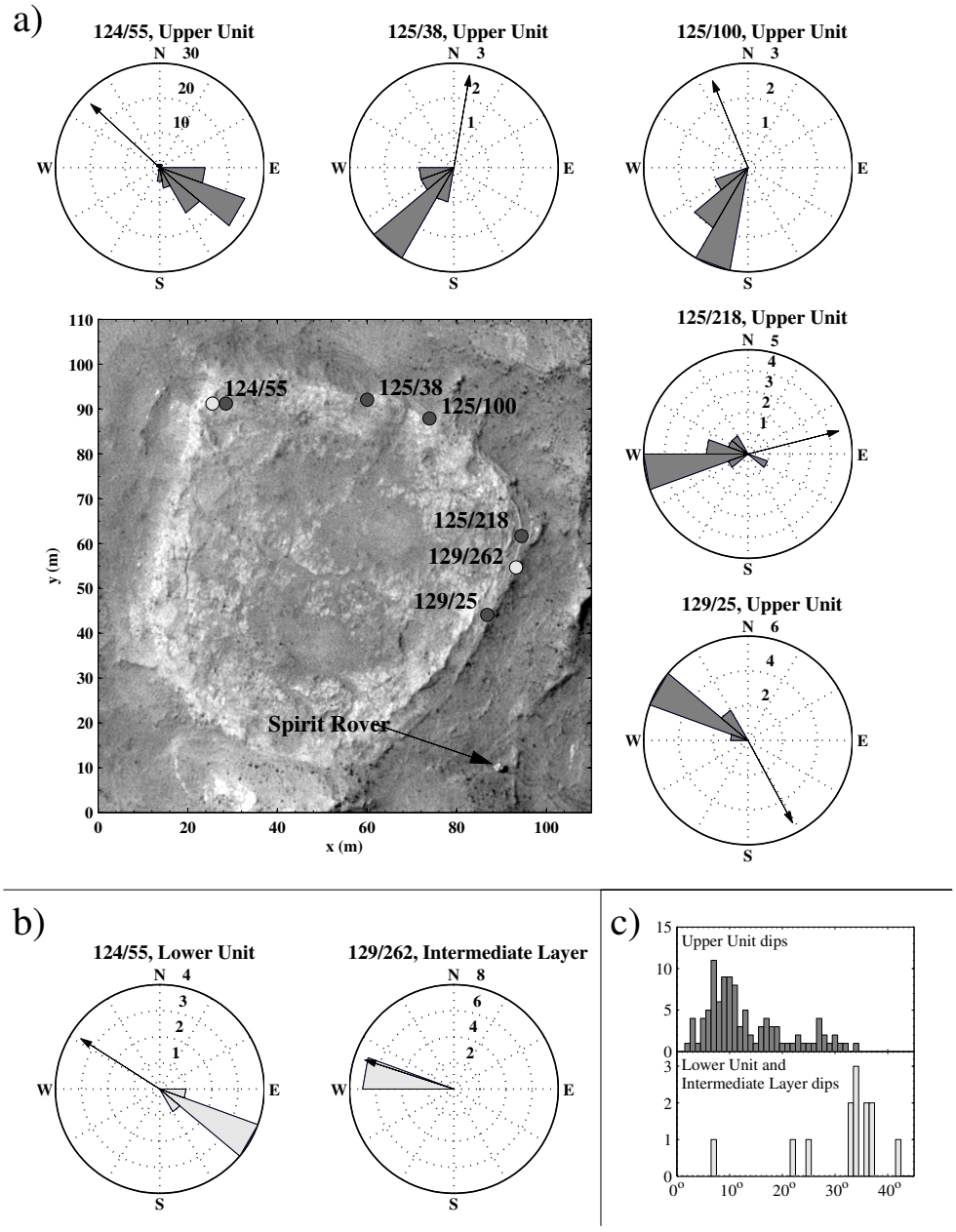

Figure 3.9: Structural data for Home Plate at each of the sites visited by Spirit. For each of the locations indicated on the map, the corresponding rose plot shows dip azimuths of the measured beds. The black arrow on each plot shows the average orientation of the associated outcrop face, to demonstrate that they are not correlated with the fitted bedding planes. a) Measurements within the upper unit, for five locations around the circumference. Together, these plots depict the radial inward dipping structure found at Home Plate over nearly half of its circumference. The base map is an orthogonal projection of HiRISE image PSP_001513_1655; north is up. b) Results for the lower unit, taken on the northwest corner, and the intermediate "fin" layer, taken on the eastern margin. These dip azimuths show excellent agreement with the overlying strata of the upper unit. c) Histograms of the overall dip magnitudes for the upper unit, and the lower unit together with the intermediate layer which shows similar dip magnitudes. The generally smaller dips of the upper unit relative to underlying strata implies a shallowing trend with increasing height in the stratigraphic section.

3.1.6.2 Lower Unit Results

The lower unit of the stratigraphy was best imaged at the northwestern corner of Home Plate, and this was the only location suitable for structural analysis. Overall, the lower unit appears to have low resistance to physical erosion, and primarily erodes back into nearly planar outcrops. Such small topographic variation renders much of the unit unsuitable for this study, due to the inability to uniquely determine the three-dimensional attitude from a linear exposure. Only one area, on the rock Barnhill, had suitable surface topography to allow derivation of the dips within the lower unit. The images of Barnhill best suited to this analysis were from Spirit's Front Hazcam on sol 751. From this area, six bedding traces were extracted which were well fit by planes. The dip azimuth of these beds is uniformly southeast. The mean dip angle for the whole dataset was fairly steep at 26°, with the steepest being over 36°. The lower unit bedding attitudes are nearly identical in strike, but have slightly higher dips compared to the upper unit strata directly above them.

3.1.6.3 Intermediate Layer Results

On the east side of Home Plate, the erosion resistant layer immediately below the upper unit is exposed parallel to bedding in several places. Where images are available at close range, it is possible to tightly constrain the structure. Here, we made seven measurements of the bedding which showed excellent agreement in attitude. For this layer, the mean azimuth was N74°W, roughly radial to Home Plate, with a standard deviation of only 3°. The dips within this unit are the steepest measured at Home Plate, ranging from 33°–42°, with a mean of 36°. This result is significant in that it lies at or above the angle of repose, where dry sediment becomes unstable to avalanching.

3.1.6.4 Upper Unit Results

The upper unit of Home Plate is particularly well suited to the structural topographic analysis described here, due to characteristic erosional patterns. In many places, this unit has eroded to form undulating surfaces and ∼10 cm scale spurs which project out of the outcrop face. This surface relief allows well-constrained measurements of the three-dimensional bedding structure.

Imaging at each of the four locations mentioned above provided adequate topography for structural measurements of the upper unit. A total of 93 measurements were used in this analysis from all of the sites.

Overall, the dip magnitudes within this part of the stratigraphic section range from roughly 0°–35°, with a 1-σ range of 5°–25°. Dip azimuths vary widely between outcrops, although they exhibit a consistent trend at each individual location. Azimuths overwhelmingly trend southeast at the first site visited by Spirit, on the northwestern corner of Home Plate, as shown in Figure 3.9. This orientation projects roughly into the outcrop at this location, radial to the Home Plate structure. Here, a large number of beds could be analyzed due to thorough imaging at close range which minimizes noise in the topographic data. At the second and third outcrops along the northern edge, Site 125, positions 38 and 100, similarly consistent trends were found despite the smaller number of usable layers. At both of these locations, dip directions were uniformly southwest, which again corresponds to the direction towards the center of Home Plate. At the fourth and fifth sites on the eastern margin, strata dip westward and northwestward respectively, again both in the radial direction.

The upper unit of Home Plate exhibits ubiquitous cross-stratification, which complicates structural measurements. However, all of the measurements were made in areas of low-angle cross-bedding to minimize this effect. At the first outcrop, where the most measurements were made, layers showed a mean slope perpendicular to the overall trend of less than 3°, up to a maximum of only 8°. The fact that the variability induced by cross-stratification is small is also shown simply by the tightness of the calculated distributions around a mean dip direction, as illustrated by Figure 3.9.

3.1.7 Discussion

The most consistent hypothesis for the origin of Home Plate includes rapid deposition of material by a pyroclastic surge, followed by possible aeolian reworking. Evidence of ballistic ejecta in the form of a bomb sag, and steeply inclined strata with variable bedding and grain sorting characteristics are consistent with such a high-energy process. While an impact event could also produce a surge

with similar deposits, chemical evidence, most notably the lack of Ni enrichment, makes this a less favorable scenario, as discussed by *Squyres et al.* (2007). The presence of abundant vesicular basaltic rocks in the area further strengthens the case for a volcanic origin.

3.1.7.1 Structure and Origin of Home Plate

One of the most striking characteristics of Home Plate is its bowl-shaped internal structure. Any depositional model must take account of this unusual attribute. One possible interpretation is that Home Plate is itself the volcanic vent which supplied the material for the observed deposits. Terrestrial analogs include tuff rings and maar volcanoes, both low relief hydrovolcanic edifices which often exhibit surge deposits. In this case, the localized nature of the Home Plate materials can be accounted for, as proximal deposits are thicker and more volatile enhanced than distal beds, and therefore more likely to be preserved. Both the bomb sag in the lower unit and the cross-bedding of the upper unit further implicate a source proximal location (*Wohletz*, 1998). Although it is difficult to put a quantitative constraint on the vent distance from a single bomb, ballistic modelling by *Wilson and Head* (2007) for a clast of this size strongly suggests a local source within Gusev crater, perhaps within a few kilometers. On the other hand, the lack of additional large ejecta blocks along with the well-sorted nature of the clastic rocks seen at some locations imply a degree of physical sorting which is not likely to be found at proximal locations, suggesting Home Plate itself is not the volcanic source. In addition, the size of Home Plate is at the very lower limit for tuff rings or maars on Earth, which are more typically hundreds of meters to kilometers in scale (*Cas and Wright*, 1987). Home Plate is only 80 meters in diameter, and potentially analogous deposits in the Columbia Hills are even smaller. Finally, the observation of bedforms interpreted to be oblique or nearly parallel to flow direction, as in Figures 3.3 and 3.4, is unexpected given the radial outward flow direction implied if the center of Home Plate is the volcanic source and the cross-bedding is primary. If the upper unit has been reworked by the wind, the flow direction does not provide information about the vent location.

While it remains possible that the center of Home Plate is the vent which produced the stratified

material, our favored interpretation for the radial structure is deposition by a volcanic surge into a preexisting depression, most likely an impact crater. Surge deposits are well known to drape underlying topography and thicken in topographic lows (*Reading*, 1996). Further, they are capable of overriding rough topography, and even traveling up topographic slopes (*Crowe and Fisher*, 1973; *Waters and Fisher*, 1971). In this case, the thin surge beds could have been stripped away from most flat-lying areas, but remain protected within a natural depression. The rim of the preexisting impact crater could have been eroded before or after deposition by the pyroclastic surge, consistent with observed crater degradation seen elsewhere at Gusev crater (*Grant et al.*, 2005). Infilling by pyroclastic material is consistent with both the steepness and upward shallowing of dips observed from the lower unit and intermediate layer to the upper unit. Evidence of topographic draping has also been found on the ridges surrounding Home Plate and on Husband Hill, directly to the north (*Lewis et al.*, 2007; *Crumpler et al.*, 2006). Deposition in a fresh, primary crater of this diameter would imply a maximum thickness up to ∼16 m for the Home Plate material (*Melosh*, 1989), although depth measurements of similarly sized degraded craters on the Gusev plains suggests a few meters maximum thickness to be more likely.

3.1.7.2 Origin of Upper Unit Cross-bedding

While the lower unit of Home Plate is likely to be a primary surge deposit, the cross-stratified upper unit of Home Plate may have undergone aeolian reworking and later lithification. The structural attributes of the upper unit are most consistent with a primary volcaniclastic origin. The inward-dipping, bowl shape of the unit can be explained by draping of a topographic depression, as inferred for the lower unit. No evidence for a depositional hiatus in the form of an disconformity has been found at the base of the upper unit on either side of Home Plate, from structural or morphologic observations. Dip measurements of the underlying units average 25° for the west side and 35° for the east side. Particularly on the east side where strata are steepest, formation of aeolian dunes on a substrate approaching the angle of repose is unlikely. Pyroclastic surges in contrast are capable of overriding topographic obstacles and depositing material on steep uphill slopes, particularly when

the ash cloud has a higher fraction of entrained water to increase cohesion (*Cas and Wright*, 1987; *Cole et al.*, 2001). Post-depositional compaction of the sediment alone can not explain the observed magnitude of the radial dips, requiring a volume loss of tens of percent. In the case that Home Plate is itself the volcanic vent, evacuation of the magma chamber, and to a lesser extent thermal contraction, could provide additional inward collapse and rotation of the overlying sediments.

Sedimentological observations suggest varying degrees of physical processing for the sediment population which comprises the upper unit of Home Plate. Images from the east side show several millimeter-size particles, and one clast nearly three millimeters in length. The coarse tail of the grain size distribution seen at this location (Figure 3.8) is more consistent with a pyroclastic origin, although the grains are not large enough to rule out aeolian transport by saltation-induced creep. In contrast, observations on the west side show a narrow size distribution of particles, with a similar size range to that observed at the El Dorado sand sheet (Figure 3.7). The well-rounded shape of many clasts on the west side suggests extensive transport and abrasion, as would be expected in an aeolian environment. We can not rule out the possibility that a fraction of the upper unit is comprised of accidental material that was already rounded and sorted before being swept into a pyroclastic surge. Hydrovolcanic deposits often include a large portion of material which is derived from preexisting country rock (*Ollier*, 1967; *Lorenz*, 1973). However, the chemical similarity to both the lower unit and nearby vesicular basalts suggests that the upper unit material is derived from a common source (*Squyres et al.*, 2007; *Schmidt et al.*, 2008). In summary, structural and sedimentological observations from the east side are supportive of a primary pyroclastic origin for Home Plate. On the west side, however, the observed sedimentology suggests aeolian reworking of pyroclastic materials. Future observations may help resolve this issue. In particular, observations of outsized clasts in the upper unit could constrain its genesis.

Finally, it is notable that no examples of centimeter-scale cross-bedding have been found within the upper unit of Home Plate. The discovery of these small scale bedforms within the bedrock at the Opportunity rover landing site has been critical in establishing the dune-interdune depositional model for the bedrock at that location (*Squyres et al.*, 2004b; *Grotzinger et al.*, 2005). The occurrence

of these bedforms at Meridiani Planum has been put forward as a unique indicator of subaqueous, rather than subaerial flow. In contrast, the lack of similar features at Home Plate is consistent with the interpretation of purely subaerial transport, either within a pyroclastic surge, or by aeolian processes.

3.1.7.3 Implications of a Pyroclastic Surge Deposit at Gusev Crater

The discovery of a preserved volcaniclastic deposit within Gusev crater sheds new light on the geologic history of this location. A common source of explosive volcanism arises from interaction of hot magma with a water reservoir. Particularly for small, basaltic sources such as that inferred for Home Plate, explosions typically result from rapid vaporization of surface or subsurface hydrologic sources (*Wohletz*, 1998; *Cas and Wright*, 1987). While there is little evidence to suggest large amounts of water at the surface in the vicinity of Home Plate, the existence of a ground water reservoir at the time of formation could have provided the necessary trigger for a phreatomagmatic explosion. In this scenario, the very existence of Home Plate may implicate subsurface water in the ancient past, a reservoir which is otherwise difficult to assess.

In addition, the preservation of the Home Plate deposits through lithification provides information about aqueous interaction at this location. The rocks at Home Plate have been eroded to a large degree, and the paucity of loose rocks from the Home Plate sequence suggests poor resistance to physical abrasion. In the event that Home Plate is a primary volcaniclastic deposit, induration could have occurred nearly contemporaneously with deposition. If the cross-bedding of the upper unit represents aeolian reworking of the pyroclastic material, lithification would have to have occurred some time after the volcanic explosion. In either case, water is the most likely mechanism for cementing loose ash particles into coherent rock. Indeed, chemical and mineralogical evidence suggests significant hydrothermal action at Home Plate and within the Inner Basin of the Columbia Hills (*Schmidt et al.*, 2008). The formation of many terrestrial sedimentary rocks is aided by burial and compaction. Similarly, the thick section of sulfate bedrock of Meridiani Planum shows evidence for extensive deflation including crater degradation and a widespread lag of hematite

grains (*Grotzinger et al.*, 2005). Lacking similar morphologic evidence for burial and exhumation at Home Plate, lithification likely proceeded at the surface. More generally, if Home Plate were indeed lithified subsequent to the original volcanism, it demonstrates the potential for preservation of small sedimentary deposits on Mars, which would provide a valuable record of process and conditions through time.

3.1.8 Summary

Quantitative analysis of the sedimentology and structure of Home Plate have provided new constraints regarding its origin. Structural analysis has provided an explanation for the singular observation of the Home Plate stratigraphy here, as the inward dip of the bedding suggests a unique depositional setting. Sedimentological observations have shown a varying clast population between the two sides of Home Plate. Observations on the east side favor a primary pyroclastic origin for the exposed stratigraphy of Home Plate, while observations on the west side are consistent with aeolian reworking of the upper unit. In either case, however, it is clear that Home Plate originates from explosive volcanic activity. The inward dips of the structure may arise as a result of deposition into a preexisting depression, likely an impact crater. Alternatively, the volcanic source may have been situated at the center of Home Plate, where vent collapse could also produce a radial structure. The nature of the lithification of Home Plate remains unknown, although hydrothermal processes are suggested by geochemical evidence. Particularly in the case of aeolian reworking, this lithification must have occurred well after the initial depositional event. The recognition of Home Plate as a pyroclastic deposit provides direct evidence for explosive volcanism on ancient Mars, and may implicate subsurface hydrologic reservoirs as a trigger for the inferred surge. The rich stratigraphy characterized here and at Meridiani Planum by the Opportunity rover provide a framework for outcrop-scale interpretation of layered deposits on Mars.

Acknowledgements

We thank Dave Rubin, Gary Kocurek and John Southard for illuminating discussions and suggestions, as well as Douglas Jerolmack and David Lescinsky for insightful reviews. We are especially indebted to the MER Athena Science and Engineering Teams without whom these observations would not have been possible. Funding for Athena science team members was provided by NASA contracts through Cornell and the Jet Propulsion Laboratory.

3.2 Low Ridge

3.2.1 Introduction

The Mars Exploration Rover Spirit has been exploring the Inner Basin of the Columbia Hills since descending from Husband Hill in early 2006. During her second Martian winter at Gusev, Spirit carried out scientific investigations on and around a small topographic high known as Low Ridge (*Squyres et al.*, 2008; *Arvidson et al.*, 2008). Over the Martian winter and subsequent spring, Spirit extensively studied her surroundings, including a number of stratified outcrops and float rocks between Low Ridge and Mitcheltree Ridge to the north. These ridges are mostly covered by talus, but a few prominent outcrops are found, especially near their base. Rocks on these ridges tend to be more poorly bedded than the units seen at Home Plate. Chemical and mineralogical analyses have shown the outcrop materials analyzed in this area to exhibit significant compositional differences from Home Plate. Most notably, these materials show a higher degree of oxidation, with a large percentage of hematite comprising the iron mineralogy (*Morris et al.*, 2008; *Ming et al.*, 2008). The morphological and compositional differences provide new clues in reconstructing the geologic history of the Inner Basin and the Columbia Hills. This study focuses primarily on physical relationships between these Inner Basin outcrops through sedimentological and structural observations.

3.2.2 Traverse from Low Ridge to Mitcheltree Ridge

Spirit first imaged Low Ridge on sol 778 after leaving Home Plate, and began its winter campaign there shortly after on sol 805. At this location, a series of erosion-resistant beds form an outcrop known as Prat, which stretches over 10 m in length along the northern side of Low Ridge (Figure 3.10). This feature was extensively studied both from remote sensing and *in situ* analyses. Targets included King George Island, within the Prat bed, and the float rock Halley at the base of Low Ridge. After the winter campaign, Spirit traversed a short distance to study the vesicular basalt Esperanza, also imaging an outcrop of bright stratified rock on the eastern side of the ridge, informally named Druzhnaya. On sol 1069, Spirit began to analyze a small outcrop immediately to

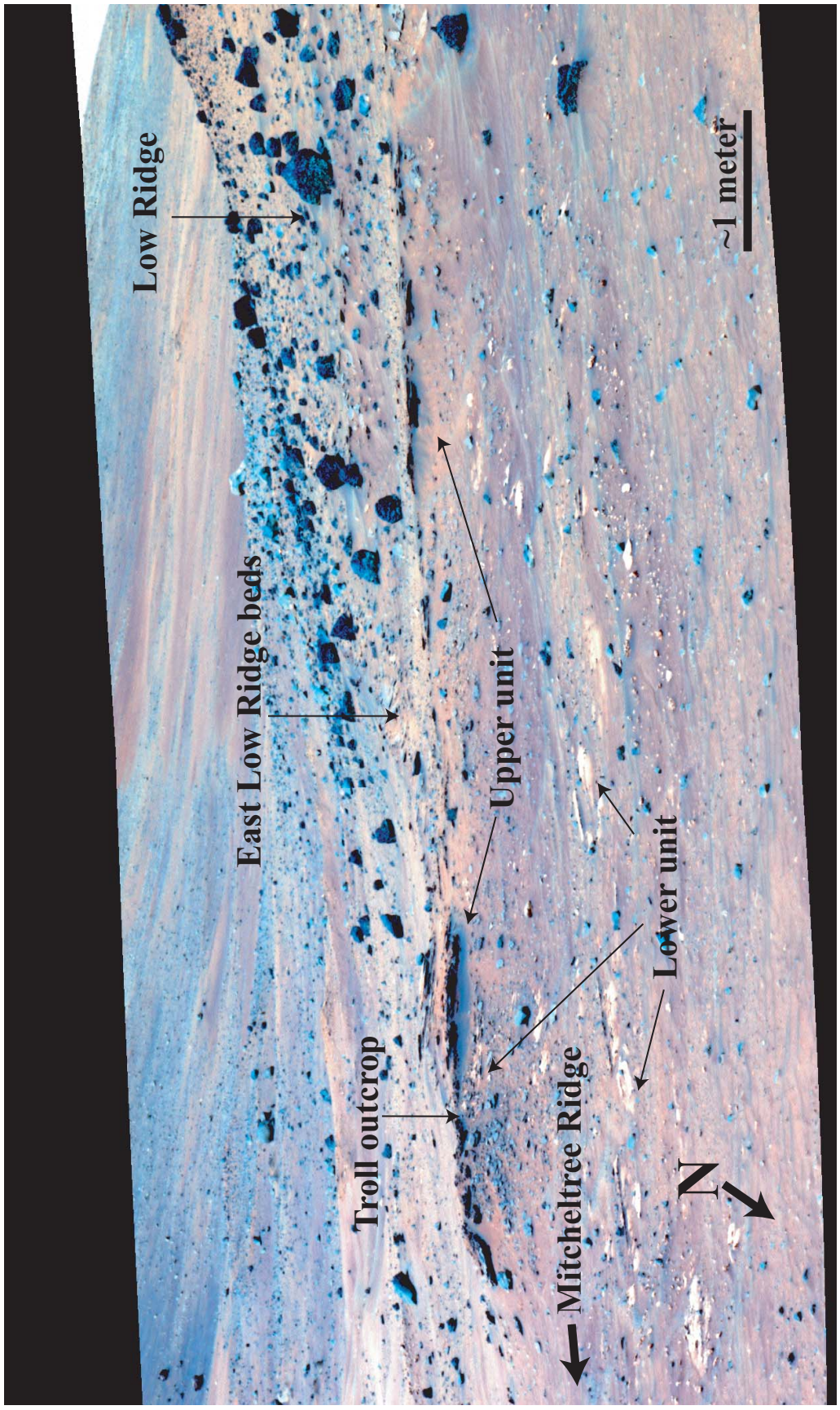

Figure 3.10: Pancam false color view of Low Ridge from sol 778, with major stratigraphic units indicated. Mosaic produced by the Pancam team. Image credit: NASA/JPL/Cornell.

the north of Low Ridge known as Troll. Two distinct units were observed here, with the lower and upper units nicknamed Montalva and Riquelme respectively. Continuing her northward traverse, Spirit imaged the outcrop Bellingshausen at the southern end of Mitcheltree Ridge, and the rock Torquas further north along the ridge.

The ability to study the rocks at Low Ridge is limited by several factors including rover accessibility and obscuration by loose dust and erosional debris. In general, cover by rocks and soil on the ridges is much more extensive than was encountered at Home Plate. Outcrops of material tend to be sparse, and contacts between different units are rarely well exposed. Therefore portions of the stratigraphic sequence remain uncertain. However, the rocks which Spirit has been able to analyze *in situ* represent most of the major classes observed from remote sensing. In particular, Low Ridge and the surrounding outcrops exhibit two morphologically distinct rock types in the outcrops imaged by Spirit. In addition, the abundant vesicular basalts on Low Ridge and diverse soils observed in the area may constitute additional units of the stratigraphy, though they are not addressed directly here.

3.2.3 Lower Unit Stratigraphy

The lower unit of the stratigraphy in this area occurs in place at the Troll outcrop between Low and Mitcheltree Ridge. Here, the exposure exhibits thin, parallel bedding at centimeter scales. MI observations of the target Montalva show the outcrop to be relatively featureless at the 100 µm scale, with hints of a fine-grained clastic texture near the limit of resolution of the MI (Figure 3.12d). The lower unit in the region of Low Ridge is typically brighter and redder than the upper unit as seen by Spirit's multispectral Panoramic Camera (Pancam). This is apparently only due to dust obscuration, as a brush of the Montalva outcrop on 1085 revealed a much bluer surface in Pancam images. The float rock Halley at the base of Low Ridge has a similar morphology in Pancam and MI images, and is likely correlative with Montalva given its proximity and stratigraphic position. There are significant geochemical differences between Montalva and Halley, which may reflect small-scale heterogeneity, and/or hydrothermal alteration, which is inferred to have played an important role in

this area (*Ming et al.*, 2008). Aditionally, rocks of similar color and mophology outcrop at the base of the southern end of Mitcheltree Ridge, but were not imaged by the MI. Although this unit shows some faint bedding, it was not possible to extract structual information due to its limited exposure.

3.2.4 Upper Unit Stratigraphy

The upper stratigraphic unit in this area outcrops along the north and east sides of Low Ridge (Prat, King George Island, and Druzhnaya), in the Troll outcrop (Riquelme), and north along Mitcheltree Ridge (Bellingshausen and Torquas). This unit is typically expressed as moderately to poorly stratified parallel beds. Individual layers cannot typically be traced for more than a few tens of centimeters, due to poor stratification and dust cover. The true thickness of the unit is uncertain; strata tens of centimeters above the Prat outcrop are visible at Low Ridge, but were inaccessible to the rover.

3.2.4.1 Sedimentology

The sedimentological properties are a unique and defining feature of this unit. At microscopic scales these rocks have a distinct clastic texture, with highly rounded, well-sorted grains of roughly millimeter size comprising the strata, as seen in Figure 3.12a–c. The rocks appear to be clast supported, with little or no visible matrix. Grain sizes appear to be extremely uniform throughout the stratigraphy, and no obvious grading has been identified within the outcrops imaged with the Microscopic Imager. Figure 3.13a shows the observed grain-size distributions relative to some of the rocks analyzes at Home Plate. The outcrops from Low Ridge to Mitcheltree Ridge (shown in black) all have extremely similar grain-size distributions with the histogram maximum at about 800 µm. In comparison, the rocks seen at Home Plate (shown in gray) have uniformly finer grain sizes, with little overlap between the two sets of distributions. Although the Ridge rocks have a collectively coarser clastic population, the degree of sorting is equally high as was observed at Home Plate, when plotted using the logarithmic phi (ϕ) scale (Figure 3.13b). This distinctive texture has only been observed in this area southeast of Home Plate, and strongly suggests a common genesis for these

outcrops.

3.2.4.2 Structure

The geometry of the layers at Low Ridge constrains their formation and relationship to other structures in the Inner Basin, particularly the nearby layered rocks of Home Plate. The most striking attribute of the strata in this area is their high variability in orientation over short distances. At Low Ridge, the outcrop exposed on the eastern face, Druzhnaya, shows a consistent westward dip, while the the north face shows an eastward dip. The mean attitude of the bedding at Druzhnaya is 12° to the west, while the exposure on the north face, Prat, dips at an average of 7° eastward (Figure 3.11). The Troll outcrop between the two ridges shows a complex structural trend, as shown by the rose plot at the lower right in Figure 3.11. The dips here are generally southwest trending, closing off the structural synform of Low Ridge. At Mitcheltree Ridge, a similar inward trend is observed, with the Bellingshausen outcrop on the east side showing eastward dips, and an outcrop further north on the west side exhibiting steep easward dips. The stratigraphy here does not follow the consistent bedding attitudes seen nearby at Home Plate (indicated in the map in Figure 3.11), where strata were observed to have radial inward orientations. Instead, the bedding at Low and Mitcheltree Ridge are dominated by their own local structural trends, oriented roughly inward toward the ridges themselves. The stratal geometries thus form shallow synforms over only a few meters across the ridges.

3.2.5 Interpretations

The diverse structural and sedimentological characteristics of the layered rocks found in the Inner Basin of the Columbia Hills suggest a similarly complex formation sequence. The complex structural attribues of the ridges could suggest two possibilities: 1) Deposition of the layered materials on an uneven substrate, which led to the layers inheriting orientations from the underlying topography. 2) Disruption of layers by impact processes or tectonic activity. No clear evidence of faulting has been observed in the stratigraphy thus far, and there are no obvious impact sites associated with the

ridges. Rather, draping of material over preexisting topography is favored, as has also been invoked for Home Plate (*Lewis et al.*, 2008b). This hypothesis is also consistent with a pyroclastic origin for the sediment, as proposed in section 3.1.8.

The sedimentology of the upper unit in this area is particularly interesting given its unique grain size distribution. Although the Home Plate upper unit was observed to contain ∼200–400 µm grains, the ridges show coarser sediment with roughly a factor of 3 larger diameters. While the Home Plate clasts were consistent with transport by aeolian saltation, as concluded by comparison to the modern El Dorado dune field, the sediment in this area would be coarser than has been observed to occur in saltation-related aeolian bedforms. Coarser granule ripples, which move by impact-induced creep, have been observed in isolated cases at Gusev, although at even coarser sizes with a mean of ∼1.3 mm (*Jerolmack et al.*, 2006). An alternative possibility, given the suggested provenance as a pyroclastic deposit, is that the grains formed as accretionary lapilli. These spherical particles can form in volcaniclastic ash clouds by the agglomeration of fine particles in the presence of sufficiently high water content (*Cas and Wright*, 1987). Indeed, these clasts are precisely of the size range predicted for accretionary lapilli on Mars. Depending on the magma water content, *Wilson and Head* (2007) predict lapilli sizes to range from 700 to 900 µm, roughly an order of magnitude smaller than commonly form on Earth due primarily to the lower densities predicted in Martian pyroclastic surges.

Although the contact between the two stratigraphic units is poorly exposed in this area, an attempt was made to image the contact at the Troll outcrop on sol 1085. No sharp transition was observed within the area imaged by the Microscopic Imager. Rather, a possible gradational transition was observed, from the featureless appearance of the Moltalva target to the spherical clasts found at Riquelme, immediately above. In the transition zone, the outcrop becomes rougher, with several round nodules exposed in the size range of the clasts seen in the upper unit. This observation is also consistent with an accretionary origin for the clasts in the upper unit, possibly reflecting a gradual change in eruptive conditions as the sediments were deposited.

In combination with the stratigraphy analyzed at Home Plate, the area around Low Ridge

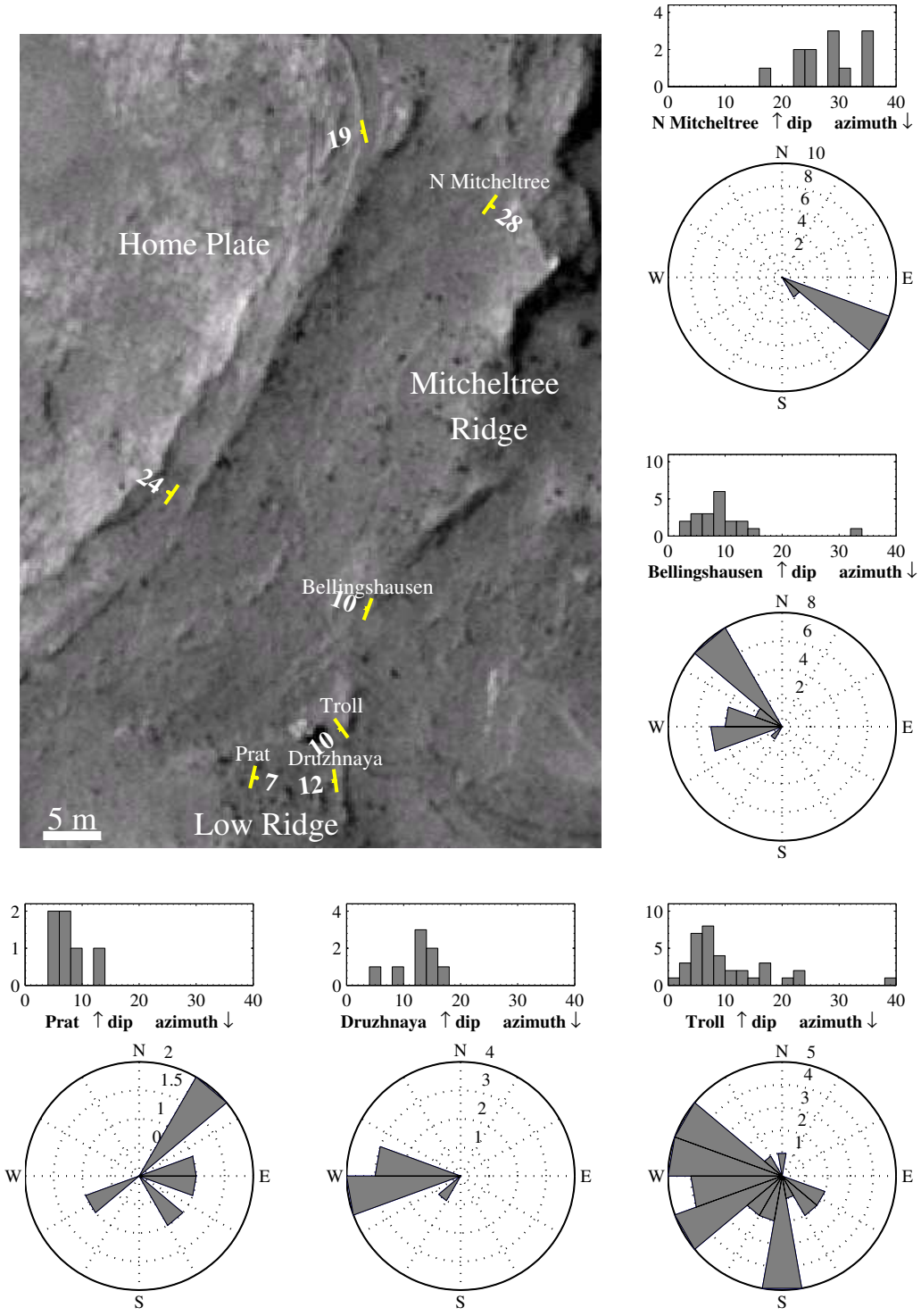

Figure 3.11: Structural map of Low and Mitcheltree Ridge and surroundings on HiRISE basemap. For each of the 5 sites on the ridges, dip histograms and rose plots of the dip azimuths are shown for all beds measured. Both ridges form structural synforms, with bedding dipping inward on all sides. Strata do not follow the radial trend of Home Plate, shown by two representative dip marks. As with Home Plate however, the variable orientations are consistent with draping of topographic depressions. HiRISE background is image PSP_001513_1655.

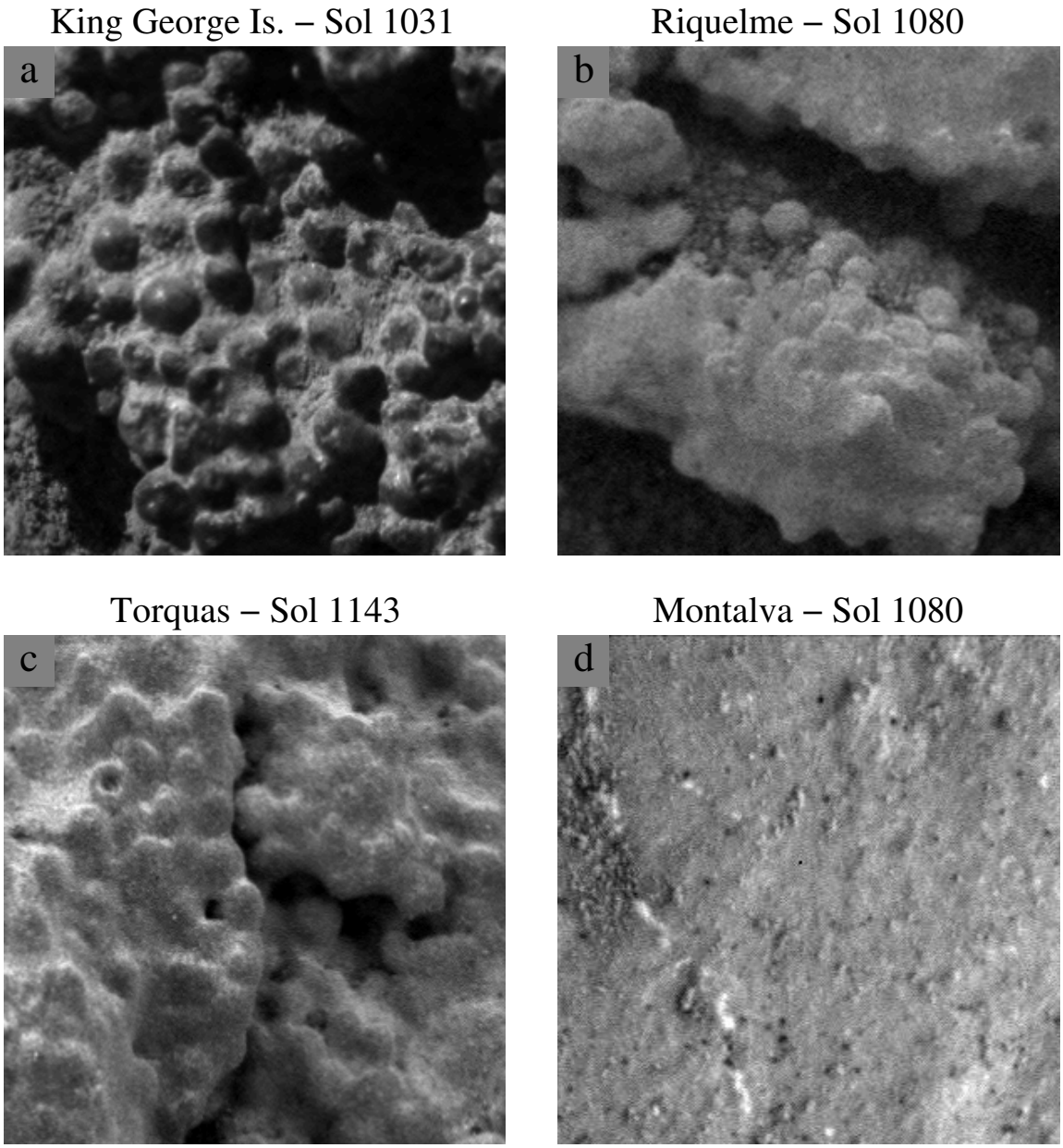

Figure 3.12: Microscopic Imager (MI) views of four likely pyroclastic rocks in the Low Ridge area. a) Image of upper unit rock King George Island, exposed on Low Ridge. Well rounded and sorted, millimeter-size clasts comprise the rock. Image 2M217894386RALAS20P2977M2M1. b) Similar morphology seen at Riquelme, on the Troll outcrop on sol 1080. Image 2M222243837RALASCGP2976M2M1. c) Torquas, a third rock with large spherical grains on Mitcheltree Ridge, from sol 1143. Image 2M227835190RALAS4JP2936M2M1. d) Image of a lower unit rock known as Montalva, on the Troll outcrop, taken on sol 1070. Only hints of a clastic texture are seen at this scale, likely indicating a fine-grained composition. Small dark spots are likely clasts near the limit of resolution of the image (<100 µm). Image 2M222241654EFFASCGP2939M2M1. All images are 1 cm across.

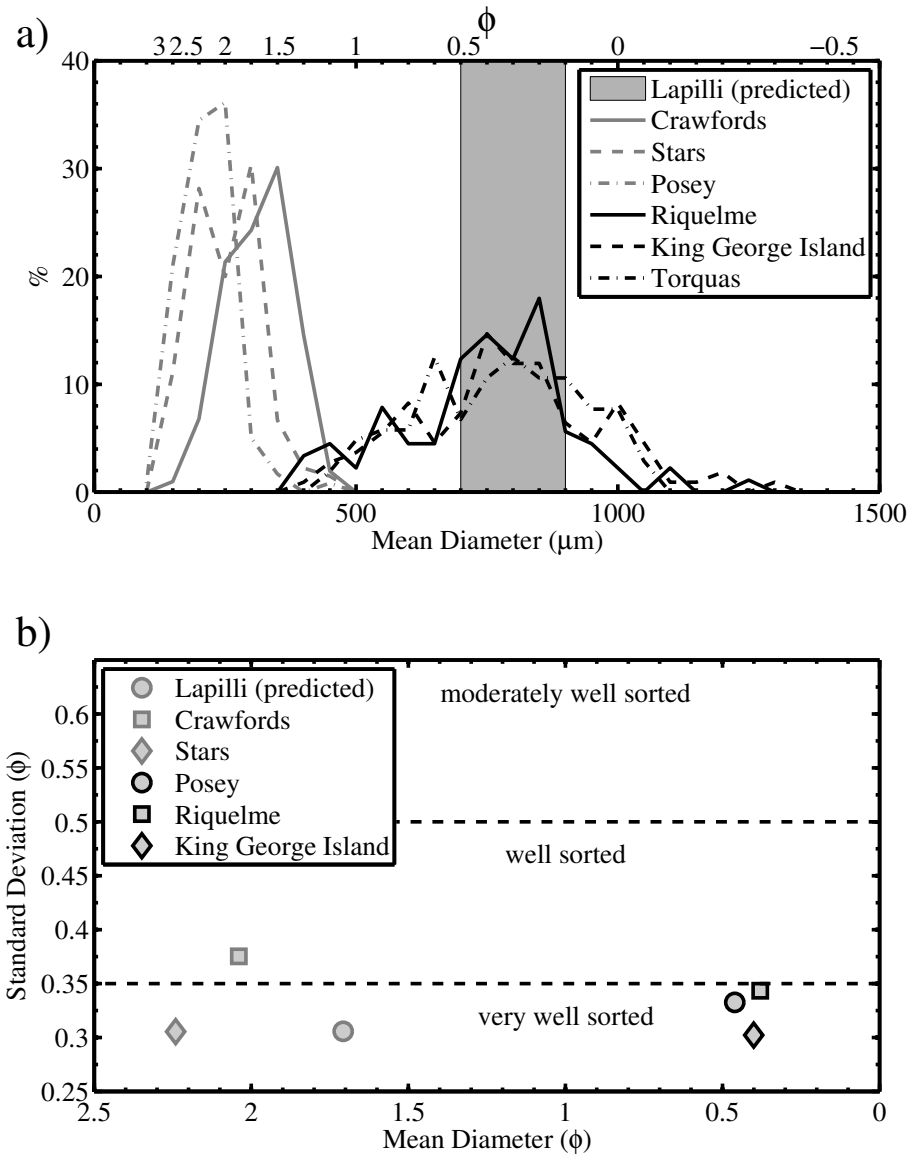

Figure 3.13: a) Grain size histograms for rocks observed with Spirit's Microscopic Imager. King George Island, Torquas, and Riquelme are located on Low Ridge, Mitcheltree Ridge, and the Troll outcrop respectively. Crawfords, Stars, and Posey are rocks observed in the upper unit of Home Plate, for comparison. All of the Ridge targets have extremely similar clastic populations which are clearly distinct from Home Plate rocks, supporting the case that they together comprise a single, separate stratigraphic unit. The shaded region marks the size range predicted for accretionary lapilli on Mars by *Wilson and Head* (2007). The coincidence of the distributions with this prediction is consistent with an accretionary origin for the highly rounded grains which comprise the unit. b) Plot of mean and standard deviation of the sediment populations, using the logarithmic phi scale. Although the Ridge outcrops have an overall coarser population, the high degree of sorting is equivalent to that observed in Home Plate rocks.

and Mitcheltree Ridge exhibits a rich history within the Inner Basin. Chemical and mineralogical studies show extensive alteration, consistent with hydrothermal interaction (*Schmidt et al.*, 2008). Stratigraphic and structural observations point to a dynamic series of depositional processes. The correlation of units over tens of meters shows a common genesis for Low Ridge and Mitcheltree Ridge. Although in the simplest hypothesis these structures are inferred to have formed contemporaneously with Home Plate, the exact stratigraphic relationships remain unclear. Most notably, cross-bedding of the type seen at Home Plate has not been observed elsewhere in the region. The inward dipping trends observed at both the ridges and Home Plate suggest preferential preservation of the stratigraphy in local topographic lows. These measurements remain consistent with the suggestion of *Lewis et al.* (2008b), that a small crater may have been the source of the depression filled by the Home Plate sediments, although the additional observations point to more complex preexisting topography. In addition, the bedding orientations seem to require meters of erosion in the modern topographic lows, further complicating the landscape history in the Inner Basin.

Chapter 4

Rhythmic Stratigraphy in the Martian Rock Record

4.1 Introduction

In this chapter we present the detection of quasiperiodic bedding in the martian rock record. This attribute is found in several locations around the planet, with a concentration in western Arabia Terra. First, I introduce the methods for deriving stereo topography from HiRISE stereo images and data analysis techniques. This is followed by a discussion on the detection and possible origin of rhythmic stratigraphy specifically in Arabia Terra region. Finally, the wider occurrence of regularly cyclic bedding on Mars is assessed, including descriptions of the local geologic context and structural attributes. In addition, several representative sections are shown where aperiodic bedding has been identified. Likely formation scenarios are discussed for the set of quasiperiodic sedimentary rocks on Mars.

4.2 Methods

4.2.0.1 Digital Topographic Extraction

Digital topographic data are extracted from stereo images via the method of *Kirk et al.* (2008), using the Socet Set software package. Camera positions and velocities are refined by controlling tiepoints to the Mars Orbiter Laser Altimeter global dataset, which has a nominal vertical accuracy

of ∼1 m (*Smith et al.*, 2001). Final Digital Terrain Models (DTMs) are produced at a grid spacing of 1 m, roughly equivalent to 3 pixels for full-resolution HiRISE images. Topographic artifacts and areas of interpolation are typically minor. Seams between adjacent CCDs typically result in discontinuities on the order of tens of centimeters, and are avoided for scientific analyses. Inaccuracies resulting from spacecraft jitter over the course of image acquisition are minor. Orthographically rectified images (orthoimages) are generally produced in Socet Set at a corresponding pixel scale, although full resolution orthoimages (25 cm/pixel) are occasionally used.

4.2.0.2 Structural Measurements

To correctly reconstruct the stratigraphic record, the three-dimensional orientation of bedding in an outcrop must be measured and accounted for. This is particularly important for the outcrops studied here, which can be heavily faulted. We have extracted topographic profiles along the edges of beds for each outcrop, where natural curvature can adequately constrain the planar orientation. Profiles do not cross faults in the rocks where displacement may have occurred. Further, we avoid areas adjacent to faults where folding can distort beds into non-planar surfaces. Planar coefficients, along with 95% confidence intervals, are determined via linear regression. From the confidence intervals, we evaluate the maximum deviation of the normal vector of the plane from the best fit, rejecting those with an uncertainty above 2°. From the regression coefficients of x and y, a and b respectively, the azimuth θ and magnitude ϕ of the dip are calculated as:

$$\tan\phi = \sqrt{a^2 + b^2}, \tag{4.1}$$

$$\tan(\theta + \pi) = \frac{b}{a}. \tag{4.2}$$

4.2.0.3 Extraction of Stratigraphic Records

To extract an accurate profile of an outcrop, bedding orientations must be relatively consistent across the section. Measurements of stratal geometry are taken where possible throughout an outcrop, and a mean orientation (θ_0, ϕ_0) is calculated for the entire section. As such, beds are assumed to be

parallel planes with variable offsets. For topographic profile consisting of a set of observations (x_i,y_i,z_i), the vertical bed offset d is calculated as:

$$d = \langle \tan\phi_0 \cdot \cos\theta_0 \cdot x + \tan\phi_0 \cdot \sin\theta_0 \cdot y + z \rangle_i, \tag{4.3}$$

with the true thickness t between adjacent bedding planes:

$$t = \Delta d \cdot cos\phi_0. \tag{4.4}$$

This basic technique can also be used to obtain a corrected high-resolution grayscale and slope record for an outcrop. Elevation and grayscale values are extracted along a specified profile. Again, the vertical offset is determined for every sampled point, and used to sort pixels in stratigraphic order. We then interpolate the record to constant stratigraphic spacing for the purposes of spectral analysis. Typical sampling intervals are 0.1 m, as low-angle topographic exposures dramatically increase stratigraphic resolution. The interpolation interval is chosen to be the mean stratigraphic spacing of the original datapoints. Two-dimensional grayscale profiles can also be extracted and averaged along the bedding direction to increase the signal-to-noise ratio of the record. This tends to be particularly useful where variable lighting of small scale topography can induce distortions in the grayscale signal.

4.2.0.4 Spectral Analysis

We perform spectral analysis on the topographically corrected and uniformly resampled depth-series signals to determine whether statistically significant quasiperiodic components are present. Power spectra are estimated via the multitaper method of *Thomson* (1982), using three Slepian data tapers. Statistical confidence levels are determined via the robust method of *Mann and Lees* (1996). The spectral background is modeled as that of a first-order autoregressive ($AR(1)$) process, of the form

$$S_n = \alpha S_{n-1} + \omega_n, \tag{4.5}$$

where $0 \leq \alpha < 1$ is the lag-one autocorrelation coefficient, and ω_n is a Gaussian-distributed random value. The robust background fitting technique of *Mann and Lees* (1996) involves both reshaping (by initially removing probable periodic components) and smoothing of the power spectrum. A smoothing interval of 0.2 m^{-1} is used for all spectra, and the choice of value has been found to have only a small effect on the final results.

4.3 Quasi-periodic Bedding at Arabia Terra

Originally published in:
Lewis, K. W., O. Aharonson, J. P. Grotzinger, R. L. Kirk, A. S. McEwen, and T.-A. Suer (2008a), Quasi-periodic bedding in the sedimentary rock record of Mars, *Science*, *322*, 1532–, doi: 10.1126/science.1161870

Abstract

Widespread sedimentary rocks on Mars preserve evidence of surface conditions different from the modern cold and dry environment, although it is unknown how long conditions favorable to deposition persisted. Here, we use 1 m stereo topographic maps to demonstrate the presence of rhythmic bedding at several outcrops in the Arabia Terra region. Repeating beds are ∼10 meters thick, and one site contains hundreds of meters of strata bundled into larger units at a ∼10:1 thickness ratio. This repetition likely points to cyclicity in environmental conditions, possibly as a result of astronomical forcing. If deposition were forced by orbital variation, the rocks may have been deposited over tens of millions of years.

4.3.1 Introduction

Sedimentary rocks record surface and environmental conditions throughout the history of Mars (*Malin and Edgett*, 2000; *Christensen and Moore*, 1992). Landed missions have studied a few locations in detail, but most deposits remain accessible only from orbital data. The High Resolution Imaging Science Experiment (HiRISE) (*McEwen et al.*, 2007) has revealed meter-scale bedding in the rocks at many locations. Stereo observations allow the three-dimensional structure of these stratified outcrops to be determined, from which bedding orientations and true thicknesses can be calculated. Here, we report on the measurement of several stratified deposits in the Arabia Terra region that contain highly rhythmic bedding and may record a history of orbitally forced variations in surface conditions. Previous attempts have been made to correlate layers within the north polar ice cap of Mars to the most recent orbital history (*Laskar et al.*, 2002; *Milkovich and Head*, 2005). In contrast, the rocks of Arabia Terra record ancient surface conditions.

4.3.2 Overview

The intracrater layered deposits of Arabia Terra are thick sequences of sedimentary rocks distributed widely across Mars from 350° E to 30° E and from the equator up to 25° N (*Edgett*, 2002). Although the deposits are separated by large distances, the region in which they occur is greater than 500 × 1000 km in area. Most sequences are several hundred meters thick and have eroded back to remnant mounds on the floors of large craters, natural locations for both deposition and preservation. Many deposits have a stair-stepped morphology, with the differential resistance of the outcrops highlighting their stratified internal structure (*Malin and Edgett*, 2000). The origin of these sedimentary rocks is uncertain, although there is a general lack of valley incision in western Arabia Terra (*Carr and Chuang*, 1997; *Hynek and Phillips*, 2003), and there is no observed evidence for fluvial channels within these deposits. While erosion may have removed overlying strata (*Hynek and Phillips*, 2003), the craters we studied do not have breached or heavily incised rims, and show little evidence for lacustrine processes.

Among the craters containing light-toned layered deposits in Arabia Terra, four have adequate stereo coverage to make quantitative measurements of the stratigraphy. These sedimentary sequences contain tens to hundreds of beds of similar morphology with planar and parallel bedding. Faults offset the stratigraphy in places, but we have avoided these areas in our analysis. Extensive aeolian erosion has revealed the thick sections, and also provides a clue to the depositional origin of the rocks. Few craters are observed on the light-toned deposits, and little talus is observed at the base of steep slopes, suggesting that the deposits are weakly lithified and composed of grains fine enough to be transported away by modern aeolian activity. The striking differential resistance to erosion seen across each bed points to a repeated change in the depositional environment as the strata were formed.

4.3.3 Method

To assess the structure of layered deposits, we created digital terrain models (DTMs) with 1 m post spacing from HiRISE stereo images, as described in section 4.2.0.1. These products are registered

to the Mars Orbiter Laser Altimeter (MOLA) dataset, and have vertical accuracy of <1 m, allowing analysis of meter-scale bedding (Table S1). Figure 4.1 shows a cross section along one outcrop, demonstrating that decameter-scale layers are well resolved in the stereo DTM. Although the apparent thicknesses are variable in plan view, the true bed thicknesses are highly regular when the erosional topography and southward dip are accounted for. Accordingly, bedding orientations are calculated via linear regression, and are typically derived from hundreds of individual topographic data points, resulting in a precision of <0.5° on the dip of a bed. We made measurements throughout each section to ensure the orientation was consistent. At the Becquerel crater site, a slight change in bedding orientation was observed and accounted for within the upper 80 meters of section. We then identified bed boundaries in plan view and projected each to a common reference frame using the measured orientation of the outcrop.

4.3.4 Results

For each of the Arabia sites, the bed thicknesses are tightly clustered around a mean value (Table 4.1, Tables 3.3–3.7). The thinnest beds are still above the resolution limits of both the images and the DTMs, which have 1 m pixel scale but typically sample the stratigraphic column at an even higher ∼0.1 m spacing due to the slope of the outcrops. Although the scale of the bedding varies from site to site, it is consistent among outcrops at the same location. Within the two unnamed craters at 8° N, 353° E and 8° N, 359° E, the characteristic thicknesses are about 10 and 13 m respectively. At Crommelin crater (5° N, 350° E), beds are 20 m thick, whereas Becquerel (22° N, 352° E) shows two scales of stratification at 3.6 and 36 m. The distribution of bed thicknesses at each location is consistent with a normal distribution via the K-S test. Alternative hypotheses that the data are either exponentially or power law distributed can be rejected. By comparing the data to ideal distributions via the Kolmogorov-Smirnov test, the hypothesis that the bed thicknesses were drawn from an exponential distribution may be rejected for four out of five datasets at a 95% confidence level. For a power law distribution, the null hypothesis can be similarly rejected for all of the datasets. In contrast, a normal distribution is consistent with all of the datasets using this test. We

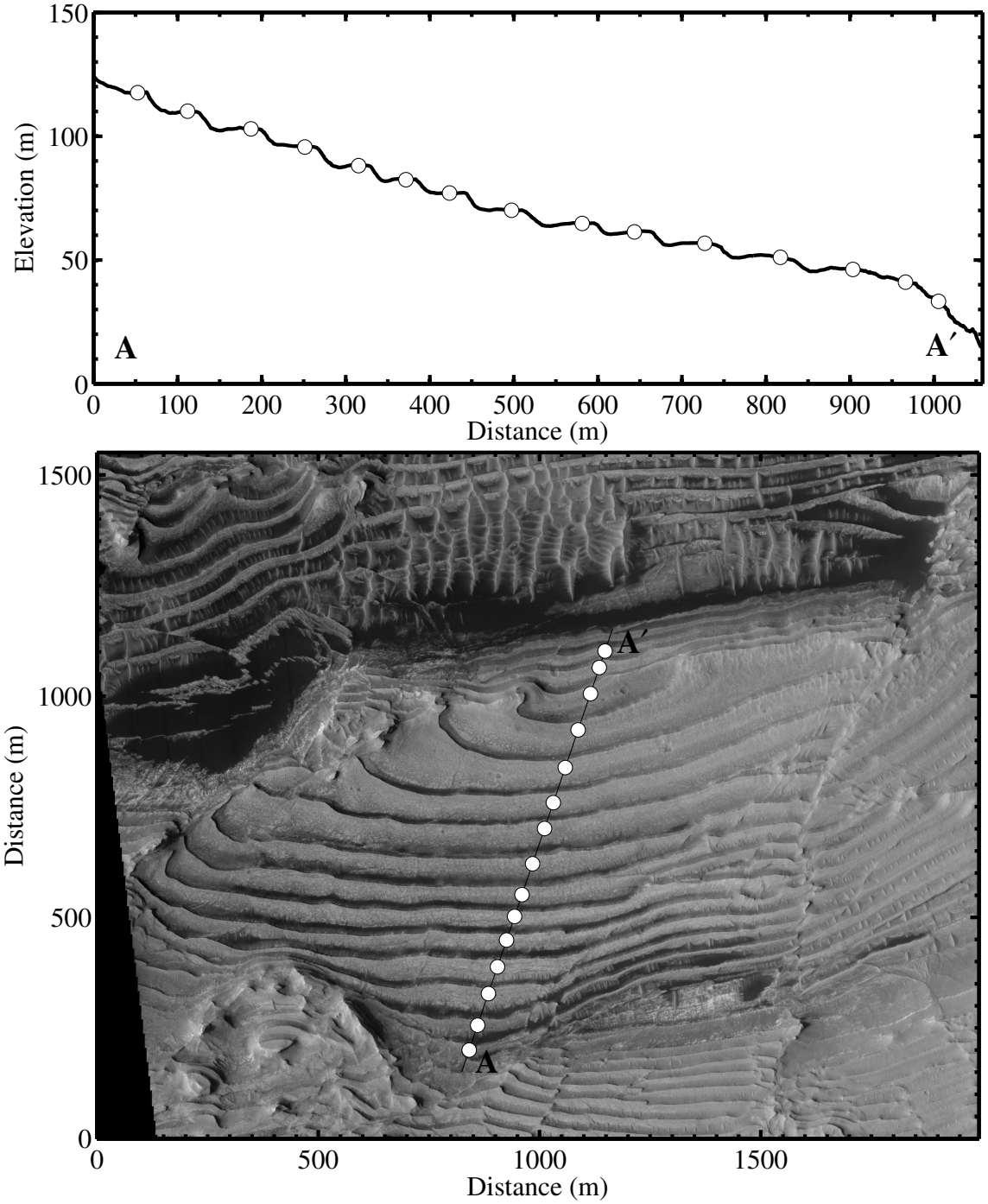

Figure 4.1: Topographic profile across one rhythmically bedded outcrop, showing that strata are well resolved in the stereo DTM. Although the beds have varying apparent thicknesses in the original images, the true thicknesses are quasiperiodic when the erosional topography and southward dip is properly accounted for. The lower panel is an orthogonal projection of HiRISE image PSP_002733_1880.

consider possible interpretations of these observed distributions below.

We have used spectral analysis of the stratigraphic records to further assess the periodicity of the bedding at these locations, described in detail in section 4.2.0.4. Both image grayscale values and DTM slope profiles provide a continuous record of the stratigraphy. In three of the four locations we analyzed the image brightness record, while at the 8° N, 359° E site, slope values provided a better record due to unfavorable lighting conditions. The data were sampled from the orthorectified images or DTM, and corrected for the structural dip and topography. To obtain a uniformly spaced record, the record was resampled in the stratigraphic reference frame to the mean spacing of the data (∼0.1 m in all four cases). We derived spectral estimates via the multi-taper method of *Mann and Lees* (1996), which were then assessed relative to a first-order autoregressive (red noise) background. We utilized the robust estimation technique of *Mann and Lees* (1996) to model the red noise component of the data, and derive corresponding confidence levels. Spectral peaks exceeding these thresholds indicate that a quasiperiodic component is non-random with the specified confidence. The spectra showed peaks which exceeded the 99% confidence levels at the measured bedding scales for all sites except Crommelin crater, where the excess power only surpassed the 95% threshold. In the Becquerel spectrum, power exceeded the 99% confidence level relative to the estimated background at both 3–4 and at 30–40 meters, demonstrating statistically significant quasiperiodicity in the Becquerel stratigraphy at both scales (Figure 4.2).

4.3.5 Interpretations

The observation of rhythmic layering on Mars at multiple locations across the Arabia region is evidence of cyclic variations in ancient surface conditions. The different scales measured, along with the varying morphologies observed between sites and the dearth of similar deposits on the intervening plains in Arabia (*Edgett and Malin*, 2002), suggests that these deposits formed in isolation, rather than as part of a regionally extensive sedimentary unit. Still, the presence of several regularly cyclic sequences within this region of Mars hints at a common external driver, with the local conditions of each sedimentary basin influencing the expression of climate cycles in the stratigraphy.

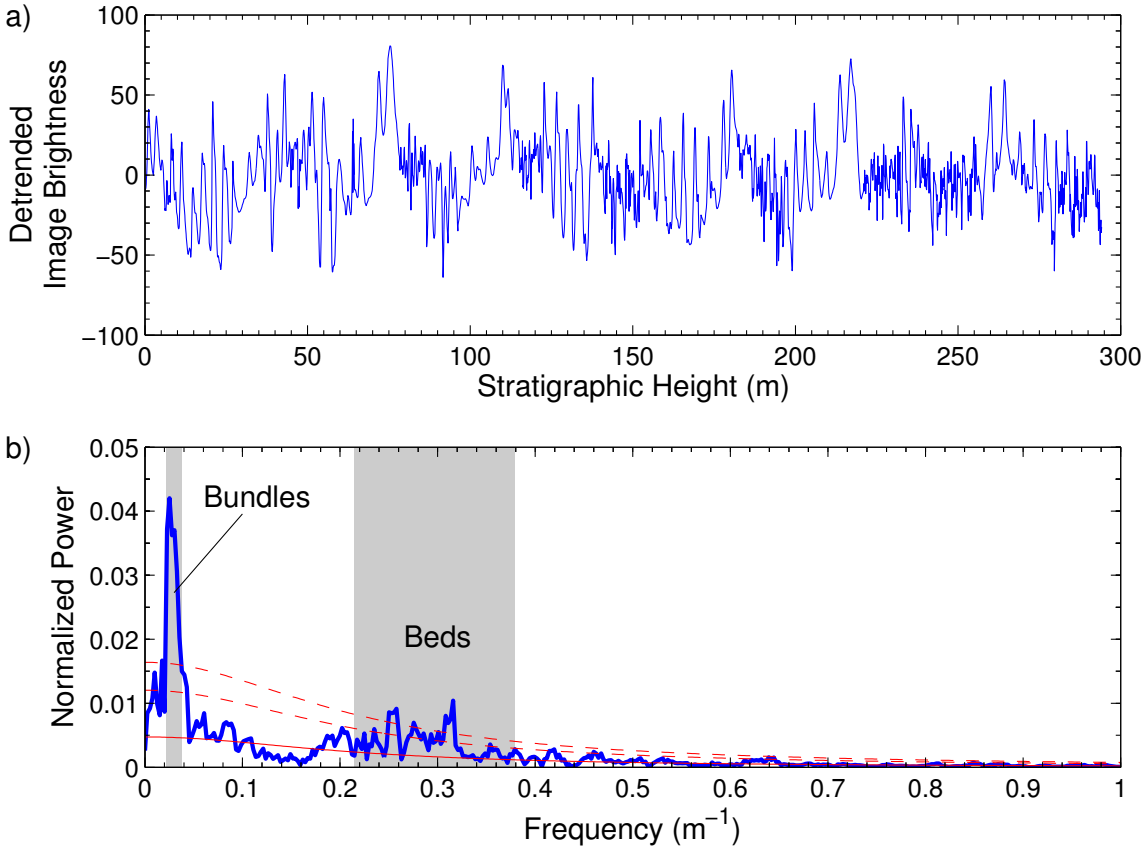

Figure 4.2: A. Detrended image grayscale levels of the Becquerel crater outcrop, topographically corrected and resampled at a uniform interval of 0.1 m in the stratigraphic column. B. Power spectrum of the Becquerel crater stratigraphy. Estimated red noise background (red, solid) along with 95% and 99% confidence levels (red, dashed) are indicated. Shaded regions indicate the 1σ range of bed and bundle thickness measurements, and correspond well to the two regions where power exceeds the 99% confidence level, indicating quasiperiodicity at both scales.

From orbit, it is difficult to determine the nature of the prominent bed boundaries which lead to the alternating pattern of erosional resistance. Each erosional step may record discrete or continuous changes in the bulk composition or lithification history of the sediments, overlain on a steady background sedimentation rate. Alternatively, the deposition rate may have varied over each cycle, with episodes of relatively low accumulation leading to more complete induration of the sediment. In either case, quasiperiodic bedding will result when the sediment accumulation rate is roughly constant when averaged over each cycle. With either model, the observed periodicity in stratigraphic position represents a record of cyclicity in time.

An alternative depositional model is that each bed was laid down by discrete, aperiodic events of similar magnitude. This is seen, for example, on Earth in the flood deposits of glacial Lake Missoula, where outbursts of comparable magnitude created repeating beds of similar thickness (*Waitt Jr.*, 1980). Two observations argue against this possibility in Arabia Terra. First, the bundling of strata into repeating packages seen in Becquerel crater would require an unlikely additional level of incidental cyclicity. Second, the apparent lack of coarse sediment, channel incision or erosional unconformities argues against fluvial emplacement of these several-meter-thick beds. Emplacement of a bed in this scenario must occur in a single depositional event to be timescale independent. This requirement likely rules out formation by individual dust storms, for instance, as current dust deposition rates are on the order of only microns per year (*Landis and Jenkins*, 2000). It is impossible to rule out any scenario without knowing the precise relationship between time and depth. However, we find this case improbable given the bundling seen at Becquerel crater, the volumes of sediment required, and the lack of evidence for aqueous deposition.

The nature of the sedimentation process which deposited the Arabia layers remains uncertain. However, the observation of regularly cyclic bedding rules out processes that occur in a purely stochastic manner, including volcanism and impact cratering. Such events recorded at random intervals within a stratigraphic column are expected to result in an exponential distribution of intervals (*Wilkinson et al.*, 1998). Further, the size-frequency distributions of many stochastic depositional processes are skewed toward smaller events, and can be described in many cases by a

power law. Such processes including turbidites, flood events, landslides, volcanic eruptions and impacts (*Carlson and Grotzinger*, 2001; *Malamud and Turcotte*, 2006, and references therein). As both power law and exponential distributions may be statistically rejected for several of the Arabia sites, a stochastic process of this nature is unlikely, without forcing by environmental cyclicity.

On Earth, periodic stratification in the rock record is often associated with cyclic driving mechanisms, which influence the deposition and preservation of sediments. Tidal, seasonal, solar, and orbital cycles have all been documented in sedimentary records (*Fischer*, 1986; *House*, 1995; *Weedon*, 2003). Quasiperiodic climate cycles on Earth can also arise from internal atmospheric, ocean, and ice sheet dynamics, without an obvious external forcing function (*Weedon*, 2003). On Mars, the likelihood of such internally generated cycles is diminished in the absence of oceans, wet-based ice sheets, and biological feedbacks (*Kieffer and Zent*, 1992). Martian global dust storms may be quasiperiodic, although at shorter, interannual timescales (*Kahn et al.*, 1992).

In analogy to the Earth, the strongest periodic signals on Mars arise at diurnal, annual, and orbital frequencies, all of which cause large variations in local surface conditions. As on Earth, these cyclic forcing mechanisms are dominant at periods shorter than ∼10 years and longer than a few tens of thousands of years (*House*, 1995). The thickness of the beds in Arabia argues against deposition on diurnal or annual timescales. Annual accumulation of over ten meters of sediment would represent an extremely high deposition rate, and would imply the kilometer-thick deposits accumulated in as little as tens of years. In contrast, deposition at orbital frequencies (∼100,000 years) assumes a modest average accumulation rate of ∼100 μm per year. This value allows for alternating accumulation and erosion of sediment on shorter timescales, requiring only that the net deposition is roughly constant over long timescales.

Bundling within rhythmic sequences has been a useful indicator of Milankovitch forcing on Earth. In particular, the 5:1 frequency ratio of the precession to eccentricity cycles for the Earth has been observed in the rock record (*House*, 1995; *Schwarzacher*, 2000). A hierarchy of this type can be used not only to confirm the influence of a periodic forcing mechanism, but also to translate stratigraphic cycles to relative timescales (*Hinnov*, 2000). At Becquerel crater (Figure 4.3) we observe a roughly

10:1 ratio of frequencies over several hundred meters of section, for a total of at least 10 bundles. Individual beds here have a mean thickness of 3.6 ± 1 m, and the bundles are 36 ± 9 m thick. Strata are less distinct near the bottom of each bundle, making it difficult to obtain a precise count for each cycle.

The obliquity of Mars has the largest effect on the global climate, and has been most often discussed as a driver for climate change (*Ward et al.*, 1974; *Christensen and Moore*, 1992; *Kieffer and Zent*, 1992; *Head et al.*, 2003). The tilt of the planet's spin axis ranges over tens of degrees, and can have a strong effect on climate, changing the mean annual insolation even at low latitudes by 10% or more, and affecting the global distribution of volatiles. Among the leading effects, polar condensation of carbon dioxide is expected to reduce atmospheric pressure at low obliquity (*Fanale and Salvail*, 1994). For an aeolian depositional scenario, reduced pressure limits the capacity of the atmosphere to transport sediment (*Cutts and Lewis*, 1982). The obliquity of Mars oscillates with a period of ∼120,000 years, and is modulated on a timescale of ∼1.2 and ∼2.4 Ma (*Ward*, 1992; *Laskar et al.*, 2004). Orbital calculations show that this modulation is expressed more strongly at 2.4 Ma for the recent history of Mars, although the ancient history is unknown due to the chaotic nature of the obliquity over long timescales (*Touma and Wisdom*, 1993). As absolute frequencies of these orbital cycles will not vary significantly over geologic timescales (*Laskar et al.*, 2004), this 10:1 ratio in the obliquity cycle is a potential candidate for orbital forcing of the cyclic stratigraphy measured at Becquerel crater. This would imply a formation of one bed per 120,000-year obliquity cycle, one bundle per 1.2 Ma modulation cycle, and deposition of the entire measured section over roughly 12 Ma.

The identification of quasiperiodic signals within these layered terrains provides a possible relative chronometer within the Martian rock record. Orbital variations stand out as a possible driver of the observed quasiperiodicity, although definitive identification of the cycles involved will require additional information. Likewise, while an aeolian scenario provides a clear link to orbital forcing, the specific formation model remains uncertain. Determination of formation timescales ultimately provides a calibration for interpreting the geological history of Mars. With the tentative, but rea-

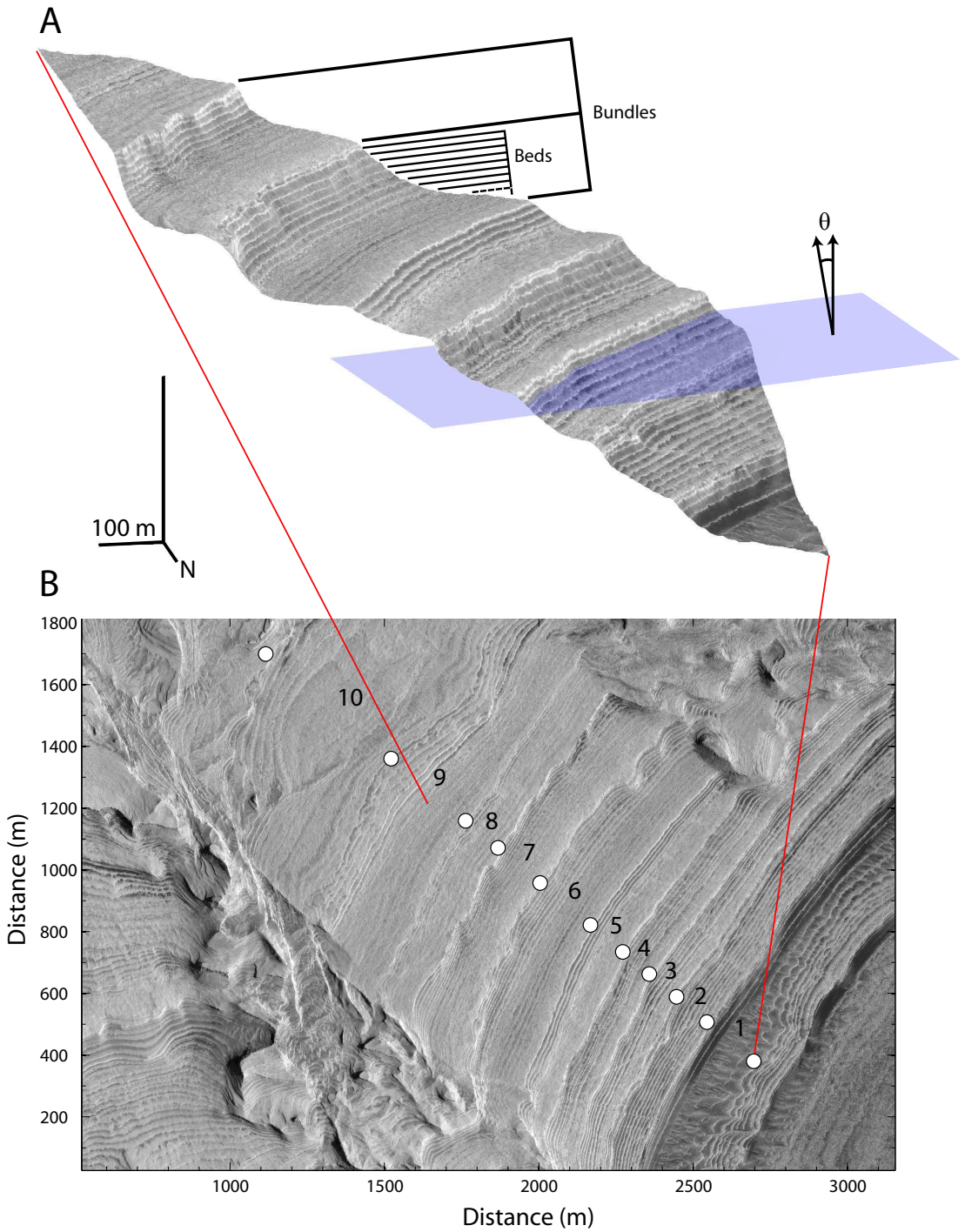

Figure 4.3: A. Three-dimensional view of the stratified deposit within Becquerel crater. This location shows two scales of quasiperiodic bedding, marked as beds and bundles. The ratio of these characteristic thicknesses is a potential clue to the forcing mechanisms responsible for the cyclicity seen in the rocks. The blue plane indicates the best fit orientation of the bedding, which has a dip of ∼3 degrees. To obtain true thicknesses, both the erosional morphology and the tilt of the bedding from horizontal (indicated by θ) must be accounted for. HiRISE image PSP_001546_2015 is shown draped over digital stereo topography. Scale bars indicate 100 m in both the horizontal and vertical directions. B. Plan view of HiRISE image PSP_001546_2015, showing context for A; north is down. Numbers mark the boundaries between successive bundles as revealed in the topography.

sonable assumption that some water was required to lithify the Arabia deposits, the suggestion of orbital cyclicity implies that a hydrologic cycle may have been active at least intermittently over millions of years. In contrast to the catastrophic surface conditions inferred from impact craters and outflow channels, this strong cyclicity observed in the Martian rock record depicts a fundamentally more predictable and regular environment in the ancient past.

Acknowledgements

This work was conducted with support from NASA's Mars Data Analysis Program, as well as the NASA Earth and Space Science Fellowship program. We are grateful to two anonymous reviewers for helpful comments and suggestions.

Crater Name	Location	N	Mean Thickness (m)	σ (m)
Becquerel (Beds)	22° N, 352° E	66	3.6	1.0
Becquerel (Bundles)	22° N, 352° E	10	35.5	9.2
Crommelin	5° N, 350° E	8	19.6	4.0
Unnamed	8° N, 353° E	14	9.7	1.5
Unnamed	9° N, 359° E	10	12.6	2.6

Table 4.1: Locations and bed thickness distributions measured from HiRISE stereo topographic data at four outcrops in the Arabia Terra region of Mars.

HiRISE Stereo Images

Crater Name	Location	Left Image	Right Image
Becquerel	22° N, 352° E	PSP_001546_2015	PSP_001955_2015
Crommelin	5° N, 350° E	PSP_003432_1850	PSP_005766_1850
Unnamed	8° N, 353° E	PSP_002733_1880	PSP_002878_1880
Unnamed	8° N, 359° E	PSP_001902_1890	PSP_002047_1890

Table 4.2: HiRISE images used for stereo analysis at each location in Arabia Terra

Becquerel Beds

Number	X (m)	Y (m)	Z (m)	Thickness (m)
1	0.0	0.0	-3383.6	3.4
2	22.4	6.2	-3381.5	2.8
3	28.9	0.1	-3378.8	3.4
4	39.5	-4.4	-3375.0	3.3
5	48.2	-9.8	-3372.1	3.2
6	55.4	-18.6	-3370.3	3.4
7	65.3	-24.5	-3367.0	3.7
8	73.2	-31.7	-3363.8	3.8
9	85.8	-18.4	-3360.1	2.7
10	85.3	-28.0	-3357.1	2.4
11	87.6	-34.9	-3354.6	2.7
12	92.5	-33.9	-3353.2	4.0
13	142.0	-48.6	-3343.9	4.3
14	152.3	-57.0	-3340.5	4.8
15	165.8	-60.0	-3336.1	4.1
16	172.3	-64.9	-3332.9	3.4
17	179.4	-72.6	-3329.1	4.1
18	186.8	-74.8	-3325.1	4.6
19	251.3	-100.7	-3311.8	3.0
20	259.1	-103.0	-3308.9	4.2
21	268.7	-107.2	-3305.1	5.7
22	281.3	-109.8	-3299.4	4.7
23	299.4	-96.9	-3295.8	4.8
24	310.1	-100.5	-3291.2	4.1
25	383.4	-89.2	-3279.6	2.0
26	386.1	-98.8	-3278.4	2.2
27	386.5	-112.2	-3276.7	3.2
28	398.6	-115.5	-3273.8	3.6
29	410.1	-122.5	-3270.9	4.2
30	483.9	-355.8	-3264.7	3.1
31	487.8	-379.5	-3262.5	3.6
32	491.9	-402.0	-3260.5	3.6
33	503.9	-404.1	-3256.9	3.2
34	505.6	-417.1	-3254.4	4.0
35	505.5	-436.4	-3250.6	4.2

Becquerel Beds (cont.)

Number	X (m)	Y (m)	Z (m)	Thickness (m)
36	512.9	-436.0	-3246.6	4.4
37	519.5	-444.5	-3243.5	2.9
38	652.0	-499.5	-3227.0	3.2
39	663.5	-502.7	-3224.3	3.2
40	666.7	-512.2	-3222.2	4.1
41	671.6	-519.5	-3219.5	3.7
42	682.2	-519.9	-3215.8	6.5
43	754.0	-629.0	-3203.9	2.1
44	770.7	-619.3	-3201.5	1.6
45	768.6	-657.7	-3202.1	2.6
46	938.9	-779.1	-3186.1	4.9
47	945.7	-811.8	-3182.8	3.3
48	933.6	-863.1	-3181.4	4.1
49	954.6	-883.9	-3178.6	4.1
50	990.0	-888.4	-3175.4	2.6
51	1256.9	-1174.9	-3172.5	4.1
52	1280.7	-1184.8	-3169.9	5.1
53	1306.5	-1185.6	-3165.1	6.6
54	1325.6	-1206.3	-3160.1	6.5
55	1382.6	-1119.1	-3150.6	2.5
56	1399.9	-1138.5	-3149.0	3.1
57	1411.8	-1142.6	-3146.6	3.2
58	1529.7	-1186.0	-3136.2	3.7
59	1555.1	-1184.4	-3131.9	3.2
60	1563.6	-1209.3	-3129.3	3.1
61	1578.0	-1211.2	-3126.2	3.2
62	1589.5	-1210.3	-3121.3	3.0
63	1607.0	-1206.8	-3118.1	2.9
64	1614.4	-1213.3	-3115.3	3.6
65	1616.5	-1225.4	-3111.8	3.4
66	1618.2	-1235.3	-3107.9	2.3

Table 4.3: Bed locations and thicknesses measured from HiRISE stereo topographic data at Becquerel crater

Becquerel Bundles

Number	X (m)	Y (m)	Z (m)	Thickness (m)
1	0.0	0.0	-3385.6	31.4
2	62.5	-88.5	-3359.1	40.6
3	182.5	-142.5	-3323.6	36.7
4	254.0	-233.3	-3294.1	25.2
5	376.5	-314.8	-3274.5	44.1
6	496.5	-547.2	-3243.2	36.6
7	633.8	-630.4	-3215.6	18.6
8	725.8	-754.9	-3204.3	40.9
9	998.5	-933.6	-3178.2	49.7
10	1380.6	-1250.1	-3150.9	31.3

Table 4.4: Bundle locations and thicknesses measured from HiRISE stereo topographic data at Becquerel crater

Crommelin Beds

Number	X (m)	Y (m)	Z (m)	Thickness (m)
1	0.0	0.0	-3111.7	21.0
2	-59.4	-40.0	-3107.9	26.4
3	-172.8	-53.8	-3100.0	19.3
4	-264.0	-112.3	-3098.6	16.7
5	-439.2	-89.9	-3110.0	13.1
6	-574.7	-53.3	-3114.8	19.4
7	-672.1	-105.2	-3113.5	22.6
8	-868.1	-109.6	-3129.1	18.2

Table 4.5: Bed locations and thicknesses measured from HiRISE stereo topographic data at Crommelin crater

8° N, 353° E Beds

Number	X (m)	Y (m)	Z (m)	Thickness (m)
1	0.0	0.0	-3216.0	11.2
2	5.1	-33.3	-3208.8	6.5
3	16.0	-74.6	-3203.6	9.4
4	-8.9	-166.2	-3199.2	10.0
5	-68.1	-259.1	-3193.2	9.7
6	9.5	-323.2	-3186.4	7.2
7	-59.8	-393.8	-3183.6	9.7
8	-157.4	-478.3	-3180.0	10.5
9	-228.2	-548.8	-3174.0	8.4
10	-235.2	-595.0	-3168.5	9.5
11	-262.2	-648.0	-3161.9	10.5
12	-242.7	-710.8	-3154.5	10.6
13	-256.7	-771.6	-3146.9	12.5
14	-291.6	-841.6	-3139.2	9.6

Table 4.6: Bed locations and thicknesses measured from HiRISE stereo topographic data at an unnamed crater located at 8° N, 353° E

9° N, 359° E Beds

Number	X (m)	Y (m)	Z (m)	Thickness (m)
1	0.0	0.0	-2551.7	10.1
2	8.8	73.1	-2533.7	13.1
3	16.7	126.1	-2516.1	11.8
4	55.2	145.2	-2504.2	9.6
5	109.8	168.6	-2489.6	9.7
6	106.9	200.5	-2477.3	14.3
7	109.7	248.1	-2458.9	14.5
8	87.2	302.3	-2440.0	12.8
9	144.6	334.4	-2423.4	17.8
10	159.3	391.5	-2397.1	12.1

Table 4.7: Bed locations and thicknesses measured from HiRISE stereo topographic data at an unnamed crater located at 9° N, 359° E

4.4 Global Distribution and Geological Setting of Rhythmic Sedimentary Rocks on Mars

4.4.1 Introduction

While sedimentary rocks are exposed throughout the low latitudes of the planet Mars, many questions remain about their genesis and evolution. On Earth, considerable scientific progress evolved from the recognition of biostratigraphic markers, which allowed the correlation of distant rock formations (*Prothero and Schwab*, 2004). On Mars, the sedimentary rock record has been studied solely from remote sensing, with the exception of the two Mars Exploration Rover landing sites (e.g., *Grotzinger et al.*, 2005; *Squyres et al.*, 2007). From orbital data alone, it has been difficult to identify analogous stratigraphic markers for correlating distant sections. Spatial proximity of multiple sedimentary deposits (such as those in Valles Marineris or Arabia Terra) hints at a genetic link, but firmer evidence has remained elusive. *Lewis et al.* (2008a) utilized digital topographic maps derived from HiRISE stereo images to reconstruct true stratigraphic records of image brightness and topographic slope, under the assumption that these parameters are proxies for lithologic variation. As a result, several sections were found to contain quasiperiodic bedding of highly regular thickness. Here, we examine the stratigraphy in these locations in more detail, and examine potentially correlative sedimentary deposits for which stereo coverage is not yet available. In addition, we present analysis of several additional sites outside of Arabia Terra, some of which exhibit a distinct periodic signal.

A central outstanding question regarding the sedimentary rocks of Mars is the relevent timescale for deposition. Since the rocks represent a record of the planet's ancient climate conditions, which are thought to vary greatly through time, it is propitious to know what fraction of its history they document. The same question has provoked reseach into the polar caps of Mars, whose absolute age could constrain climate models of Mars' recent (1–10 Ma) history. Several authors have searched for periodic signals within the stratigraphy of the ice, in an attempt to find a link to specific climate forcing cycles (*Milkovich and Head*, 2005; *Laskar et al.*, 2002; *Perron and Huybers*, 2009). Thus far,

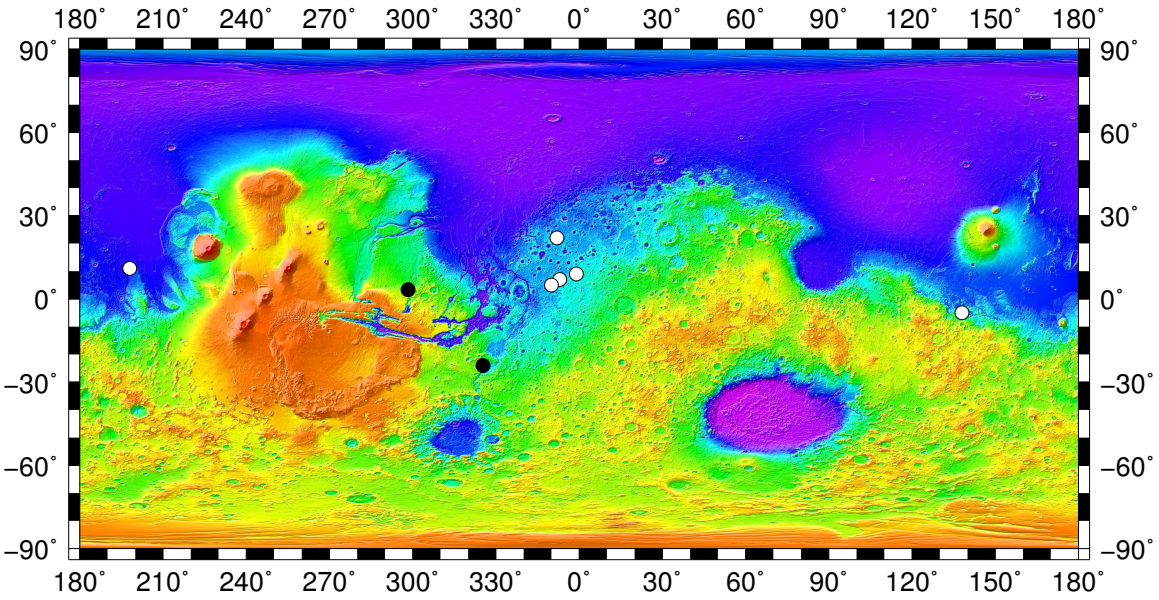

Figure 4.4: Map of the sections selected for this study. White circles indicate sections where quasiperiodic bedding is detected. Four of these are clustered in western Arabia Terra, while distant occurrences are found within Gale crater and an outcrop of the Medusa Fossae formation. Black circles mark two representative sections where non-periodic strata are observed, within Juventae Chasma and Eberswalde crater, which are described as contrasting examples.

conclusive correlations to the planet's insolation history have remained elusive.

Milkovich et al. (2008) reported briefly on the possibility of cyclic stratigraphy within Juventae Chasma using HRSC stereo topography. However, the possible detection of cross-bedding by *Komatsu et al.* (2004) makes the interpretation less clear. *Lewis et al.* (2008a) summarized the discovery of cyclic bedding within the rock record at Arabia Terra, also described in section 4.3.5. Here, we expand upon this work, extending our survey outside of the Arabia Terra region (Figure 4.4). We have identified quasiperiodic bedding at two new locations, at Gale crater and within the Medusa Fossae formation. In addition, we discuss in more depth the local geological setting of each of the sedimentary outcrops. Finally, we discuss the implications of the observation of globally distributed rhythmic sedimentary rocks on Mars.

4.4.2 Structure and Stratigraphy of Western Arabia Sites

Each of the locations studied in Arabia, while being in the same general region of Mars, exhibits distinctive characteristics. The sedimentary deposits are all found within craters, which are likely

sites of preferential preservation. The craters are generally tens of kilometers in diameter, implying an original depth of several kilometers. These intracrater deposits are concentrated in western Arabia Terra below ∼10° latitude with the exception of Becquerel Crater, which is located at 22° N. Outcrops generally have higher thermal inertia than the surrounding plains indicating a degree of lithification, generally ranging from 250 to 700 $Jm^{-2}K^{-1}s^{-1/2}$, as derived from the Thermal Emission Spectrometer (TES) instrument (*Christensen et al.*, 2001). These values are slightly higher than that found for the "White Rock" deposit in Pollack crater, although still well below that expected for continuously exposed bedrock (*Ruff et al.*, 2001).

4.4.2.1 Unnamed 8° N, 353° E crater

An unnamed 60 km diameter crater at 8° N, 353° E holds some of the most extensive, and most periodic, bedding in the Arabia region. This crater has been discussed in a number of studies since the discovery of its stratigraphy from MOC images (*Malin and Edgett*, 2000; *Edgett and Malin*, 2002; *Edgett*, 2002), although little is known about its origin. The stratified materials span the entire floor of the crater without exposing the underlying substrate. Although the highest strata are found high on the walls of the crater, they appear to be constrained to a few hundred meters below the rim. The total elevation range of the interior deposits is greater than 1300 m (roughly −3200 to −1900 m). The true thickness of the exposed stratigraphy is difficult to estimate, due to structural deformation. The presence of steeply dipping sections and an extensive network of faults hinder the correlation of adjacent sections, preventing a full reconstruction. Several largely intact blocks were chosen for study at this location, lying near the lowest part of the crater at roughly −3200 m elevation.

The area for which HiRISE stereo coverage was available is located in the northwestern part of the crater, which contains some of the most well-expressed bedding. Hundreds of beds appear to be exposed across the floor and walls of the crater. However, several major northwest trending faults permeate the stratigraphy, along with a large number of smaller faults trending in all directions. The largest faults can be followed over several kilometers, and appear to have caused large displacements,

as the bedding often cannot be followed across a major fault. In most cases, the rhythmic nature of the bedding hinders the correlation of distinctive strata between sections. However, one particularly dark bed can be follwed across several nearby faulted blocks. Four stratigraphic sections were extracted acrosss the HiRISE image pair to evaluate their intercorrelation. Figure 4.5a shows the locations of each of the sections within the HiRISE base image. The positions of twelve beds common to all of the sections were measured (from which eleven thicknesses can be calculated), along with the bedding attitudes for each location. In each case, the outcrop orientation was determined to be nearly identical, dipping at 11°–12° toward the south. The resulting bed thicknesses are shown in Figure 4.5b. Similar trends can be seen from bed to bed between datasets, providing confidence that the proposed marker bed is a reliable stratigraphic feature. Since beds positions are averaged from a set of x, y, z values, errorbars representing 1-σ residuals are shown. These observations suggest that much of the stratigraphy in this crater represents repeated sections, and that the total stratigraphic record present is thinner than exposed outcrops appear to reveal. In addition, the correlation of these disconnected outcrops demonstrates that large (100 meter to kilometer scale) displacements have occured on major faults. Due to the fact that the slip vector is unknown, the relative contributions of strike-slip and dip-slip motion cannot be determined. Interestingly, the surprisingly similar bedding orientations between sections suggests that their dip was acquired prior to faulting, possibly as a result of being deposited against the northern crater wall.

Two sections were selected for spectral analysis. The first was chosen from one of the four correlated sections discussed above. The outcrop, shown in Figure 4.6a contains 16 beds averaging 10.4 ± 1.6 m in thickness. The corresponding image brightness record and power spectrum are shown in Figure 4.6b and c. The mean discrete bedding thickness is plotted with the spectrum in blue, and corresponds precisely to the dominant spectral peak. The second section, also described in section 4.3.5, is shown in Figure 4.7 and contains 14 beds at 9.7 ± 1.5 m thickness. Both peaks far surpass their respective 99% confidence levels relative to estimated red-noise backgrounds. The stratigraphic relationship of these two blocks is not known precisely, although the second block appears to be stratigraphically higher than the first. Thus, the constancy in bedding thickness

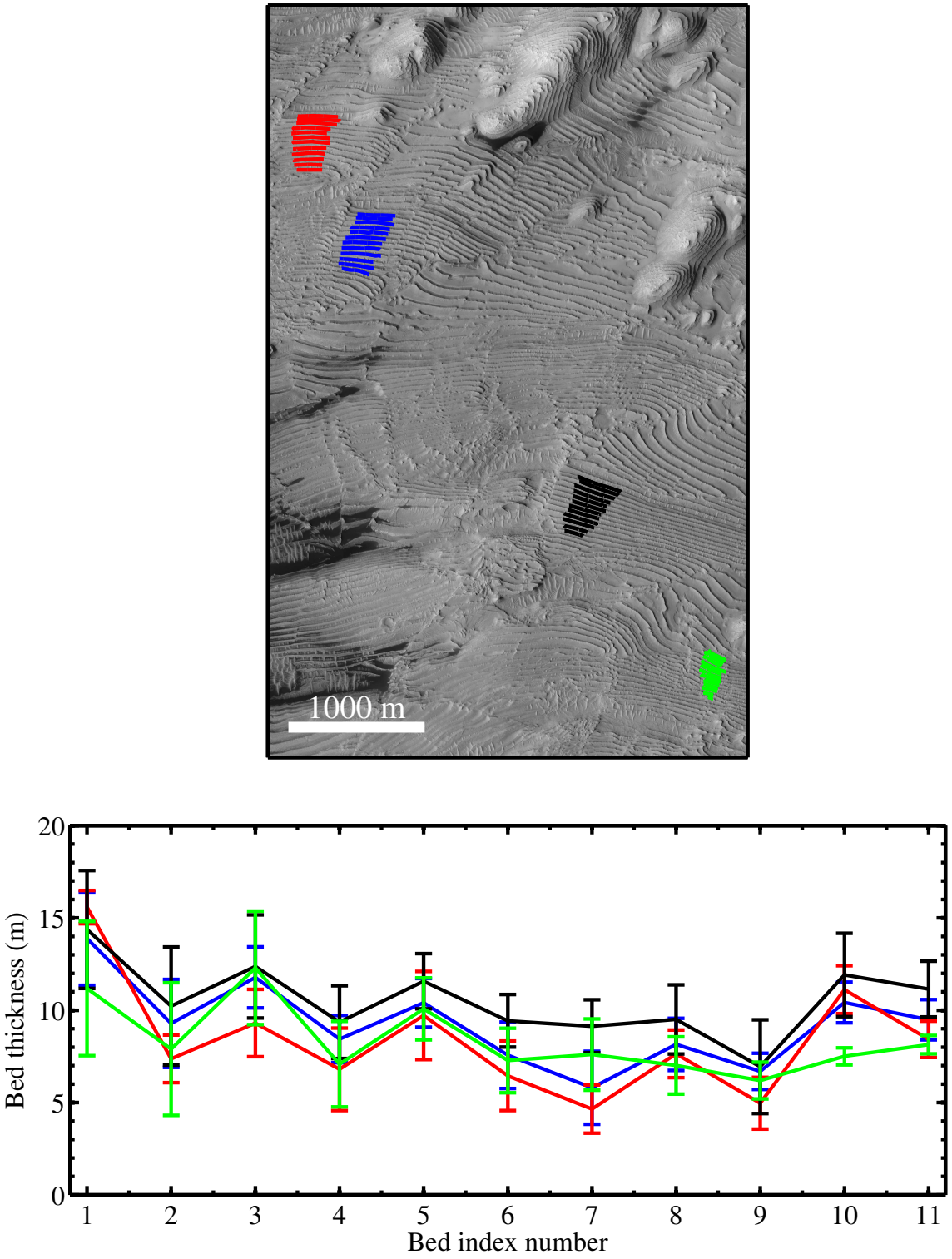

Figure 4.5: A. Locations of four stratigraphic sections in which a distinctive marker bed has been identified. B. Measured bed thicknesses for the four correlated sections. A similar sequence of thicknesses is observed in each of the locations, supporting the marker bed as a reliable tiepoint.

appears to be present over kilometer horizontal lengthscales, and over larger stratigraphic distances than in the single section described by *Lewis et al.* (2008a).

4.4.2.2 Unnamed 9° N, 359° E Crater

A second unnamed crater for which HiRISE stereo is available is located several hundred kilometers to the east. Within this 30 km diameter crater, sedimentary deposits are exposed around the walls of the crater, with prominent mesas scattered across the floor. In total, a few tens of beds are exposed, although erosion may have removed overlying strata. Mesas with simlar morphology are found in several nearby craters (e.g., those at 9° N,358° E; 8.8° N,358.2° E; and 11° N,355.5° E), suggesting a common genesis. However, the stratigraphy cannot be compared quantitatively, as HiRISE stereo data has not yet been acquired for these sites.

The HiRISE image pair used here (PSP_001902_1890/PSP_002047_1890) covers the central portion of the crater, with stratified hills to the north and south, and the substrate exposed at the center of the crater. A hill on the northern side offered the longest continuous record, shown in Figure 4.8a. Dips were found to be southward at rougly 5°. As in other locations, this is consistent with draping of the northern crater wall by the beds. In the southern part of the image, however, orientations are generally nearly horizontal. Here, the majority of several dozen beds measured have dips under 3°, with no preferential azimuth (Figure 4.9). As some of the scatter in the data is certainly due to measurement error, the stratigraphy in the southern portion of the crater is consistent with nearly horizontal deposition. In addition, the low dips indicate that the bedding in this crater has not been tectonically disrupted to the degree seen at other locations. This is also consistent with the lack of major faults observed within the crater.

The slope information in the DTM proved to be a more reliable stratigraphic record than the image brightness at this location. This is due mainly to the lighting conditions of the outcrop, which offered poor albedo contrast. The adjusted percent slope record is plotted in Figure 4.8b, and is dominated by a low frequency oscillation resulting from differential resistance of the beds to erosion. Figure 4.8c shows the corresponding power spectrum, with a clear peak centered at roughly 13 m

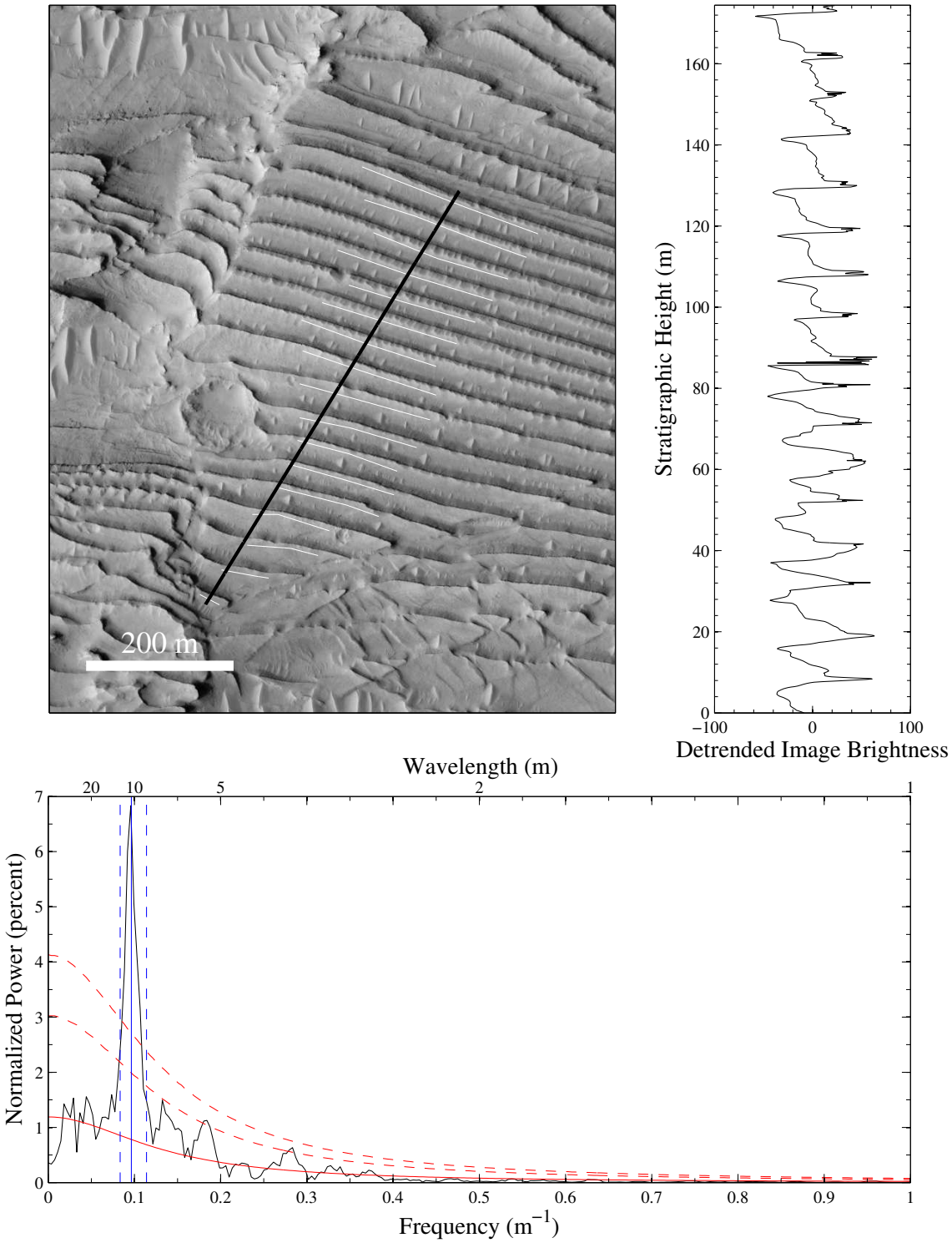

Figure 4.6: A. Location of one 8° N, 353° E crater outcrop. Black line marks the location of the extracted image brightness profile, with white lines showing the positions of individually measured beds. B. Stratigraphically adjusted and detrended image brightness record for 8° N, 353° E crater. C. Power spectrum of the 8° N, 353° E crater stratigraphy. Estimated red noise background (red, solid) along with 95% and 99% confidence levels (red, dashed) are indicated. Blue lines indicate the mean and 1-σ range of bed and bundle thickness measurements, corresponding well to the largest peak in the spectrum.

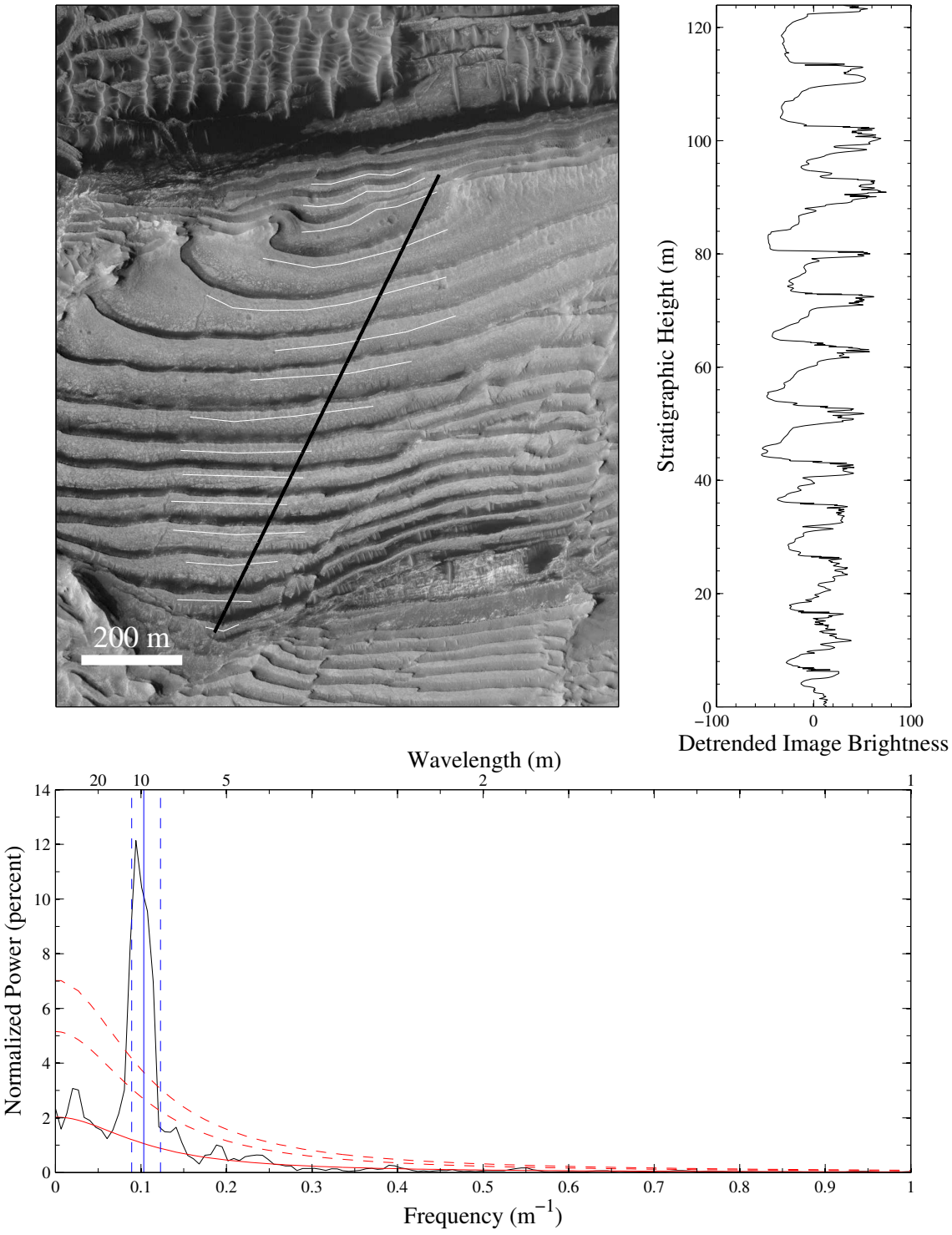

Figure 4.7: A. Location of the second 8° N, 353° E crater outcrop. Black line marks the location of the extracted image brightness profile, with white lines showing the positions of individually measured beds. B. Stratigraphically adjusted and detrended image brightness record for 8° N, 353° E crater. C. Power spectrum of the 8° N, 353° E crater stratigraphy. Estimated red noise background (red, solid) along with 95% and 99% confidence levels (red, dashed) are indicated. Blue lines indicate the mean and 1-σ range of bed and bundle thickness measurements, corresponding well to the largest peak in the spectrum.

surpassing the 99% confidence level. A second peak at 3 m is seen, and does not correspond to an obvious scale of variation in the images. As we used the slope record at this location, this may be an artifact of the DTM generation algorithm.

4.4.2.3 Crommelin

Crommelin crater, located at 5° N, 350° E, is the most equatorial of the Arabia sites described here, lying in the southwestern limit of Arabia Terra. The crater itself is roughly 110 km in diameter, and hosts a large central mound of stratified rock which covers the floor of the crater. The mound is over 2200 m in thickness, ranging from −3600 m at its lowest exposure to −1400 m at its peak. Interestingly, the unbreached crater rim is only as high as −1800 m in places, 400 m below the peak of the sedimentary mound. Immediately to the southeast, two additional craters are infilled with morphologically similar materials. Directly to the south, an 80 km diameter crater contains a similar ∼1700 m thick mound of sediment exposed from −3200 to −1500 m, similar to the elevation range of the Crommelin mound. Again, this mound is higher than the rim of its crater by as much as 300 m in places. Additionally, an unnamed 50 km crater to the southeast contains a ∼300 m high, less well-exposed sedimentary mound, which is fully constrained below the crater rim.

We analyzed one stratigraphic section situated near the base of the mound at −3100 m. This outcrop occurs on a 150 m high topographic ridge exposed on the eastern side of the crater floor. The strata exposed on the ridge are uniformly westward dipping at 5°–15°. This may reflect post-emplacement tilting, although the position of the outcrop on the eastern side of the crater could also be consistent with draping of the bedding against the crater wall.

As compared to the other sites in Arabia, bedding is relatively poorly expressed in this area of Crommelin crater. Strata tend to have scalloped edges which vary laterally in erosional resistance. Prominent beds are accentuated by the presence of dark aeolian sands which collect along topographic steps, nine of which have been identified within the exposed section. Each of these contain a larger number of poorly expressed sub-units; unfortunately, these sub-units are difficult to follow, and the strata are generally too thin to resolve in the DTM. For this reason, we focus on

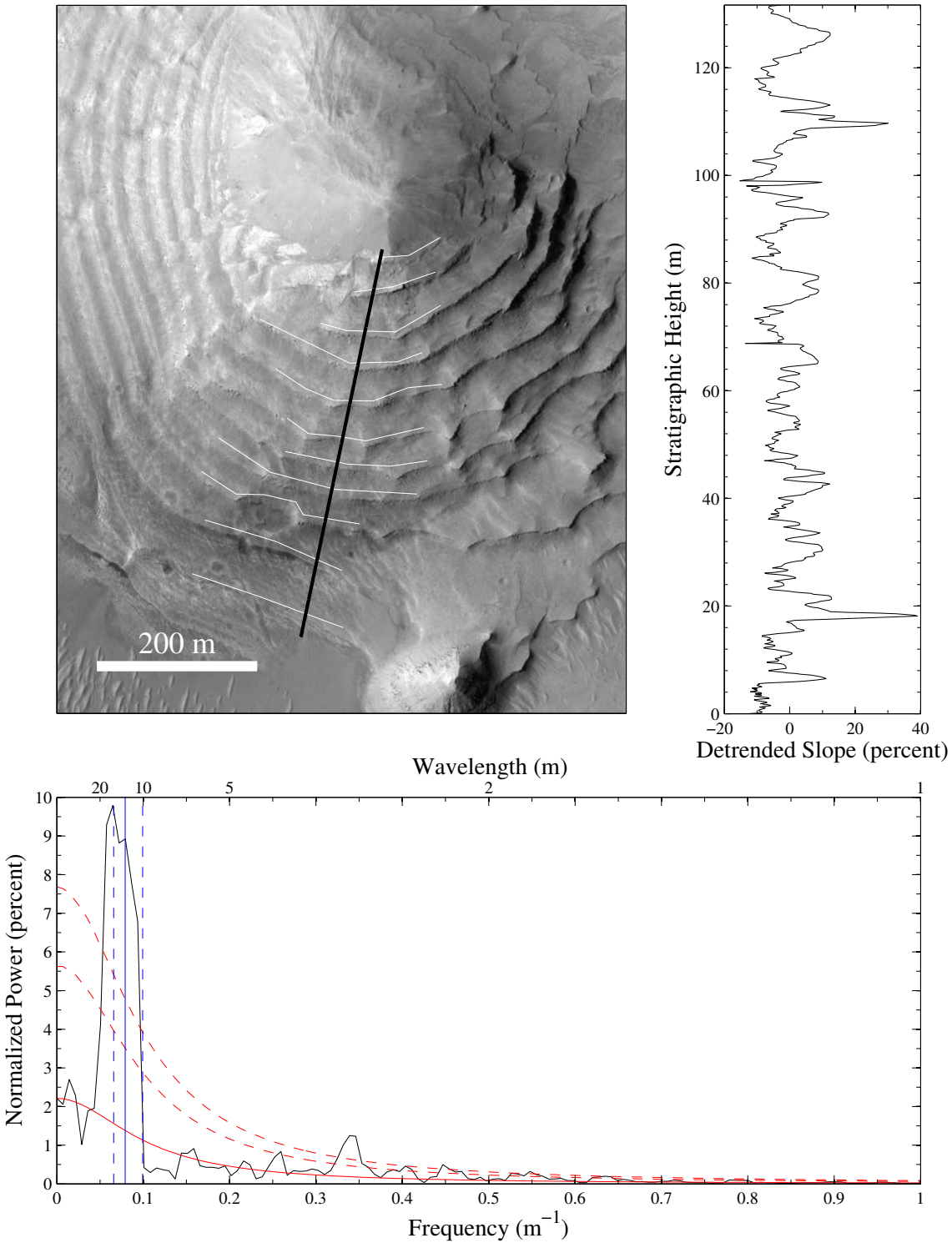

Figure 4.8: A. Location of 9° N, 359° E crater outcrop. Black line marks the location of the extracted image brightness profile, with white lines showing the positions of individually measured beds. B. Stratigraphically adjusted and detrended topographic slope record for 9° N, 359° E crater. C. Power spectrum of the 9° N, 359° E crater stratigraphy. Estimated red noise background (red, solid) along with 95% and 99% confidence levels (red, dashed) are indicated. Blue lines indicate the mean and 1-σ range of bed and bundle thickness measurements, corresponding well to the largest peak in the spectrum.

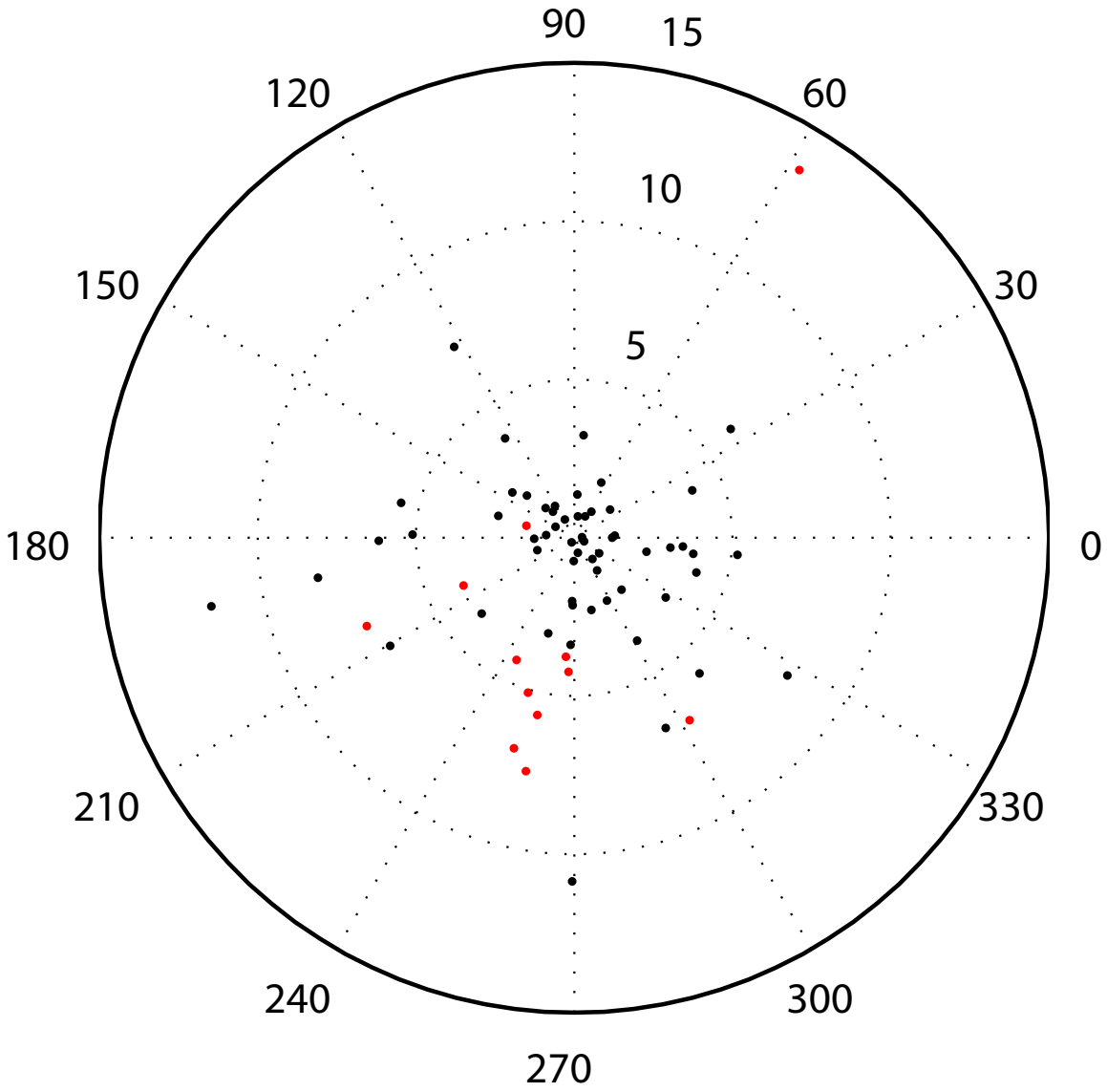

Figure 4.9: Dip and azimuth of 70 beds measured at the 9° N, 359° E crater. Strata on the northern side of the image (red) have southeastward dips of about 5°, on average. In contrast, outcrops in the southern half of the crater (black) tend to have low dips with no preferential orientation, consistent with nearly horizontal deposition.

the nine larger stratigraphic divisions. Figure 4.10a shows the location of the reconstructed section in black, with individual bedding measurements in white. Figure 4.10b shows the image brightness profile, with data adjusted to their true stratigraphic position. The Crommelin record has the most noise of all of the sections studied, as a result of a lower-quality topographic model. Obscuration by atmospheric dust in one of the HiRISE images is an impediment to precise image correlation. However, spectral analysis does detect a quasiperiodic signal at the scale of the beds, as discussed in section 4.3.4, and shown in Figure 4.10c. The normalized power spectrum is shown in black, with 50%, 95%, and 99% confidence levels shown in red. Blue lines mark the mean thickness and standard deviation of the discretely measured beds, closely corresponding to the largest spectral peak. Relative to an estimated red noise background, however, this peak only reaches the 95% confidence level.

4.4.3 Additional Sites

4.4.3.1 Gale Crater

Gale crater, one of the candidate landing sites of the Mars Science Laboratory rover, is a 170 km diameter crater located at 5° S, 138° E, far east of Arabia Terra. The crater is also filled with a large mound of sedimentary rock, possibly the thickest exposed at the surface of Mars today. The mound is more than 5 km thick, and hosts a diverse mineral assemblage transitioning from clay minerals at its base to sulfates higher in the stratigraphy (*Milliken et al.*, 2009). The top of the mound is mostly covered by a thick dust lag, resulting in an extremely low thermal inertia, and preventing specific mineral identification (*Pelkey et al.*, 2004). Unlike the other craters where cyclic bedding has been observed, the rim of Gale crater is breached by a large valley on its southern border. In addition, clear exidence of fluvial action is present as incised canyons sourced on the mound itself (*Cabrol et al.*, 1999). However, these features all occur in the lower portions of the mound. *Malin and Edgett* (2000) pointed out the presence of at least one major unconformity within the Gale stratigraphy, marked by a change in bedding attitude, and an interbedded crater at the stratigraphic contact which has been partially exhumed. The stratigraphy described here lies above

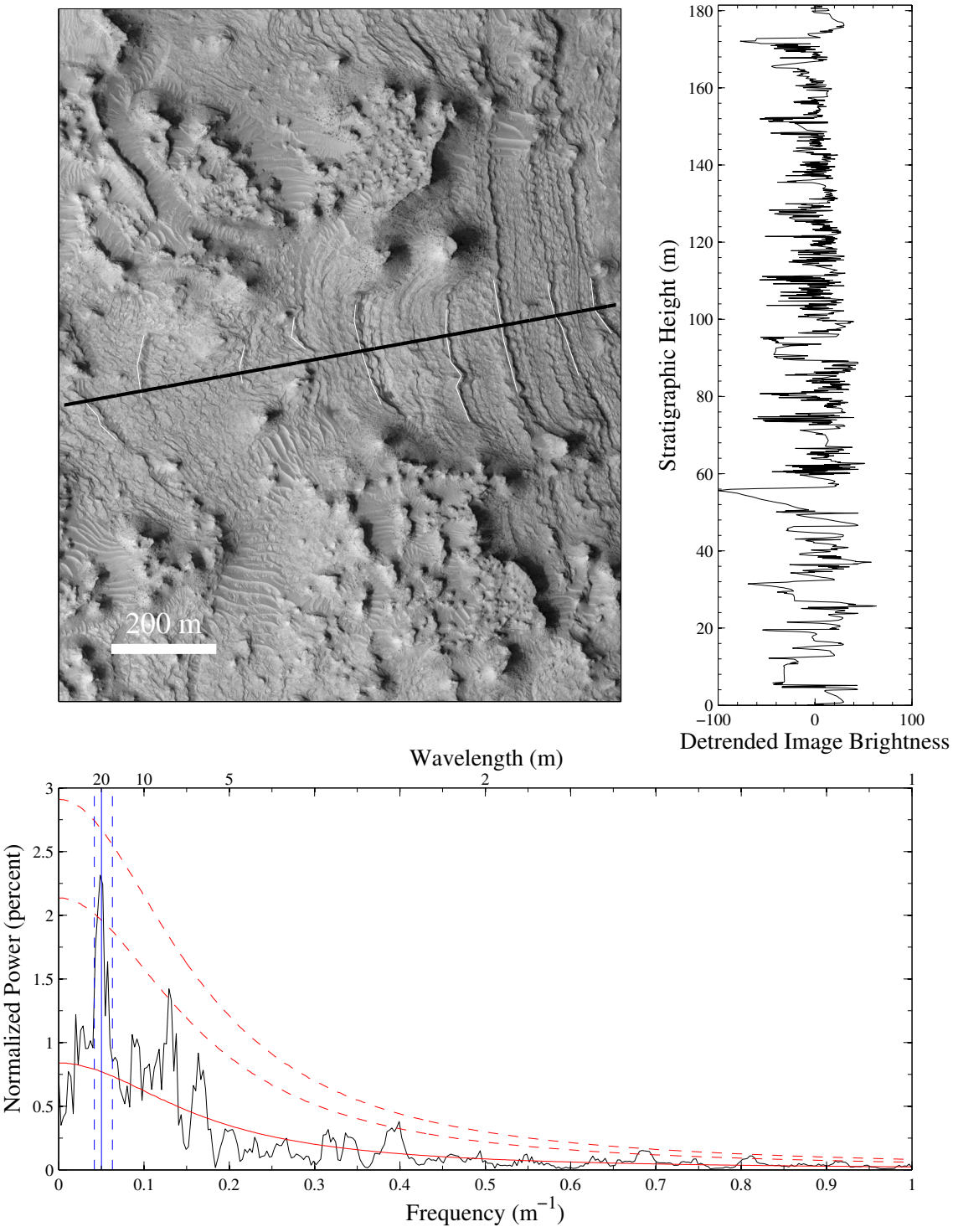

Figure 4.10: A. Location of Crommelin crater outcrop. Black line marks the location of the extracted image brightness profile, with white lines showing the positions of individually measured beds. B. Stratigraphically adjusted and detrended image brightness record for Crommelin crater. C. Power spectrum of the Crommelin crater stratigraphy. Estimated red noise background (red, solid) along with 95% and 99% confidence levels (red, dashed) are indicated. Blue lines indicate the mean and 1-σ range of bed and bundle thickness measurements, corresponding well to the largest peak in the spectrum.

this contact, likely postdating the fluvial activity. The bedding lies at ∼200 m elevation, fully 2.5 km above some sections of the northern rim of the crater, while still slightly below much of the southern rim. Given the location of Gale crater on the topographic dichotomy of the planet, the asymmetry of the rim is likely an original feature, rather than a sign of modification. The stratigraphy at the top of the mound likely formed above the rim, most importantly ruling out a lacustrine origin.

HiRISE stereo topography was derived from an image pair located near the summit of the Gale crater mound. This area features a large exposure of rock strata on the hanging wall block of a several kilometer-long normal fault. Strata dip steeply eastward toward the fault, at ∼29°. We avoided the area immediately adjacent to the fault, where the rocks have been folded into a synclinal structure. The total exposed stratigraphy in this area is several hundreds meters thick, although bedding is not continuously well expressed in any one location due to rough erosional topography. Unlike the craters found in Arabia Terra, the stratigraphy is not highlighted by the presence of dark sand. As a result, lighting conditions dominate the contrast of rock surfaces.

Figure 4.11 shows the stratigraphic section analyzed at the Gale crater summit. A 130 m long section was recovered in the uppermost portion of the stratigraphy, which shows a finer bedding scale than observed at most of the Arabia sites. Spectral analysis shows a concentration of power at ∼4.5 m, corresponding to roughly 25 beds. A low-frequency peak occurs at 30 m, but is likely related to a long-term variation in the outcrop slope brightness (or topographic slope) rather than cyclic variations. Three additional peaks barely reach the 99% confidence level in this spectrum. The first, at 3.1 m could correspond to real bedding variations, being within the range of discrete thicknesses measured. The second and third peaks at ∼1.7 m have a higher frequency than any bedding observed, and do not correspond to an obvious scale of periodic variation in the rocks.

4.4.3.2 Medusa Fossae Formation

The thick, wind-sculpted landforms of the Medusa Fossae formation have long been a geologic puzzle on Mars (*Schultz*, 2007). Outcrops of this unit drape extensive areas along the dichotomy boundary west of Tharsis. Individual deposits are kilometers thick, and appear to be middle to late

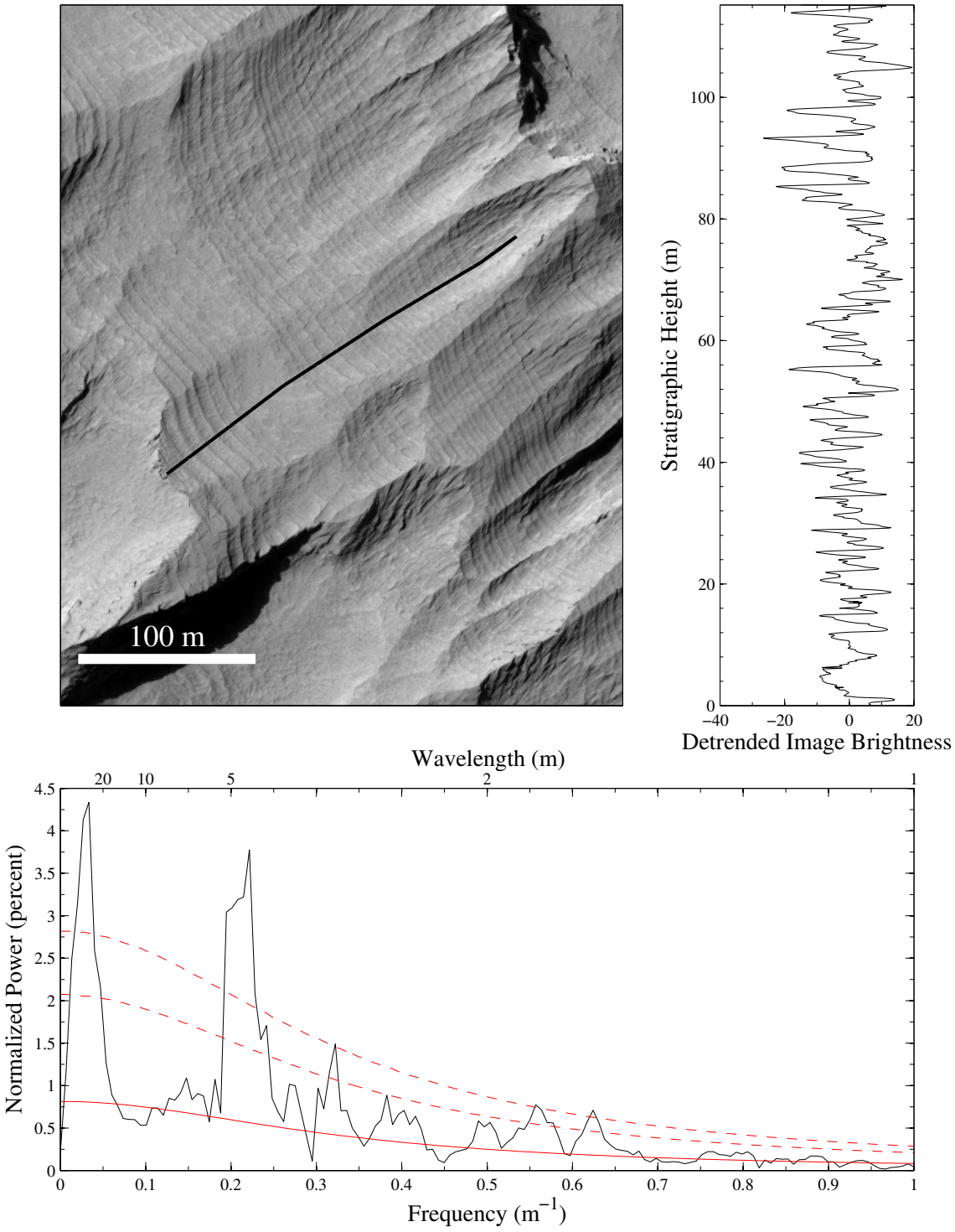

Figure 4.11: Stratigrapy exposed at the summit of the Gale crater stratified mound, as in Figure 4.6. Stereo image pair: PSP_008002_1750/PSP_009927_1750

Amazonian in age (*Scott and Tanaka*, 1986). Theories for the origin of the Medusa Fossae formation include pyroclastic ash falls (*Edgett et al.*, 1997) or accumulations of ice and dust. Anomalously low Earth-based 3.5 cm radar returns from this region initially indicated the formation was very fine grained to a depth of at least several meters (*Muhleman et al.*, 1991). More recently, orbital radar observations by the Mars Advanced Radar for Subsurface and Ionospheric Sounding (MARSIS) instrument onboard the Mars Express spacecraft have shown the deposits to exhibit low attenuation to long wavelength ($\sim$100 m) radiation (*Watters et al.*, 2007). These observations are consistent either with a low dielectric constant due to an ice-rich composition, or with a low density material with exceptionally high porosity. Although in many locations the Medusa Fossae formation appears massive, large stratigraphic divisions have been mapped with thicknesses of hundreds of meters, while bedding can occasionally be identified at the 10 m scale (*Bradley et al.*, 2002).

Several outliers of the Medusa Fossae formation were imaged in stereo by HiRISE at 11° N, −162° E. The largest among these lies preserved within a preexisting 2 km diameter crater at −3400 m elevation, while other remnants are exposed on the surrounding plains. Particularly in the case of the material protected by the crater, bedding is well expressed. Aeolian erosion has exposed concentric rings of strata which seem to drape the underlying topography. Owing to their deposition within a crater, the layers are not planar over a lengthscale of more than hundreds of meters, complicating the measurement of bedding orientation. As at Gale, the deposits are of fairly uniform albedo, such that image brightness is dominated by topography rather than material differences. A section where the topography is fairly smooth (other than the differential erosion of the bedding) was extracted on the east side of the crater, where lighting conditions are most favorable. Due to the presence of a large intervening ridge, this record was extracted in two pieces sampling much, of the exposed stratigraphy. The two records are approximately 45 m and 30 m long respectively. Each of the sections show a dominant peak in their power spectra at roughly 3 m (2.8 m for the lower section, and 3.4 m for the upper section. This outcrop in the Medusa Fossae formation, halfway around the planet from western Arabia Terra, demonstrates that quasiperiodic stratigraphy is a global, rather than regional, phenomenon on Mars.

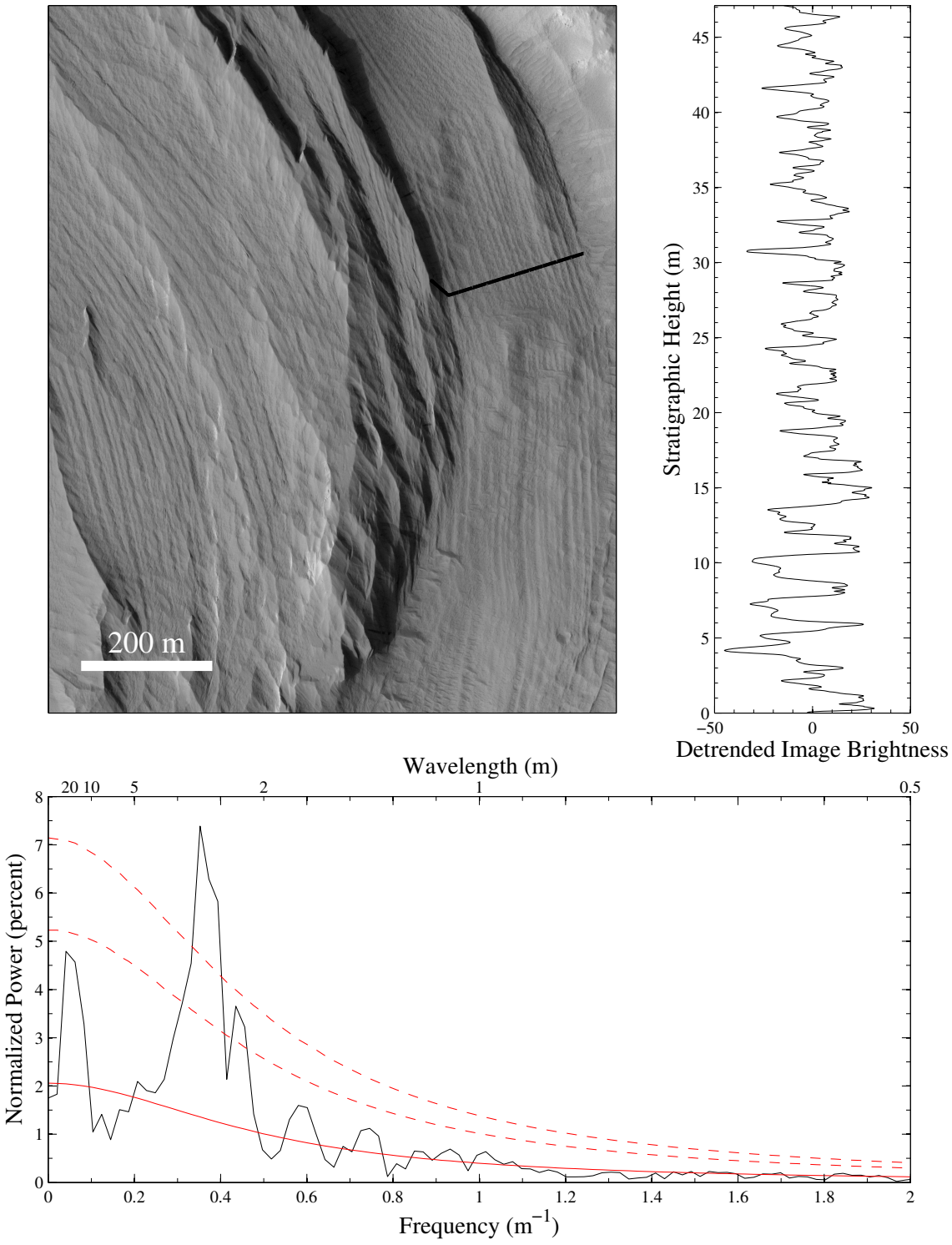

Figure 4.12: Bedding exposed in an outlier of the Medusa Fossae formation, preserved within a crater, as in Figure 4.6. Stereo image pair: PSP_003398_1910/PSP_003543_1910.

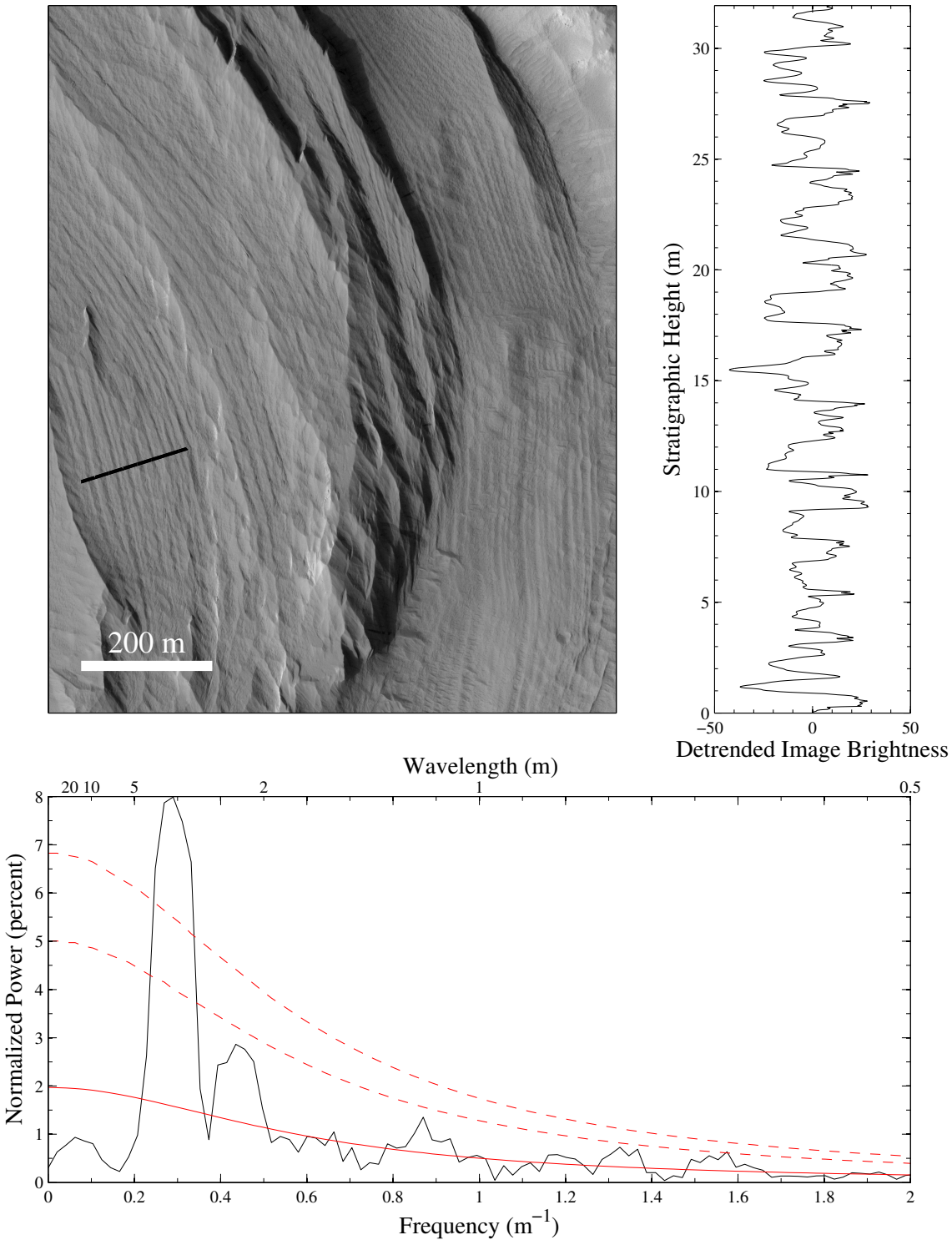

Figure 4.13: Bedding exposed in an outlier of the Medusa Fossae formation, preserved within a crater, as in Figure 4.6. Stereo image pair: PSP_003398_1910/PSP_003543_1910.

4.4.4 Aperiodic Stratigraphy

Although quasiperiodic stratigraphy has now been identified at several locations across Mars, the majority of sedimentary rocks on the planet do not exhibit this property. Several key examples are highlighted below which show aperiodic bedding, which is by far the more common characeristic among terrestrial rocks. The lack of expression of climate cyclicity in a given record may be due to a number of reasons. *Perron and Huybers* (2009) show that even small amounts of "jitter" in a record can suppress a periodic signal. However, the internal dynamics of a sedimentary system can easily dominate the stratigraphy, particularly in energetic systems where erosion alternates with deposition.

4.4.4.1 Juventae

One of the largest concentrations of sedimentary deposits on Mars is located within the chasma of the Valles Marineris system. Several of these large mounds of light-toned material are located on the floor of Juventae Chasma (labeled "A" through "D" by *Catling et al.* (2006). Observations by the CRISM and OMEGA spectrometers detect the presence of mono- and polyhydrated sulfate minerals in the mounds, particularly within mound "B" (*Gendrin et al.*, 2005; *Bishop et al.*, 2007). Previous authors have found some evidence for periodic brightness variations at one location on Mound "B" using High Resolution Stereo Camera (HRSC) stereo topographic data (*Milkovich et al.*, 2008).

HiRISE stereo data is not yet available for the area studied by *Milkovich et al.* (2008). However, we examined the neaby mound "C" for evidence of a dominant periodicity in the stratigraphy. The outcrop, located at 3.3° S, −61.7° E, covers much of the north face of the mound. Although rough surface topography overwhelms the bedding signal in places, we were able to recover a nearly 450 m long section. The surface exposure is very good, and clear of modern sedimentary cover. Unlike many of the sedimentary outcrops discussed above, beds do not have strongly differential resistance to erosion. Rather, brightness variations appear to be intrinsic properties of the stratigraphy, suggesting variable composition. Bedding orientation is consistent at roughly 7° to the south, into the mound. This may reflect topographic draping, a pattern which appears to be common on Mars, of the strata

over the north wall of the chasma. The consistency of the bedding attitude, as well as the lack of observed faults in the mound, indicates that tectonic disruption is not a complicating factor at this location.

The location and image brightness of the reconstructed sequence is shown in Figure 4.14a and b. The scale of the bedding is typically 1–10 m, although stratigraphic divisions are diffuse and may extend to scales below the image resolution. The power spectrum estimated from the brightness record is shown in Figure 4.14c, and conforms well to a red noise model. No statistically significant peaks are evident, with the exception of a secular trend at low frequencies. The wavelength of this secular component is 150 m, representing less than three full cycles, far too few to test for true periodicity. As for many of the sedimentary rocks of Mars, the formation process is unknown for the Juventae Chasma mounds. However, climate cyclicity does not seem to have left a dominant imprint on the stratigraphy, providing a counterexample to the sequences described in Arabia Terra.

4.4.4.2 Eberswalde

Eberswalde crater (located at 24° S, −34.7° E) hosts a remarkably well-preserved fluvial distributary network, and perhaps the best evidence of a deltaic environment on Mars, as discussed in chapter 2. First recognized by *Malin and Edgett* (2003) and *Moore et al.* (2003), the delta front exposes roughly 80 m of stratigraphy. As described by *Lewis and Aharonson* (2006), the bedding is generally parallel, with very low (<2°) dip angles. More recent measurements with HiRISE stereo data confirm these earlier results, constraining dips further to less than 1° on average. Some stratal truncations and bedding that is non-parallel can be observed in the higher resolution data, as expected for a dynamic fluvial system. CRISM visible/near IR spectroscopy shows the presence of hydrated phyllosilicates with in the exposed strata, further evidence for their deposition in an aqueous environment (*Mustard et al.*, 2008b).

Fluvial deltas are one of the classic examples of internal dynamics in a sedimentary system leading to quasiperiodic behavior, also known as autocyclicity. Repeated switching of deposition among delta lobes can lead to cyclic facies changes in the stratigraphic record, and has been observed to occur

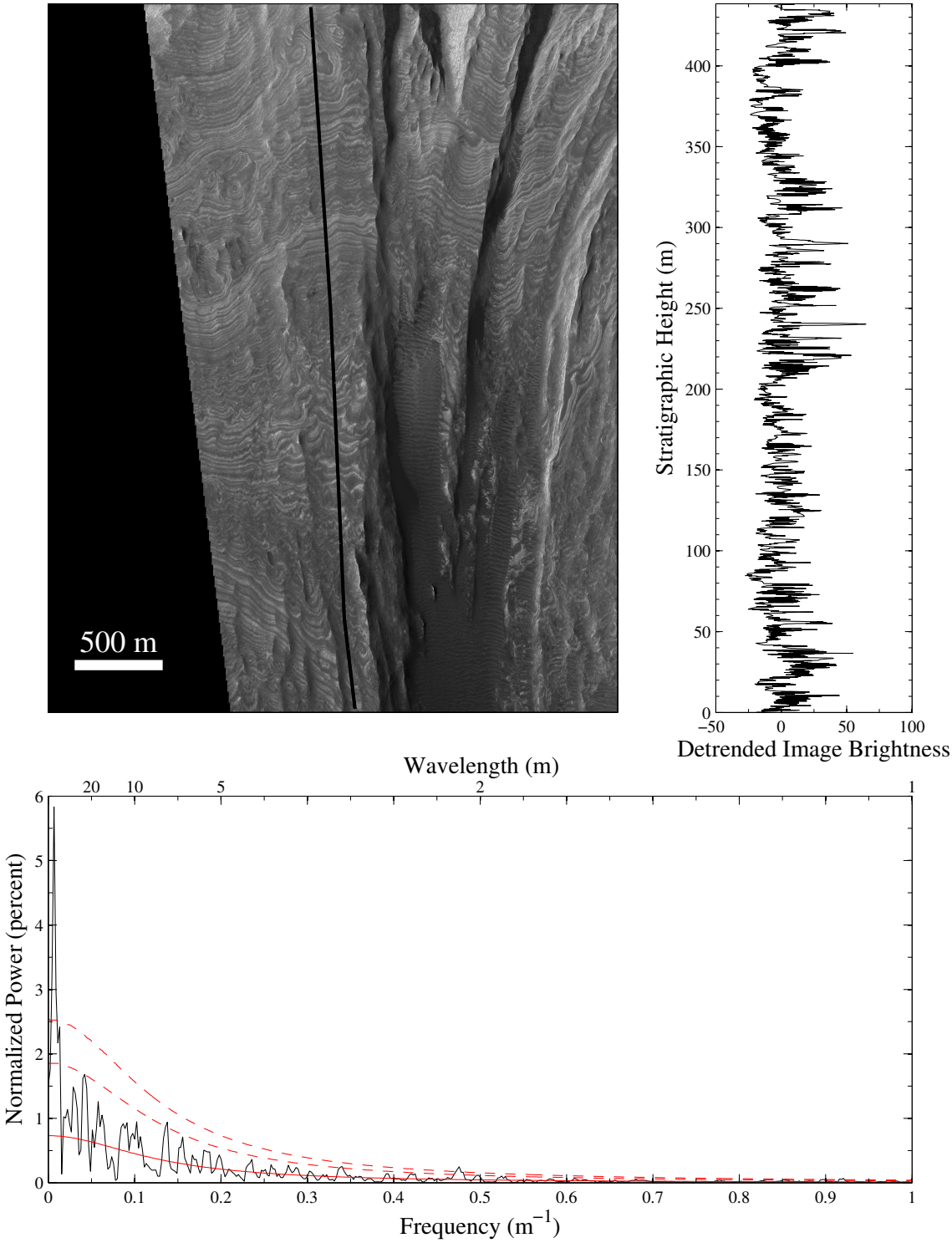

Figure 4.14: Bedding exposed in a large sedimentary mound in Juventae Chasma, as in Figure 4.6. No statistically significant periodic component is seen in the power spectrum. The peak at low frequencies corresponds to a wavelength of roughly 150 m, and likely represents secular variation of the record rather than a periodic component.

in modern deltas (*Coleman*, 1988). Flume studies and modelling by *Kim and Jerolmack* (2008) outline a second mechanism, whereby fan deltas may vary between storage and release phases for transported sediment, leading alternately to either sheet flow or incision on the delta surface, and cyclic changes in the associated facies. In both examples however, autocyclic systems may lead to repetitive depositional facies, although the resulting beds in the stratigraphic record are not necessarily periodic in thickness.

We extracted a grayscale record from the Eberswalde delta front near the thickest exposed section, shown in Figure 4.15a and b. Bedding tends to be moderately well expressed, with only weakly differentially resistant zones. Polygonal fracturing of the strata, not seen at other locations discussed in this study, may add noise to the grayscale record, but mostly at higher frequencies than the observed bedding scales of 1–10 m. The corresponding power spectrum in Figure 4.15c shows an excellent fit to an autoregressive background estimate, as in the Juventae Chasma example. No statistically significant periodicities are detected within these deltaic deposits.

4.4.5 Possible Stratigraphic Correlations

In general, quantitative correlation of non-contiguous stratigraphic sections on Mars is only made possible with the measurement of true bedding thicknesses. As it now stands, specific links between individual stratified outcrops have been difficult to demonstrate, leaving even their relative ages largely unknown. A successful effort would represent significant progress in understanding the martian geologic record. Although this study has not identified any specific bedding-scale markers, several connections may be drawn through the scales and morphologies observed at these sites. Although similar bedding scales alone do not alone prove a genetic link, it would be consistent with common formation from a series of regional depositional events.

Two possible stratigraphic relationships are hinted at by the above measurements, based on similar quasiperiodic bedding scales. The first potential link is between the two unnamed craters at 8° N, 353° E and 9° N, 359° E. These two craters are only a few hundred kilometers from each other, and exhibit some similar morphologic characteristics, as discussed above. The scale of bedding

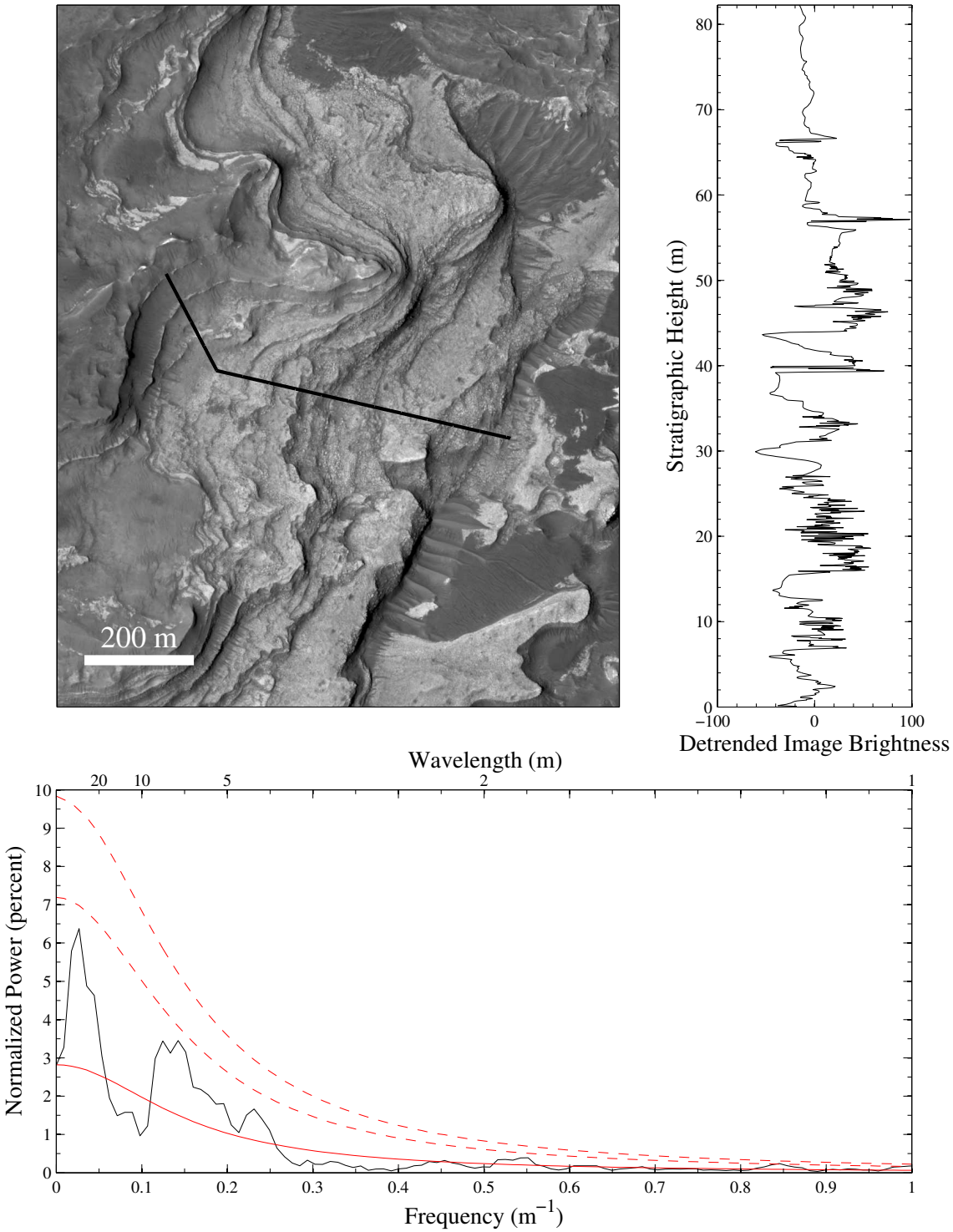

Figure 4.15: Bedding exposed in the frontal scarp of the delta in Eberswalde Crater, as in Figure 4.6. As in Juventae Chasma, no statistically significant periodic component is seen in the power spectrum. It is likely that the local dynamics of fluvial sedimentation dominated over climatic conditions in depositing the bedding. It is also possible that this deposit was laid down over a period of time far shorter than orbital timescales, as discussed in chapter 2.

within the latter is only slightly greater than that found at the 8° N, 353° E crater. The two discrete thickness distributions overlap, with 1-σ ranges of 8.8–12.0 m and 8.1–11.2 m for the 8° N, 353° E crater, and 10.0–15.1 m for the 9° N, 359° E crater. However, by comparing the empirical cumulative distribution functions via the Kolomogorov-Smirnov test, the hypothesis that they are drawn from the same population can be rejected at a 95% confidence level.

As a second test, the resolution of the power spectra can be examined to determine whether it is possible to distinguish the dominant peaks for the two sites. Spectral resolution is calculated as $\delta f = p/N \cdot \delta z$ for a record consisting of N observations of spacing δz, with the bandwidth parameter here chosen as $p = 2$ (*Mann and Lees*, 1996). The corresponding spectral peaks are indeed distinct at 0.096 ± 0.015 and 0.094 ± 0.011 for the to section within the 8° N, 353° E crater, and 0.065 ± 0.015 for the 9° N, 359° E crater. While the spectral peaks appear to be separable, the absolute thicknesses of the beds are sensitive to inaccuracies in dip. Thus, it cannot be ruled out with certainty that the beds in these two nearby craters exhibit essentially the same bedding scale. Alternatively, the deposits could have formed concurrently, but under different local deposition rates. If such a link existed, it would have implication for the both the formation mechanism and original extent of these sequences. A critical future test will involve examining the exposed stratigraphy in other nearby craters (e.g., those at 9° N, 358° E; 8.8° N, 358.2° E; and 11° N, 355.5° E) for bedding at similar scales.

A second possible link may exist between Gale crater and the Medusa Fossae formation, the two cyclic examples identified outside of Arabia Terra. Although the two outcrops are separated by 60° in longitude and over 3000 km, the greater Medusa Fossae formation spans tens of degrees, and reaches as far west a Gale crater (*Watters et al.*, 2007). Others have also suggested a relationship based on the morphological similarity and proximity of Gale crater to outcrops of the Medusa Fossae formation (*Thomson et al.*, 2008). Indeed, the sections presented here for the two sites have similar appearances, although this could also be due similarly thick dust mantles. The dominant bedding scales are similar, though not identical. From spectral analysis, the dominant frequencies are separable, at 0.221 ± 0.017 m^{-1} at Gale, versus 0.352 ± 0.042 m^{-1} and 0.290 ± 0.063 m^{-1}

within the Medusa Fossae formation. Still, in terms of absolute magnitude, the difference between a 4.4 m and 2.8–3.4 m wavelength is fairly small, particularly when compared to the 10–20 m beds measured in Arabia Terra. Given the kilometers thick record of the Medusa Fossae formation, the two analyzed sections could have been taken from very different portions of the same stratigraphic section, if they share a common formation. Once again, only with high resolution data for a number of other locations will it be possible to resolve this question.

4.4.5.1 Implications for Mars

The discovery of quasiperiodic bedding within several stratified deposits on Mars helps to answer some key questions regarding their origin, while posing additional ones. Although the formation mechanism cannot be determined with certainty, several possibilities rise as more likely, of which we find one to be most consistent with observed characteristics. As discussed in section 4.3.5, volcanic events are stochastic processes, which do not typically display periodic eruptive behavior, but rather exhibit power law behavior similar to that observed for earthquakes (*Pelletier*, 1999; *Simkin*, 1993). Similarly, impact events are well known to follow a power law size-frequency distribution. Sequences of ash deposits in either case would be unlikely to generate the observed bed thickness distributions. The additional discovery of quasiperiodic bedding ouside, or above the rim, of an enclosed basin, places additional constraints on their genesis. At least in the case of the Gale and Medusa Fossae sites along with the uppermost Crommelin mound, lacustrine deposition is ruled out. Lacustrine deposition is unlikely for the remaining Arabia sites, given the lack of contributing valleys which breach the crater rims. Precipitation of evaporitic minerals from solution via ground water seepage, as suggested by *Andrews-Hanna et al.* (2007), is also likely ruled out for the Gale and Medusa Fossae strata. Further, none of the Arabia locations contain purely horizontal bedding, a probable outcome of any groundwater model. Rather, the bedding dips in several cases trend toward the center of the craters, consistent with topographic draping.

Dust accumulation from aeolian airfall is a candidate formation process that is consistent with many of the above observations. All of the deposits are in generally dusty regions of Mars, as

determined by the TES instrument (*Ruff and Christensen*, 2002). The materials which comprise the strata remain unknown, although a weakly cemented dust accumulation would be consistent with the lack of strong mineral absorptions, as proposed for Pollack crater (*Ruff et al.*, 2001) and eastern Arabia Terra (*Fergason and Christensen*, 2008). Unfortunately, these results provide no new information regarding the presence or absence of accompanying ice, as inferred by *Watters et al.* (2007) for the Medusa Fossae formation. However, the detection of cyclicity likely rules out formation as a pyroclastic deposit.

The major outstanding question regards the relevant depositional timescales for rhythmic stratigraphy on Mars. Becquerel crater remains the only location where multiple bedding scales are apparent, allowing a tentative link to obliquity oscillations. This characteristic may be a result of the anomalously high latitude of Becquerel crater as compared to the other sites, which results in a different insolation pattern as a function of obliquity. For the other sites, only guesses can be made for the relevant forcing cycles. Given the scale of the bedding observed across these deposits, the smallest of which is 2.8 m, annual timescales would require extremely high deposition rates compared to modern sediment transport pathways. If the deposits are indeed related to orbital variations, they could have formed over millions of years. In the extreme, if the Medusa Fossae formation, over 3 km high in places, were composed entirely of 3 m beds representing 120 kyr cycles, the deposits could record over 100 Ma of martian history.

4.4.6 Conclusions

Quantitative analysis of the sedimentary rock record of Mars has become a reality, with the advent of high-resolution image, spectral, and topographic data. Topographic data from stereo HiRISE images allows the calculation of basic geologic quantities, such as bedding orientation and thickness. In several instances, we have shown sedimentary rock outcrops to contain quasiperiodic bedding, indicating repeating environmental changes as the rocks were deposited. While several of these sites lie within western Arabia Terra, two have also been found in far removed regions of the martian low latitudes, indicating widespread deposition of quasiperiodic sediments. Two representative out-

crops of martian sulfate terrains and deltaic sediments contain aperiodic bedding, counterexamples indicative of more complex depositional influences.

Within one crater, we have shown bedding thicknesses to be constant over kilometer lengthscales. While also demonstrating reproducability, this finding implicates a depositional process which acts uniformly over such distances. Stratigraphic correlations between separate outcrops of quasiperiodic bedding remain tentative. Still, two possibilities have been discussed where links may exist based on similar bedding scales. These represent fruitful opportunities for future HiRISE stereo targeting.

Two of the sections described here lie either above the rim of a closed basin (Gale crater) or outside of a closed basin entirely (Medusa Fossae formation). This observation alone has a strong bearing on the formation process, ruling out lacustrine and evarporative processes. With the observation of quasiperiodic strata, stochastic depositional processes like volcanism and impact cratering can also be ruled out. Our favored formation hypothesis is gradual accumulation of aeolian airfall dust which varies on the timescale of orbital oscillations. This hypothesis is in agreement with that previously suggested for similar deposits on Mars from thermal emission spectroscopic data. Future studies may help constrain the ages and durations of time represented by these sedimentary rocks. More specific correlation of bedding patterns between isolated outcrops holds the promise of contributing to the assembly of a global stratigraphy for the sedimentary rock record of Mars.

Bibliography

Ahlbrandt, T. S., and S. G. Fryberger (1982), Introduction to eolian deposits, in *Sandstone depositional environments*, vol. 31, edited by P. A. Scholle and D. Spearing, pp. 11–47, American Association of Petroleum Geologists Memoir, Tulsa, OK.

Albee, A. L., R. E. Arvidson, F. Palluconi, and T. Thorpe (2001), Overview of the Mars Global Surveyor mission, *J. Geophys. Res.*, *106*(E10), 23,291–23,316.

Alexander, D. A., R. G. Deen, P. M. Andres, P. Zamani, H. B. Mortensen, A. C. Chen, M. K. Cayanan, J. R. Hall, V. S. Klochko, O. Pariser, C. L. Stanley, C. K. Thompson, and G. M. Yagi (2006), Processing of Mars Exploration Rover imagery for science and operations planning, *J. Geophys. Res.*, *111*, E02S02, doi:10.1029/2005JE002462.

Andrews-Hanna, J. C., R. J. Phillips, and M. T. Zuber (2007), Meridiani Planum and the global hydrology of Mars, *Nature*, *446*, 163–166, doi:10.1038/nature05594.

Arvidson, R. E., S. W. Squyres, R. C. Anderson, J. F. Bell, D. Blaney, J. Brückner, N. A. Cabrol, W. M. Calvin, M. H. Carr, P. R. Christensen, B. C. Clark, L. Crumpler, D. J. D. Marais, P. A. de Souza Jr., C. d'Uston, T. Economou, J. Farmer, W. H. Farrand, W. Folkner, M. Golombek, S. Gorevan, J. A. Grant, R. Greeley, J. Grotzinger, E. Guinness, B. C. Hahn, L. Haskin, K. E. Herkenhoff, J. A. Hurowitz, S. Hviid, J. R. Johnson, G. Klingelhöfer, A. H. Knoll, G. Landis, C. Leff, M. Lemmon, R. Li, M. B. Madsen, M. C. Malin, S. M. McLennan, H. Y. McSween, D. W. Ming, J. Moersch, R. V. Morris, T. Parker, J. W. R. Jr., L. Richter, R. Rieder, D. S. Rodionov, C. Schröder, M. Sims, M. Smith, P. Smith, L. A. Soderblom, R. Sullivan, S. D. Thompson, N. J. Tosca, A. Wang, H. Wänke, J. Ward, T. Wdowiak, M. Wolff, and A. Yen (2006), Overview of the

Spirit Mars Exploration Rover mission to Gusev Crater: Landing site to Backstay Rock in the Columbia Hills, *J. Geophys. Res.*, *111*, E02S01, doi:10.1029/2005JE002499.

Arvidson, R. E., S. W. Ruff, R. V. Morris, D. W. Ming, L. S. Crumpler, A. S. Yen, S. W. Squyres, R. J. Sullivan, J. F. Bell III, N. A. Cabrol, B. C. Clark, W. H. Farrand, R. Gellert, R. Greenberger, J. A. Grant, E. A. Guinness, K. E. Herkenhoff, J. A. Hurowitz, J. R. Johnson, G. Klingelhöfer, K. W. Lewis, R. Li, T. J. McCoy, J. Moersch, H. Y. McSween, S. L. Murchie, M. Schmidt, C. Schröder, A. Wang, S. Wiseman, M. B. Madsen, W. Goetz, and S. M. McLennan (2008), Spirit Mars rover mission to the Columbia Hills, Gusev Crater: Mission overview and selected results from the Cumberland Ridge to Home Plate, *J. Geophys. Res.*, *113*, E12S33, doi:10.1029/2008JE003183.

Bell III, J. F., S. W. Squyres, K. E. Herkenhoff, J. N. Maki, H. M. Arneson, D. Brown, S. A. Collins, A. Dingizian, S. T. Elliot, E. C. Hagerott, A. G. Hayes, M. J. Johnson, J. R. Johnson, J. Joseph, K. Kinch, M. T. Lemmon, R. V. Morris, L. Scherr, M. Schwochert, M. K. Shepard, G. H. Smith, J. N. Sohl-Dickstein, R. J. Sullivan, W. T. Sullivan, and W. M. (2003), Mars Exploration Rover Athena Panoramic Camera (Pancam) investigation, *J. Geophys. Res.*, *108*(E12), 8063, doi:10.1029/2003JE002070.

Bhattacharya, J. P., T. H. D. Payenberg, S. C. Lang, and M. Bourke (2005), Dynamic river channels suggest a long-lived Noachian crater lake on Mars, *Geophys. Res. Lett.*, *32*, L10,201, doi: 10.1029/2005GL022747.

Bibring, J.-P., Y. Langevin, A. Gendrin, B. Gondet, F. Poulet, M. Berthé, A. Soufflot, R. Arvidson, N. Mangold, J. Mustard, and P. Drossart (2005), Mars surface diversity as revealed by the OMEGA/Mars Express observations, *Science*, *307*, 1576–1581, doi:10.1126/science.1108806.

Bibring, J.-P., R. E. Arvidson, A. Gendrin, B. Gondet, Y. Langevin, S. Le Mouelic, N. Mangold, R. V. Morris, J. F. Mustard, F. Poulet, C. Quantin, and C. Sotin (2007), Coupled ferric oxides and sulfates on the martian surface, *Science*, *317*, 1206–1210, doi:10.1126/science.1144174.

Bishop, J. L., E. N. Dobrea, S. L. Murchie, C. M. Weitz, W. M. Calvin, L. A. Roach, S. M. Pelkey, A. J. Brown, J. F. Mustard, J.-P. Bibring, and Mro Crism Team (2007), Sulfates and mafic minerals in Juventae Chasma as seen by CRISM in coordination with OMEGA, HiRISE and Context Images, *7th International Coference on Mars*, abstract #3350.

Bishop, J. L., E. Z. N. Dobrea, N. K. McKeown, M. Parente, B. L. Ehlmann, J. R. Michalski, R. E. Milliken, F. Poulet, G. A. Swayze, J. F. Mustard, S. L. Murchie, and J.-P. Bibring (2008), Phyllosilicate diversity and past aqueous activity revealed at Mawrth Vallis, Mars, *Science*, *321*, 830–833, doi:10.1126/science.1159699.

Bradley, B. A., S. E. H. Sakimoto, H. Frey, and J. R. Zimbelman (2002), Medusae Fossae Formation: New perspectives from Mars Global Surveyor, *J. Geophys. Res.*, *107*(E8), 5058, doi: 10.1029/2001JE001537.

Cabrol, N. A., and E. A. Grin (1999), Distribution, classification, and ages of martian impact crater lakes, *Icarus*, *142*(1), 160–172.

Cabrol, N. A., E. A. Grin, H. E. Newsom, R. Landheim, and C. P. McKay (1999), Hydrogeologic evolution of Gale crater and its relevance to the exobiological exploration of Mars, *Icarus*, *139*(2), 235–245.

Carlson, J., and J. Grotzinger (2001), Submarine fan environment inferred from turbidite thickness distributions, *Sedimentology*, *48*(6), 1331–1351.

Carr, M. H. (1996), *Water on Mars*, 229 pp., Oxford University Press, New York.

Carr, M. H., and F. C. Chuang (1997), Martian drainage densities, *J. Geophys. Res.*, *102*, 9145–9152.

Cas, R. A. F., and J. V. Wright (1987), *Volcanic Successions, Modern and Ancient: a Geological Approach to Processes, Products and Successions*, Allen & Unwin, Boston.

Catling, D. C., S. E. Wood, C. Leovy, D. R. Montgomery, H. M. Greenberg, C. R. Glein, and J. M. Moore (2006), Light-toned layered deposits in Juventae Chasma, Mars, *Icarus*, *181*, 26–51, doi:10.1016/j.icarus.2005.10.020.

Christensen, P. R., and H. J. Moore (1992), The Martian surface layer, in *Mars*, edited by H. H. Kieffer, B. M. Jakosky, C. W. Snyder, and M. S. Matthews, pp. 686–729, University of Arizona Press, Tucson.

Christensen, P. R., J. L. Bandfield, V. E. Hamilton, S. W. Ruff, H. H. Kieffer, T. N. Titus, M. C. Malin, R. V. Morris, M. D. Lane, R. L. Clark, B. M. Jakosky, M. T. Mellon, J. C. Pearl, B. J. Conrath, M. D. Smith, R. T. Clancy, R. O. Kuzmin, T. Roush, G. L. Mehall, N. Gorelick, K. Bender, K. Murray, S. Dason, E. Greene, S. Silverman, and M. Greenfield (2001), Mars Global Surveyor Thermal Emission Spectrometer experiment: Investigation description and surface science results, *J. Geophys. Res.*, *106*, 23,823–23,871.

Cole, P. D. (1991), Migration direction of sand-wave structures in pyroclastic surge deposits: Implications for depositional processes, *Geology*, *19*, 1108–1111.

Cole, P. D., J. Guest, A. Duncan, and J. Pacheco (2001), Capelinhos 1957-1958, Faial, Azores: Deposits formed by an emergent surtseyan eruption, *Bulletin of Volcanology*, *63*(2), 204–220.

Coleman, J. M. (1988), Dynamic changes and processes in the Mississippi River delta, *Bull. Geo. Soc. Am.*, *100*(7), 999–1015.

Craddock, R. A., and A. D. Howard (2002), The case for rainfall on a warm, wet early Mars, *J. Geophys. Res.*, *107*(E11), 21–1.

Crowe, B. M., and R. V. Fisher (1973), Sedimentary structures in base-surge deposits with special reference to cross-bedding, Ubehebe craters, Death Valley, California, *Bulletin of the Geological Society of America*, *84*(2), 663–681.

Crumpler, L. S., S. W. Squyres, R. E. Arvidson, J. F. Bell, III, D. Blaney, N. A. Cabrol, P. R. Christensen, D. J. Desmarais, J. D. Farmer, R. Fergason, M. P. Golombek, F. D. Grant, J. A. Grant, R. Greeley, B. Hahn, K. E. Herkenhoff, J. A. Hurowitz, A. T. Knudson, G. A. Landis, R. Li, J. Maki, H. Y. McSween, D. W. Ming, J. E. Moersch, M. C. Payne, J. W. Rice, L. Richter, S. W. Ruff, M. Sims, S. D. Thompson, N. Tosca, A. Wang, P. Whelley, S. P. Wright, and M. B.

Wyatt (2005), Mars Exploration Rover Geologic traverse by the Spirit rover in the Plains of Gusev Crater, Mars, *Geology*, *33*(10), 809–812, doi:10.1130/G21673.1.

Crumpler, L. S., T. McCoy, and the Athena Science Team (2006), MER surface geologic transect mapping in the plains and hills, Gusev Crater, *Lunar Planet. Sci. Conf.*, *XXXVII*, abstract #1685.

Cutts, J. A., and B. H. Lewis (1982), Models of climate cycles recorded in Martian polar layered deposits, *Icarus*, *50*(2-3), 216–244, doi:10.1016/0019-1035(82)90124-5.

Dabrio, C. J. (1990), Fan-delta facies associations in late Neogene and Quaternary basins of south-eastern Spain, in *Coarse-Grained Deltas*, edited by A. Colella and D. B. Prior, pp. 91–111, Blackwell Scientific, Oxford.

Edgett, K. S. (2002), Low-albedo surfaces and eolian sediment: Mars Orbiter Camera views of western Arabia Terra craters and wind streaks, *J. Geophys. Res.*, *107*(E6), 5038.

Edgett, K. S., and M. C. Malin (2002), Martian sedimentary rock stratigraphy: Outcrops and interbedded craters of northwest Sinus Meridiani and southwest Arabia Terra, *Geophys. Res. Lett.*, *29*(24), 2179, doi:10.1029/2002GL016515.

Edgett, K. S., B. J. Butler, J. R. Zimbelman, and V. E. Hamilton (1997), Geologic context of the Mars radar "Stealth" region in southwestern Tharsis, *J. Geophys. Res.*, *102*, 21,545–21,568, doi:10.1029/97JE01685.

Ehlmann, B. L., J. F. Mustard, S. L. Murchie, F. Poulet, J. L. Bishop, A. J. Brown, W. M. Calvin, R. N. Clark, D. J. Des Marais, R. E. Milliken, L. H. Roach, T. L. Roush, G. A. Swayze, and J. J. Wray (2008), Orbital Identification of Carbonate-Bearing Rocks on Mars, *Science*, *322*, 1828–1832, doi:10.1126/science.1164759.

Fanale, F. P., and J. R. Salvail (1994), Quasi-periodic atmosphere-regolith-cap CO_2 redistribution in the martian past, *Icarus*, *111*(2), 305–316, doi:10.1006/icar.1994.1147.

Fassett, C. I., and J. W. Head (2005), Fluvial sedimentary deposits on Mars: Ancient deltas in a crater lake in the Nili Fossae region, *Geophys. Res. Lett.*, *32*, 14,201, doi:10.1029/2005GL023456.

Fergason, R. L., and P. R. Christensen (2008), Formation and erosion of layered materials: Geologic and dust cycle history of eastern Arabia Terra, Mars, *J. Geophys. Res.*, *113*(E12), 12,001, doi: 10.1029/2007JE002973.

Fischer, A. G. (1986), Climatic Rhythms Recorded in Strata, *Annu. Rev. Earth Planet. Sci.*, *14*, 351, doi:10.1146/annurev.ea.14.050186.002031.

Fisher, R. V., and H.-U. Schmincke (1984), *Pyroclastic Rocks*, Springer-Verlag, New York.

Fisher, R. V., and A. C. Waters (1970), Base surge bed forms in maar volcanoes, *American Journal of Science*, *268*(2), 157.

Gendrin, A., N. Mangold, J.-P. Bibring, Y. Langevin, B. Gondet, F. Poulet, G. Bonello, C. Quantin, J. Mustard, R. Arvidson, and S. LeMouélic (2005), Sulfates in martian layered terrains: The OMEGA/Mars Express view, *Science*, *307*, 1587–1591, doi:10.1126/science.1109087.

Glotch, T. D., and A. D. Rogers (2007), Evidence for aqueous deposition of hematite-and sulfate-rich light-toned layered deposits in Aureum and Iani Chaos, Mars, *J. Geophys. Res.*, *112*, E06,001.

Grant, J., R. Irwin III, J. Grotzinger, R. Milliken, L. Tornabene, A. McEwen, C. Weitz, S. Squyres, T. Glotch, and B. Thomson (2008), HiRISE imaging of impact megabreccia and sub-meter aqueous strata in Holden Crater, Mars, *Geology*, *36*(3), 195, doi:10.1130/G24340A.1.

Grant, J. A., R. E. Arvidson, L. S. Crumpler, M. P. Golombek, B. Hahn, A. F. C. Haldemann, R. Li, L. A. Soderblom, S. W. Squyres, S. P. Wright, and W. A. Watters (2005), Crater gradation in Gusev crater and Meridiani Planum, Mars, *J. Geophys. Res*, *111*, E02S08, doi:10.1029/2005JE002,465.

Greeley, R., S. W. Squyres, R. E. Arvidson, P. Bartlett, J. F. Bell, D. Blaney, N. A. Cabrol, J. Farmer, B. Farrand, M. P. Golombek, S. P. Gorevan, J. A. Grant, A. F. C. Haldemann, K. E. Herkenhoff, J. Johnson, G. Landis, M. B. Madsen, S. M. McLennan, J. Moersch, J. W. Rice, L. Richter, S. Ruff, R. J. Sullivan, S. D. Thompson, A. Wang, C. M. Weitz, and P. Whelley (2004),

Wind-related processes detected by the Spirit rover at Gusev crater, Mars, *Science*, *305*(5685), 810–821, doi:10.1126/science.1100108.

Grin, E. A., and N. A. Cabrol (1997), Limnologic analysis of Gusev crater paleolake, Mars, *Icarus*, *130*(2), 461–474.

Grotzinger, J. P., R. E. Arvidson, J. F. B. III, W. Calvin, B. C. Clark, D. A. Fike, M. Golombek, R. Greeley, A. Haldemann, K. E. Herkenhoff, B. L. Jolliff, A. H. Knoll, M. Malin, S. M. McLennan, T. Parker, L. Soderblom, J. N. Sohl-Dickstein, S. W. Squyres, N. J. Tosca, and W. Watters (2005), Stratigraphy and sedimentology of a dry to wet eolian depositional system, Burns formation, Meridiani Planum, Mars, *Earth Planet. Sci. Lett*, *240*, 11–72.

Head, J. W., J. F. Mustard, M. A. Kreslavsky, R. E. Milliken, and D. R. Marchant (2003), Recent ice ages on Mars, *Nature*, *426*, 797–802.

Herkenhoff, K. E., S. W. Squyres, R. Arvidson, D. S. Bass, J. F. Bell, P. Bertelsen, N. A. Cabrol, L. Gaddis, A. G. Hayes, S. F. Hviid, J. R. Johnson, K. M. Kinch, M. B. Madsen, J. N. Maki, S. M. McLennan, H. Y. McSween, J. W. Rice, M. Sims, P. H. Smith, L. A. Soderblom, N. Spanovich, R. Sullivan, and A. Wang (2004), Textures of the soils and rocks at Gusev Crater from Spirit's Microscopic Imager, *Science*, *305*, 824–827.

Hinnov, L. A. (2000), New Perspectives on Orbitally Forced Stratigraphy, *Annual Review of Earth and Planetary Sciences*, *28*, 419–475, doi:10.1146/annurev.earth.28.1.419.

House, M. R. (1995), Orbital forcing timescales; an introduction, in *Orbital Forcing Timescales and Cyclostratigraphy*, edited by M. R. House and A. S. Gale, pp. 1–18, Geological Society of London, London.

Hynek, B. M., and R. J. Phillips (2003), New data reveal mature, integrated drainage systems on Mars indicative of past precipitation, *Geology*, *31*, 757–+.

Irwin, I., R. P., A. D. Howard, R. A. Craddock, and J. M. Moore (2005), An intense terminal epoch

of widespread fluvial activity on early Mars: 2. Increased runoff and paleolake development, *J. Geophys. Res.*, *119*(E12S15).

Ivanov, A. B. (2003), Ten-meter scale topography and roughness of Mars Exploration Rover landing sites and Martian polar regions, in *Lunar and Planetary Science Conference XXXIV*, abstract #2084.

Ivanov, A. B., and J. Lorre (2002), Analysis of Mars Orbiter Camera stereopairs, in *Lunar and Planetary Science Conference XXXII*, abstract #1845.

Jaeger, W. L., L. P. Keszthelyi, A. S. McEwen, C. M. Dundas, and P. S. Russell (2007), Athabasca Valles, Mars: A lava-draped channel system, *Science*, *317*(5845), 1709–1711, doi: 10.1126/science.1143315.

Jerolmack, D. J., D. Mohrig, M. T. Zuber, and S. Byrne (2004), A minimum time for the formation of Holden Northeast fan, Mars, *Geophys. Res. Lett.*, *31*, 21,701+.

Jerolmack, D. J., D. Mohrig, J. P. Grotzinger, D. A. Fike, and W. A. Watters (2006), Spatial grain size sorting in eolian ripples and estimation of wind conditions on planetary surfaces: Application to Meridiani Planum, Mars, *J. Geophys. Res.*, *111*, E12S02, doi:10.1029/2005JE002544.

Kahn, R., T. Martin, R. Zurek, and S. Lee (1992), The martian dust cycle, in *Mars*, edited by H. H. Kieffer, B. M. Jakosky, C. W. Snyder, and M. S. Matthews, pp. 1017–1053, University of Arizona Press, Tucson.

Kieffer, H. H., and A. P. Zent (1992), Quasi-periodic climate change on mars, in *Mars*, edited by H. H. Kieffer, B. M. Jakosky, C. W. Snyder, and M. S. Matthews, pp. 1180–1218, University of Arizona Press, Tucson.

Kim, W., and D. J. Jerolmack (2008), The Pulse of Calm Fan Deltas, *Geology*, *116*(4), 315–330, doi:10.1086/588830.

Kirk, R. L., L. A. Soderblom, E. Howington-Kraus, and B. A. Archinal (2002), USGS High-resolution

topomapping of Mars with Mars Orbiter Camera narrow-angle images, in *ISPRS Commission IV, Symposium 2002, Ottawa, Canada, July 9-12*.

Kirk, R. L., E. Howington-Kraus, M. R. Rosiek, J. A. Anderson, B. A. Archinal, K. J. Becker, D. A. Cook, D. M. Galuszka, P. E. Geissler, T. M. Hare, I. M. Holmberg, L. P. Keszthelyi, B. L. Redding, A. W. Delamere, D. Gallagher, J. D. Chapel, E. M. Eliason, R. King, and A. S. McEwen (2008), Ultrahigh resolution topographic mapping of Mars with MRO HiRISE stereo images: Meter-scale slopes of candidate Phoenix landing sites, *J. Geophys. Res.*, *113*(E00A24), doi:doi:10.1029/2007JE003000.

Kocurek, G. (1991), Interpretation of ancient eolian sand dunes, *Annual Review of Earth and Planetary Sciences*, *19*(1), 43–75.

Komatsu, G., G. G. Ori, P. Ciarcelluti, and Y. D. Litasov (2004), Interior layered deposits of Valles Marineris, Mars: Analogous subice volcanism related to Baikal Rifting, Southern Siberia, *Planet. Space Sci.*, *52*, 167–187, doi:10.1016/j.pss.2003.08.003.

Landis, G. A., and P. P. Jenkins (2000), Measurement of the settling rate of atmospheric dust on Mars by the MAE instrument on Mars Pathfinder, *J. Geophys. Res.*, *105*, 1855–1858.

Laskar, J., B. Levrard, and J. F. Mustard (2002), Orbital forcing of the martian polar layered deposits, *Nature*, *419*, 375–377.

Laskar, J., A. C. M. Correia, M. Gastineau, F. Joutel, B. Levrard, and P. Robutel (2004), Long term evolution and chaotic diffusion of the insolation quantities of Mars, *Icarus*, *170*, 343–364, doi:10.1016/j.icarus.2004.04.005.

Lewis, K. W., and O. Aharonson (2004), Characterization of the distributary fan in Holden NE crater using stereo analysis, in *Lunar and Planetary Institute Conference XXXV*, abstract #2083.

Lewis, K. W., and O. Aharonson (2006), Stratigraphic analysis of the distributary fan in Eberswalde crater using stereo imagery, *J. Geophys. Res.*, *111*(E06001), doi:10.1029/2005JE002558.

Lewis, K. W., O. Aharonson, M. E. Schmidt, and the Athena Science Team (2007), Stratigraphy and structure of Inner Basin outcrops in the Columbia Hills from the Spirit Rover, *Lunar Planet. Sci. Conf.*, *XXXVIII*, abstract #2393.

Lewis, K. W., O. Aharonson, J. P. Grotzinger, R. L. Kirk, A. S. McEwen, and T.-A. Suer (2008a), Quasi-periodic bedding in the sedimentary rock record of Mars, *Science*, *322*, 1532–, doi:10.1126/science.1161870.

Lewis, K. W., O. Aharonson, J. P. Grotzinger, S. W. Squyres, J. F. Bell III, L. S. Crumpler, and M. E. Schmidt (2008b), Structure and stratigraphy of Home Plate from the Spirit Mars Exploration Rover, *J. Geophys. Res.*, *113*, E12S36, doi:10.1029/2007JE003025.

Lorenz, V. (1973), On the formation of maars, *Bulletin of Volcanology*, *37*(2), 183–204.

Maki, J. N., J. F. Bell III, K. E. Herkenhoff, S. W. Squyres, A. Kiely, M. Klimesh, M. Schwochert, T. Litwin, R. Willson, A. Johnson, M. Maimone, E. Baumgartner, A. Collins, M. Wadsworth, S. T. Elliot, A. Dingizian, D. Brown, E. C. Hagerott, L. Scherr, R. Deen, D. Alexander, and J. Lorre (2003), Mars Exploration Rover Engineering Cameras, *J. Geophys. Res.*, *108*(E12), 8071, doi:10.1029/2003JE002077.

Malamud, B. D., and D. L. Turcotte (2006), The applicability of power-law frequency statistics to floods, *Journal of Hydrology*, *322*(1-4), 168–180, doi:10.1016/j.jhydrol.2005.02.032.

Malin, M. C., and K. S. Edgett (2000), Sedimentary rocks of early Mars, *Science*, *290*, 1927–1937.

Malin, M. C., and K. S. Edgett (2001), Mars Global Surveyor Mars Orbiter Camera: Interplanetary cruise through primary mission, *J. Geophys. Res.*, *106*(E10), 23,429–23,570.

Malin, M. C., and K. S. Edgett (2003), Evidence for Persistent Flow and Aqueous Sedimentation on Early Mars, *Science*, *302*, 1931–1934.

Malin, M. C., G. E. Danielson, A. P. Ingersoll, H. Masursky, J. Veverka, M. A. Ravine, and T. A. Soulanille (1992), Mars observer camera, *J. Geophys. Res.*, *97*, 7699–7718.

Mangold, N., F. Poulet, J. F. Mustard, J.-P. Bibring, B. Gondet, Y. Langevin, V. Ansan, P. Masson, C. Fassett, J. W. Head, H. Hoffmann, and G. Neukum (2007), Mineralogy of the Nili Fossae region with OMEGA/Mars Express data: 2. Aqueous alteration of the crust, *J. Geophys. Res.*, *112*(E08S04), doi:10.1029/2006JE002835.

Mann, M. E., and J. M. Lees (1996), Robust estimation of background noise and signal detection in climatic time series, *Climatic Change*, *33*(3), 409–445, doi:10.1007/BF00142586.

Martınez-Alonso, S., B. M. Jakosky, M. T. Mellon, and N. E. Putzig (2005), A volcanic interpretation of Gusev Crater surface materials from thermophysical, spectral, and morphological evidence, *J. Geophys. Res.*, *110*, E01003, doi:10.1029/2004JE002327.

McCollom, T. M., and B. M. Hynek (2005), A volcanic environment for bedrock diagenesis at Meridiani Planum on Mars, *Nature*, *438*, 1129–1131, doi:10.1038/nature04390.

McCoy, T. J., M. Sims, M. E. Schmidt, L. Edwards, L. L. Tornabene, L. S. Crumpler, B. A. Cohen, L. A. Soderblom, D. L. Blaney, S. W. Squyres, J. W. Rice Jr., E. Treguier, C. d'Uston, J. A. Grant, H. Y. McSween Jr., M. P. Golombek, A. F. C. Haldemann, and P. A. de Souza Jr. (2008), Structure, stratigraphy, and origin of Husband Hill, Columbia Hills, Gusev Crater, Mars, *J. Geophys. Res.*, *113*, E06S03, doi:10.1029/2007JE003041.

McEwen, A. S., E. M. Eliason, J. W. Bergstrom, N. T. Bridges, C. J. Hansen, W. A. Delamere, J. A. Grant, V. C. Gulick, K. E. Herkenhoff, L. Keszthelyi, R. L. Kirk, M. T. Mellon, S. W. Squyres, N. Thomas, and C. M. Weitz (2007), Mars Reconnaissance Orbiter's High Resolution Imaging Science Experiment (HiRISE), *J. Geophys. Res.*, *112*(E05S02), doi:10.1029/2005JE002605.

McSween, H. Y., R. E. Arvidson, J. F. Bell, D. Blaney, N. A. Cabrol, P. R. Christensen, B. C. Clark, J. A. Crisp, L. S. Crumpler, D. J. Des Marais, J. D. Farmer, R. Gellert, A. Ghosh, S. Gorevan, T. Graff, J. Grant, L. A. Haskin, K. E. Herkenhoff, J. R. Johnson, B. L. Jolliff, G. Klingelhoefer, A. T. Knudson, S. McLennan, K. A. Milam, J. E. Moersch, R. V. Morris, R. Rieder, S. W. Ruff, P. A. de Souza, S. W. Squyres, H. Wänke, A. Wang, M. B. Wyatt, A. Yen, and J. Zipfel (2004), Basaltic rocks analyzed by the Spirit rover in Gusev Crater, *Science*, *305*, 842–845.

Melosh, H. J. (1989), *Impact Cratering: A Geologic Process*, 245 pp., Oxford Univ. Press, New York.

Milkovich, S. M., and J. W. Head (2005), North polar cap of Mars: Polar layered deposit characterization and identification of a fundamental climate signal, *J. Geophys. Res.*, *110*(E01005), doi:10.1029/2004JE002349.

Milkovich, S. M., J. W. Head, and G. Neukum (2008), Stratigraphic analysis of the northern polar layered deposits of Mars: Implications for recent climate history, *Planetary and Space Science*, *56*(2), 266–288, doi:10.1016/j.pss.2007.08.004.

Milliken, R. E., K. S. Edgett, G. Swayze, R. N. Clark, B. J. Thomson, R. Anderson, and J. F. Bell III (2009), Clay and sulfate-bearing rocks in a stratigraphic sequence in Gale crater, in *Lunar and Planetary Science Conference*, vol. XL, abstract #1479.

Milton, N. J., and G. T. Bertram (1995), Topset play types and their controls, in *Sequence Stratigraphy of Foreland Basin Deposits*, edited by J. C. van Wagoner and G. T. Bertram, pp. 1–9, AAPG, Tulsa, Oklahoma.

Ming, D. W., R. Gellert, R. V. Morris, R. E. Arvidson, J. Brückner, B. C. Clark, B. A. Cohen, C. d'Uston, T. Economou, I. Fleischer, G. Klingelhöfer, T. J. McCoy, D. W. Mittlefehldt, M. E. Schmidt, C. Schröder, S. W. Squyres, E. Treguier, A. S. Yen, and J. Zipfel (2008), Geochemical properties of rocks and soils in Gusev Crater, Mars: Results of the Alpha Particle X-Ray Spectrometer from Cumberland Ridge to Home Plate, *J. Geophys. Res.*, *113*, E12S39, doi:10.1029/2008JE003195.

Moore, J. M., and A. D. Howard (2005), Large alluvial fans on Mars, *J. Geophys. Res.*, *110*(E04005), doi:10.1029/2004JE002352.

Moore, J. M., A. D. Howard, W. E. Dietrich, and P. M. Schenk (2003), Martian Layered Fluvial Deposits: Implications for Noachian Climate Scenarios, *Geophys. Res. Lett.*, *30*(24), 2292+.

Morris, R. V., G. Klingelhöfer, C. Schröder, D. S. Rodionov, A. Yen, D. W. Ming, P. A. de Souza, I. Fleischer, T. Wdowiak, R. Gellert, B. Bernhardt, E. N. Evlanov, B. Zubkov, J. Foh, U. Bonnes,

E. Kankeleit, P. Gütlich, F. Renz, S. W. Squyres, and R. E. Arvidson (2006), Mössbauer mineralogy of rock, soil, and dust at Gusev crater, Mars: Spirit's journey through weakly altered olivine basalt on the plains and pervasively altered basalt in the Columbia Hills, *J. Geophys. Res.*, *111*, E02S13, doi:10.1029/2005JE002584.

Morris, R. V., G. Klingelhöfer, C. Schröder, I. Fleischer, D. W. Ming, A. S. Yen, R. Gellert, R. E. Arvidson, D. S. Rodionov, L. S. Crumpler, B. C. Clark, B. A. Cohen, T. J. McCoy, D. W. Mittlefehldt, M. E. Schmidt, P. A. de Souza Jr., and S. W. Squyres (2008), Iron mineralogy and aqueous alteration from Husband Hill through Home Plate at Gusev Crater, Mars: Results from the Mössbauer instrument on the Spirit Mars Exploration Rover, *J. Geophys. Res.*, *113*, E12S42, doi:doi:10.1029/2008JE003201.

Muhleman, D. O., B. J. Butler, A. W. Grossman, and M. A. Slade (1991), Radar images of Mars, *Science*, *253*, 1508–1513, doi:10.1126/science.253.5027.1508.

Mustard, J. F., S. L. Murchie, B. L. Ehlmann, R. E. Milliken, J.-P. Bibring, F. Poulet, J. L. Bishop, L. H. Roach, F. P. Seelos, and Crism Science Team (2008a), Regional geology and stratigraphy of the Nili Fossae-Syrtis-Isidis region: New insights from CRISM and MRO data, in *Lunar and Planetary Science Conference XXXIX*, abstract #1701.

Mustard, J. F., S. L. Murchie, S. M. Pelkey, B. L. Ehlmann, R. E. Milliken, J. A. Grant, J.-P. Bibring, F. Poulet, J. Bishop, E. N. Dobrea, L. Roach, F. Seelos, R. E. Arvidson, S. Wiseman, R. Green, C. Hash, D. Humm, E. Malaret, J. A. McGovern, K. Seelos, T. Clancy, R. Clark, D. D. Marais, N. Izenberg, A. Knudson, Y. Langevin, T. Martin, P. McGuire, R. Morris, M. Robinson, T. Roush, M. Smith, G. Swayze, H. Taylor, T. Titus, and M. Wolff (2008b), Hydrated silicate minerals on Mars observed by the Mars Reconnaissance Orbiter CRISM instrument, *Nature*, *454*, 305–309, doi:10.1038/nature07097.

Muto, T. (2001), Shoreline autoretreat substantiated in flume experiments, *Journal of Sedimentary Research*, *71*, 246–254.

Muto, T., and R. J. Steel (1992), Retreat of the front in a prograding delta, *Geology*, *20*, 967–970.

Nichols, G. (1999), *Sedimentology and Stratigraphy*, Blackwell Science, Oxford.

Ollier, C. (1967), Maars: their characteristics, varieties and definition, *Bulletin of Volcanology*, *31*(1), 45–73.

Pelkey, S. M., B. M. Jakosky, and P. R. Christensen (2004), Surficial properties in Gale Crater, Mars, from Mars Odyssey THEMIS data, *Icarus*, *167*, 244–270, doi:10.1016/j.icarus.2003.09.013.

Pelletier, J. D. (1999), Statistical self-similarity of magmatism and volcanism, *J. Geophys. Res.*, *104*, 15,425–15,438, doi:10.1029/1999JB900109.

Perron, J. T., and P. Huybers (2009), Is there an orbital signal in the polar layered deposits on mars?, *Geology*, *37*(155), 155–158, doi:10.1130/G25143A.1.

Postma, G. (1990), Depositional architecture and facies of river and fan deltas: a synthesis, in *Coarse-Grained Deltas*, edited by A. Colella and D. B. Prior, pp. 13–28, Blackwell Scientific, Oxford.

Poulet, F., J.-P. Bibring, J. F. Mustard, A. Gendrin, N. Mangold, Y. Langevin, R. E. Arvidson, B. Gondet, and C. Gomez (2005), Phyllosilicates on Mars and implications for early martian climate, *Nature*, *438*, 623–627, doi:10.1038/nature04274.

Prior, D. B., and B. D. Bornhold (1990), The underwater development of Holocene fan deltas, in *Coarse-Grained Deltas*, edited by A. Colella and D. B. Prior, pp. 75–90, Blackwell Scientific, Oxford.

Prothero, D. R., and F. Schwab (2004), *Sedimentary Geology*, Freeman, New York.

Reading, H. G. (Ed.) (1996), *Sedimentary Environments: Processes, Facies, and Stratigraphy*, Blackwell Science, Oxford.

Robinson, M. S., P. J. Mouginis-Mark, J. R. Zimbelman, S. S. C. Wu, K. K. Ablin, and A. E. Howington-Kraus (1993), Chronology, eruption duration, and atmospheric contribution of the Martian volcano Apollinaris Patera, *Icarus*, *104*(2), 301–323.

Rubin, D. M. (1987), *Cross-bedding, bedforms, and paleocurrents*, *Concepts in Sedimentology and Paleontology*, vol. 1, SEPM, Tulsa, Oklahoma.

Rubin, D. M., and C. L. Carter (2006), Bedforms and cross-bedding in animation, SEPM Atlas Series No. 2 (DVD), http://walrus.wr.usgs.gov/seds/bedforms/animation.html.

Rubin, D. M., and R. E. Hunter (1982), Bedform climbing in theory and nature, *Sedimentology*, *29*, 121–138.

Ruff, S. W., and P. R. Christensen (2002), Bright and dark regions on Mars: Particle size and mineralogical characteristics based on Thermal Emission Spectrometer data, *J. Geophys. Res.*, *107*(E12), 5127, doi:10.1029/2001JE001580.

Ruff, S. W., P. R. Christensen, R. N. Clark, H. H. Kieffer, M. C. Malin, J. L. Bandfield, B. M. Jakosky, M. D. Lane, M. T. Mellon, and M. A. Presley (2001), Mars' "White Rock" feature lacks evidence of an aqueous origin- Results from Mars Global Surveyor, *J. Geophys. Res.*, *106*(E10), 23,921–23,927, doi:10.1029/2000JE001329.

Schmidt, M. E., S. W. Ruff, T. J. McCoy, W. H. Farrand, J. R. Johnson, R. Gellert, D. W. Ming, R. V. Morris, N. Cabrol, K. W. Lewis, and C. Schröder (2008), Hydrothermal origin of halogens at Home Plate, Gusev crater, *J. Geophys. Res.*, *113*, E06S12, doi:10.1029/2007JE003027.

Schultz, P. (2007), Hidden Mars, *Science*, *318*(5853), 1080–1081, doi:10.1126/science.1151412.

Schwarzacher, W. (2000), Repetitions and cycles in stratigraphy, *Earth Science Reviews*, *50*, 51–75.

Scott, D. H., and K. L. Tanaka (1986), Geologic map of the western equatorial region of Mars, Scale 1:15,000,000, *U.S. Geol. Survey Map I-1802-A*.

Sharp, R. P. (1973), Mars: Fretted and chaotic terrains, *J. Geophys. Res.*, *78*, 4073–4083.

Simkin, T. (1993), Terrestrial volcanism in space and time, *Annual Review of Earth and Planetary Sciences*, *21*, 427–452, doi:10.1146/annurev.ea.21.050193.002235.

Smith, D. E., M. T. Zuber, H. V. Frey, J. B. Garvin, J. W. Head, D. O. Muhleman, G. H. Pettengill, R. J. Phillips, S. C. Solomon, H. J. Zwally, W. B. Banerdt, T. C. Duxbury, M. P. Golombek, F. G. Lemoine, G. A. Neumann, D. D. Rowlands, O. Aharonson, P. G. Ford, A. B. Ivanov, C. L. Johnson, P. J. McGovern, J. B. Abshire, R. S. Afzal, and X. Sun (2001), Mars Orbiter Laser Altimeter: Experiment summary after the first year of global mapping of Mars, *J. Geophys. Res.*, *106*(E10), 23,689–23,722.

Smith, G. A., and K. Katzman (1991), Discrimination of aeolian and pyroclastic-surge processes in the generation of cross-bedded tuffs, Jemez Mountains, New Mexico, *Geology*, *19*, 465–468.

Squyres, S. W., and J. F. Kasting (1994), Early Mars: How warm and how wet?, *Science*, *265*, 744–749.

Squyres, S. W., R. E. Arvidson, E. T. Baumgartner, J. F. Bell, P. R. Christensen, S. Gorevan, K. E. Herkenhoff, G. Klingelhöfer, M. B. Madsen, R. V. Morris, R. Rieder, and R. A. Romero (2003), Athena Mars rover science investigation, *J. Geophys. Res*, *108*(E12), 8062, doi: 10.1029/2003JE002121.

Squyres, S. W., R. E. Arvidson, J. F. Bell, J. Brückner, N. A. Cabrol, W. Calvin, M. H. Carr, P. R. Christensen, B. C. Clark, L. Crumpler, D. J. Des Marais, C. d'Uston, T. Economou, J. Farmer, W. Farrand, W. Folkner, M. Golombek, S. Gorevan, J. A. Grant, R. Greeley, J. Grotzinger, L. Haskin, K. E. Herkenhoff, S. Hviid, J. Johnson, G. Klingelhöfer, A. Knoll, G. Landis, M. Lemmon, R. Li, M. B. Madsen, M. C. Malin, S. M. McLennan, H. Y. McSween, D. W. Ming, J. Moersch, R. V. Morris, T. Parker, J. W. Rice, L. Richter, R. Rieder, M. Sims, M. Smith, P. Smith, L. A. Soderblom, R. Sullivan, H. Wänke, T. Wdowiak, M. Wolff, and A. Yen (2004a), The Spirit rover's Athena science investigation at Gusev crater, Mars, *Science*, *305*, 794–800, doi:10.1126/science.1100194.

Squyres, S. W., J. P. Grotzinger, R. E. Arvidson, J. F. Bell, W. Calvin, P. R. Christensen, B. C. Clark, J. A. Crisp, W. H. Farrand, K. E. Herkenhoff, J. R. Johnson, G. Klingelhöfer, A. H. Knoll, S. M. McLennan, H. Y. McSween, R. V. Morris, J. W. Rice, R. Rieder, and L. A. Soderblom

(2004b), In situ evidence for an ancient aqueous environment at Meridiani Planum, Mars, *Science*, *306*, 1709–1714.

Squyres, S. W., R. E. Arvidson, D. L. Blaney, B. C. Clark, L. Crumpler, W. H. Farrand, S. Gorevan, K. E. Herkenhoff, J. Hurowitz, A. Kusack, H. Y. McSween, D. W. Ming, R. V. Morris, S. W. Ruff, A. Wang, and A. Yen (2006), Rocks of the Columbia Hills, *J. Geophys. Res.*, *111*, E02S11, doi:10.1029/2005JE002562.

Squyres, S. W., O. Aharonson, B. C. Clark, B. A. Cohen, L. Crumpler, P. A. de Souza, W. H. Farrand, R. Gellert, J. Grant, J. P. Grotzinger, A. F. C. Haldemann, J. R. Johnson, G. Klingelhöfer, K. W. Lewis, R. Li, T. McCoy, A. S. McEwen, H. Y. McSween, D. W. Ming, J. M. Moore, R. V. Morris, T. J. Parker, J. W. Rice Jr., S. Ruff, M. Schmidt, C. Schröder, L. A. Soderblom, and A. Yen (2007), Pyroclastic activity at Home Plate in Gusev crater, Mars, *Science*, *316*, 738–742, doi:10.1126/science.1139045.

Squyres, S. W., R. E. Arvidson, S. Ruff, R. Gellert, R. V. Morris, D. W. Ming, L. Crumpler, J. D. Farmer, D. J. Marais, A. Yen, S. M. McLennan, W. Calvin, J. F. Bell III, B. C. Clark, A. Wang, T. J. McCoy, M. E. Schmidt, and P. A. de Souza Jr. (2008), Detection of silica-rich deposits on Mars, *Science*, *320*(5879), 1063–1067, doi:10.1126/science.1155429.

Sullivan, R., J. F. Bell, III, W. Farrand, J. Grotzinger, K. Herkenhoff, J. Johnson, L. Richter, C. Weitz, and P. Whelley (2006), Mars Exploration Rover Spirit investigation of the "El Dorado" sand deposit, *Lunar Planet. Sci. Conf.*, *XXXVII*, abstract #1829.

Summerfield, M. (1991), *Global Geomorphology*, Longman Group, London.

Thomson, B. J., N. T. Bridges, R. E. Milliken, J. F. Bell, W. M. Calvin, and C. M. Weitz (2008), New constraints on the origin and evolution of the layered deposits in Gale crater, Mars, in *Lunar and Planetary Science Conference XXXIX*, abstract #1456.

Thomson, D. J. (1982), Spectrum estimation and harmonic analysis, in *Proc. IEEE*, vol. 70, pp. 1055–1096.

Touma, J., and J. Wisdom (1993), The chaotic obliquity of Mars, *Science*, *259*, 1294–1297.

Tyler, S. W., S. Kranz, M. B. Parlange, J. Albertson, G. G. Katul, G. F. Cochran, B. A. Lyles, and G. Holder (1997), Estimation of groundwater evaporation and salt flux from Owens Lake, California, USA, *J. Hydrology*, *200*, 110–135.

Waitt Jr., R. B. (1980), About forty last-glacial Lake Missoula jökulhlaups through southern Washington, *Geology*, *88*, 653.

Ward, W. R. (1992), Long term orbital and spin dynamics of Mars, in *Mars*, edited by H. H. Kieffer, B. M. Jakosky, C. W. Snyder, and M. S. Matthews, pp. 298–320, University of Arizona Press, Tucson.

Ward, W. R., B. C. Murray, and M. C. Malin (1974), Climatic variations on Mars 2. Evolution of carbon dioxide atmosphere and polar caps, *J. Geophys. Res.*, *79*(24), 3387–3395, doi: 10.1029/JC079i024p03387.

Waters, A. C., and R. V. Fisher (1971), Base surges and their deposits: Capelinhos and Taal volcanoes, *J. Geophys. Res.*, *76*(23), 5596–5613.

Watters, T. R., B. Campbell, L. Carter, C. J. Leuschen, J. J. Plaut, G. Picardi, R. Orosei, A. Safaeinili, S. M. Clifford, W. M. Farrell, A. B. Ivanov, R. J. Phillips, and E. R. Stofan (2007), Radar sounding of the Medusae Fossae Formation Mars: Equatorial ice or dry, low-density deposits?, *Science*, *318*(5853), 1125–1128, doi:10.1126/science.1148112.

Weedon, G. P. (2003), *Time-Series Analysis and Cyclostratigraphy: Examining Stratigraphic Records of Environmental Cycles*, Cambridge University Press, Cambridge.

Wilkinson, B. H., N. W. Diedrich, C. N. Drummond, and E. D. Rothman (1998), Michigan hockey, meteoric precipitation, and rhythmicity of accumulation on peritidal carbonate platforms, *Bull. Geol. Soc. Am.*, *110*(8), 1075–1093.

Wilson, L., and J. W. Head (2004), Evidence for a massive phreatomagmatic eruption in the initial

stages of formation of the Mangala Valles outflow channel, Mars, *Geophys. Res. Lett.*, *31*, L15701, doi:10.1029/2004GL020322.

Wilson, L., and J. W. Head (2007), Explosive volcanic eruptions on Mars: Tephra and accretionary lapilli formation, dispersal, and recognition in the geologic record, *Journal of Volcanology and Geothermal Research*, *163*, 83–97, doi:10.1016/j.jvolgeores.2007.03.007.

Wilson, L., and P. J. Mouginis-Mark (2003), Phreatomagmatic explosive origin of Hrad Vallis, Mars, *J. Geophys. Res.*, *108*(E8), 5082, doi:10.1029/2002JE001927.

Wohletz, K. (1983), Mechanisms of hydrovolcanic pyroclast formation: grain-size, scanning electron microscopy, and experimental studies, *Journal of Volcanology and Geothermal Research*, *17*, 31–63.

Wohletz, K. H. (1998), Pyroclastic surges and compressible two-phase flow, in *From Magma to Tephra: Modelling Physical Processes of Explosive Volcanic Eruptions*, edited by A. Freundt and M. Rosi, pp. 247–299, Elsevier, Amsterdam.

Wray, J. J., B. L. Ehlmann, S. W. Squyres, J. F. Mustard, and R. L. Kirk (2008), Compositional stratigraphy of clay-bearing layered deposits at Mawrth Vallis, Mars, *Geophys. Res. Lett.*, *35*, L12202, doi:10.1029/2008GL034385.

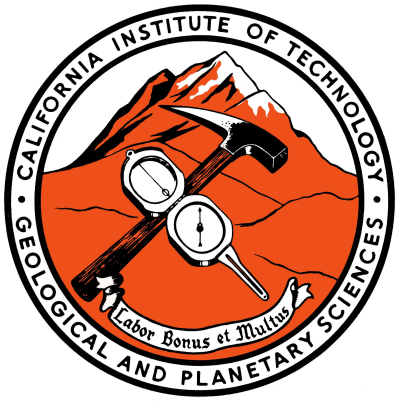
CALIFORNIA INSTITUTE OF TECHNOLOGY
GEOLOGICAL AND PLANETARY SCIENCES
Labor Bonus et Multus